A NOVEL BATTERYLESS PACEMAKER: DESIGN, DEVELOPMENT, AND IN VIVO STUDY IN AN OVINE MODEL

A Dissertation
Submitted to the Graduate Faculty
of the
North Dakota State University
of Agriculture and Applied Science

By

Sajid Mehmood Asif

In Partial Fulfillment of the Requirements
for the Degree of
DOCTOR OF PHILOSOPHY

Major Department:
Electrical and Computer Engineering

October 2016

Fargo, North Dakota

NORTH DAKOTA STATE UNIVERSITY

Graduate School

Title

A NOVEL BATTERYLESS PACEMAKER: DESIGN, DEVELOPMENT, AND IN VIVO STUDY IN AN OVINE MODEL

By

Sajid Mehmood Asif

The supervisory committee certifies that this dissertation complies with North Dakota State University's regulations and meets the accepted standards for the degree of

DOCTOR OF PHILOSOPHY

SUPERVISORY COMMITTEE:

Dr. Benjamin D. Braaten
Chair

Dr. David A. Rogers

Dr. Daniel L. Ewert

Dr. Kyle J. Hackney

Approved:

June 16, 2017
Date

Dr. Alan R. Kallmeyer
Department Chair

ABSTRACT

A standard pacemaker can improve a patient's quality of life and may even prolong it, but conventional pacemakers contain leads and batteries, which have their own complications. Hence, the need for a pacemaker with leadless and batteryless capabilities is becoming increasingly important, as it reduces infection risk, device failure, and patient discomfort. Unlike other leadless pacing technologies, the proposed method in this work does not require a battery or leads. More specifically, a novel leadless pacemaker was proposed that harvest energy from radio frequency (RF), using a metamaterial-based rectenna, to power the pacemaker and stimulate the myocardium. Initially, path loss in the body was computed by performing experiments on ovine models and available RF power, deep inside the body, was estimated. These baseline specifications were then used to design an implantable rectenna, which was simulated and optimized using Advanced Design System (ADS) and ANYS-High Frequency Structure Simulator (HFSS). The performance of the antenna was initially tested in vitro and was then integrated with a separately designed rectifier circuit using a matching circuit. The resulting module, when integrated with a pacing circuit, formed a leadless and batteryless pacemaker and was then implanted at the left ventricle of an ovine model. This prototype demonstrated that leadless pacing, using a RF-based energy harvesting method, can be achieved. Furthermore, to improve the overall form factor and achieve a conformal design, a numerical model for the deeply implantable antennas, in HFSS, was characterized. Finally, this proposed model was validated analytically as well as experimentally, and was also used to design a conformal implantable antenna for the leadless pacing application. This research has strengthened the possibility of leadless pacing using the RF energy harvesting method and has paved the way for future research in this area. Indeed, this proposed technology has the potential to bring transformational possibilities, not only to leadless pacing, but also to other deeply implantable biomedical devices.

ACKNOWLEDGEMENTS

All praise is due to Allah, the Almighty, Who has empowered me with education and gave me the strength to complete this endeavor. As it is mentioned in the Quran, "Whatever He wills occurs without resistance, and whatever He does not will, never occurs."

I would like to thank all the people who contributed in some way to the work described in this dissertation. First and foremost, I am sincerely grateful to my advisor, Dr. Benjamin D. Braaten, for his sincere guidance, continuous support, and understanding during my Ph.D. studies at NDSU. His friendly attitude, respect for his students, and mentorship was paramount in providing me a well-rounded meaning for life, as well for work. His continuous encouragement and praise has enabled me to work without the fear of failure. To me, he is an excellent example of a researcher, mentor, and role model.

I am full of gratitude to my committee members, Dr. David A. Rogers, Dr. Kyle J. Hackney, and Dr. Daniel L. Ewert, for their valuable support, guidance, and helpful recommendations. Their constructive suggestions have shaped my research and their sincere interest in my work and dissertation is very much appreciated. I am grateful to Dr. Ewert for instilling in me the interest in biomedical devices and for being a true source of inspiration, which goes beyond research. His passion and enthusiasm in research was motivational for me, even during difficult times in my Ph.D. pursuit.

I must acknowledge all the funding sources that made my Ph.D. research possible. In addition to funding from my home country, Pakistan, I am honored to have received National Science Foundation funded ND EPSCOR Doctoral Dissertation Assistantship. Furthermore, I am the recipient of the prestigious IEEE Antenna and Propagation Society Doctoral Research Award, NDSU Innovation Challenge Competition, Ozbun Entrepreneurial Fellowship, and College of Engineering–Research Assistant of the Year Award. All of the mentioned awards and fellowships either provided me with a prize money or research funding, which supported my Ph.D. studies.

The work described in this dissertation was accomplished with the help and support of my fellow researchers and collaborators. At NDSU, I worked closely with Jared Hansen, Adnan Iftikhar, Muhammad Khan, Jacob Parrow, and outside NDSU, I worked collaboratively with Dr. Keith Maile

and his team at Boston Scientific, Arden Hills, MN. I was fortunate to work with these talented individuals, who certainly contributed to my success. I am also thankful to Dr. Scott Smith, Ryan Striker, and other fellow officers of IEEE-Eta Kappa Nu, for supporting me to reinstate the Gamma Tau chapter at NDSU after it being dormant for more than two decades. I would be remiss if I did not thank Jeffrey Erickson, Laura Dallman, and Priscilla Schlenker, who deserve credit for providing assistance with administrative tasks and keeping our work smooth. Additionally, Eric Christianson provided immediate support for computer related problems. I am grateful for the opportunity to serve the IEEE Red River Valley Section as the Chairman, and also as the Vice Chairman, and the support I received from its members and officers, especially Dr. Na Gong.

Thank you, to all former and current members of RF and Applied Electromagnetics Lab. at NDSU, with a special mention to the undergraduates who have given me the opportunity to teach and mentor them. These students, especially Jerika, Ellen and Lauren, have given me the opportunities to learn more than what I was trying to teach them.

Moreover, I would like to thank my whole family for supporting me and helping me throughout my life and during this study. My mom and dad, my brothers, Saqib, Zeeshan and Binyameen and my lovely sister, Rabia. Mom and Dad, thank you very much for your unconditional love and tremendous support during my entire life. Without your support, I could never be what I am today. Finally, I am very grateful to my loving wife, Zikra Khawas, for her understanding, and all her sacrifices, sincere support, and love during these years. Thank you for being the mom of my lovely kids, Saad, Masfa, and Hatim, who are the pride and joy of my life.

Thank you.

Sajid M. Asif

DEDICATION

I would like to dedicate this dissertation to my entire family: My parents Faqir Khan and Zermina Jan; my brothers Saqib, Zeeshan, and Binyameen; my sister Rabia.

I also dedicate this dissertation to my dearest friend and my caring wife, Zikra Khawas, and to my beautiful children, Saad, Masfa and Hatim.

TABLE OF CONTENTS

LIST OF TABLES

LIST OF FIGURES

LIST OF APPENDIX FIGURES

Figure Page

1. INTRODUCTION

1.1. Introduction

Electronic implantable medical devices (IMDs) have received much attention in recent years and significant research and investments have been dedicated to developing these devices. These devices do not only improve the quality of life of the patients but have the potential to increase the life span of a patient. Some of the examples of these devices include implantable cardioverter defibrillators (ICDs), cardiac pacemakers, an endoscopic capsule, an implantable electrocardiogram (ECG) recorder, an electrical stimulator and an artificial heart. Most of these IMDs are battery-powered and the battery is either embedded inside the device or connected externally via leads. These batteries have a finite life, so when depleted, they needs to be replacement. Also, the leads cause additional complications due to infection and dislodgement [1].

In order to address the power delivery issues, some researchers have been developing new techniques to increase the battery life, while others have focused on the techniques of wireless power transfer (WPT). The idea of using the WPT for biomedical applications simply means that for an implanted medical device inside a patient, there should be no wires used and the transfer of electrical energy should happen wirelessly. This is a fascinating idea which can bring several advantages to the patient. For example, a pacemaker using the WPT technology will not need battery replacement and hence the patient may not need surgery. Also, with no leads going down the veins, multiple pacing electrodes (pacemakers) can be implanted inside a patient's heart.

While there are many advantages of the WPT technique, this method also has its own challenges, which include achieving a better form factor, power transfer efficiency and miniaturization of the antenna. This dissertation introduces the method of radio frequency (RF) energy harvesting for the design of a wireless implantable pacemaker and addresses these challenges in a systematic manner. Overall, this work has contributed towards the advancement of the knowledge in the area of wireless power transfer for implantable electronic medical devices, specifically pacemakers.

This chapter briefly discusses the need for an artificial pacemaker and presents the limitations of the conventional pacemakers. It further discusses the previous work and also highlights the latest trends in leadless pacing. This is followed by the summary of our original contributions and

the research questions and objectives. Finally, the details of the technical objectives are presented and an outline of the dissertation is summarized.

1.2. The Need for an Artificial Pacemaker

The electrical conduction system of the heart is a group of specialized heart muscle cells in the heart's walls that send electrical signals to the myocardium causing it to contract. In the case of a normal cardiac electrical conduction, an impulse is generated by the sinoatrial (SA) node of the heart, which then propagates to, and stimulates the myocardium (cardiac muscle). Mainly, this system consists of, (a) sinoatrial (SA) node, (b) atrioventricular (AV) node, and (c) His-Purkinje system (fibers located along the walls of the heart's ventricles) [3]. An illustration of the electrical conduction system of the heart with detail information is shown in Fig. 1.1 [2].

The SA node is the natural pacemaker of the heart which helps the heart to beat at a normal rate which is essential for the supply of oxygen to all parts of the body. When the heart's natural pacemaker is not working correctly, an artificial pacemaker may be recommended to regulate the heart beat in a better manner. Bradycardia and heart blockage are some of the most common reasons. Bradycardia is the condition when the heart beats slowly, while heart blockage is caused by slowed or disrupted electrical signal as it propagates through the heart. Aging and muscular

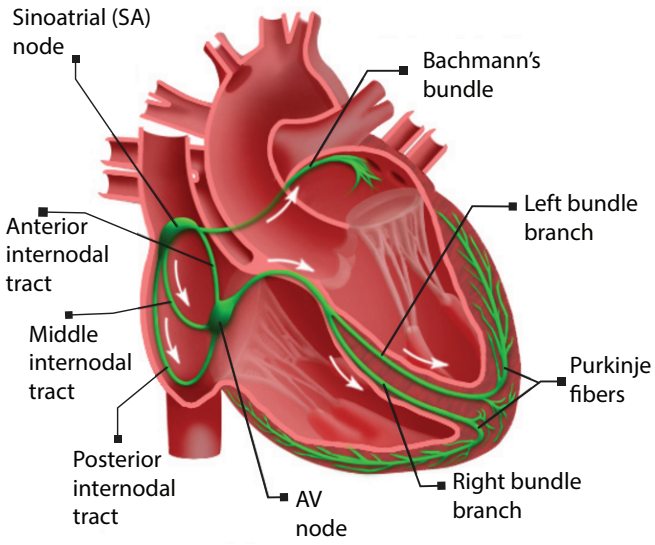

Figure 1.1. An illustration of the electrical conduction system of the human heart with details [2].

dystrophy are also known to be the cause of the heart blockages. The Doctors may also recommend a pacemaker if you have a long QT syndrome, a sinus syndrome or need cardiac resynchronization therapy (CRT). People with heart congenital disease or who have had heart transplant may also need a pacemaker.

1.3. Background

In 1932, Hayman *et al.* [4] developed the first experimental pacemaker, consisting of an electrical source and a mechanical device to control impulse formation and rate. The current was supplied via a needle introduced percutaneously to the right atrium. The first cardiac pacemaker implantation in humans, was however, performed by Senning in Sweden on 8th October, 1958 [5]. Today, more than three million people worldwide have pacemakers. Also, about 600,000 pacemakers are implanted each year and the need for a pacemaker has been increasing as heart failure (HF) alone affects more than 5 million people in the United States and 25 million worldwide [6]. The mortality rate is high, as about 50 percent of patients with advanced heart failure die within five years of diagnosis. It is reported that the total global revenue generated from cardiac pacemakers could reach USD 12.8 billion by year 2023, while the total number of pacemakers' consumption could cross 2.4 million [7].

Broadly speaking, the potential application of this research is related to anyone, who has the symptoms of HF and who has been treated maximally with medications, and has not responded to the conventional CRT. The long-term goal is to clinically translate the leadless pacing technology to treat non-responders to CRT to improve patient outcomes and restore quality of life.

The following section define the artificial pacing system for the heart and briefly discusses the problems associated with existing pacing systems. Discussing these problems will lay the foundation for the proposed research. Also, previous and current work on cardiac pacemakers will be summarized and discussed.

1.4. The Conventional Pacemaker Technology and its Complications

A typical pacing system is made up of a pacemaker, leads, and a programmer. The pacemaker sends electrical impulses to pace the heart when its own rhythm is too slow or irregular. The pacing lead is an insulated wire that carries the impulses from the pacemaker and delivers them to the heart to assist its beating. A picture of a human's heart model showing a complete

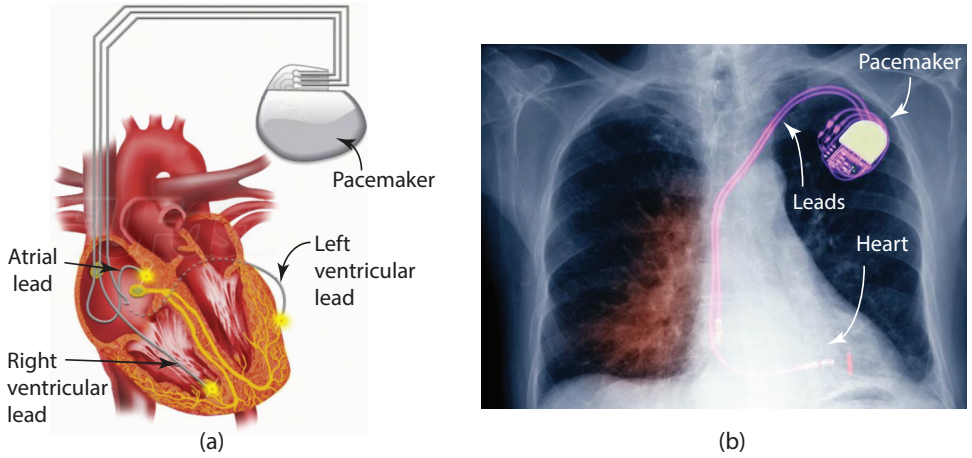

Figure 1.2. (a) A human's heart model showing complete pacing system, i.e., the pacemaker, leads and electrodes in atrial, right and left ventricles. (b) A chest X-ray after the implantation of a dual-chamber cardiac pacemaker [8].

pacing system, as well as a picture of a chest X-ray showing an implanted pacemaker is shown in Fig.1.2(a) and (b) [8].

Conventional cardiac pacemakers improve the quality of life and reduce mortality, but there are problems associated with them due to many potential procedure- and device-related complications. Approximately, every 10^{th} patient experiences a short-term complication related to transvenous implantation of the pacemaker, which may be attributed to either the pulse generator (hematoma, skin breakdown, pocket infection) or venous access and lead implantation (pneumothorax, cardiac tamponade, lead dislodgement), as reported in [9]. In the long term however, the leads are often considered to be the weakest link of the cardiac pacing system, which can intensify the venous obstruction and are prone to insulation breaks, conductor fracture, and even infection [1, 10–12]. There may be other conditions that may accompany these complications of the cardiac pacing systems, often leading to other unfavorable medical treatments, incurring significant cost [13]. It has been evident that the Achilles heel of the cardiac pacemakers is the transvenous lead, which is also its critical component and serves as a conduit for the delivery of energy pulses to provide the stimulation [14]. A list of issues related to a conventional pacemaker, its components and implantation procedure is shown in the Table 1.1.

Table 1.1. A list of various issues related to a conventional pacemaker [13]

Component	**Issues**
Implantable procedure	
Surgical pocket	Surgical morbidities, Vascular access complications
Transvenous leads	Lead dislodgement, difficulty in achieving acceptable pacing & sensing at desired sites (especially for CRT)
Technological system	
Device casing / leads antennas / battery	Interface, failure of each component especially the leads
	Finite battery longevity requiring device replacement
Patient concerns	
	Device failure and longevity
	Cosmetics, life style limitations and environment interface
Long term clinical problems	
	Pocket and lead infection
	Lead interaction with cardiac structures (tricuspid valve, venous thrombosis) and fracture
	Best pacing site(s) to preserve or enhance heart function

In addition to the lead complications, CRT is currently delivered epicardially through the coronary sinus, whose anatomy can make implantation difficult to achieve the optimal pacing site. Endocardial pacing in the left ventricle can obviate this limitation and may provide an alternative approach in the patients who failed to respond to coronary sinus pacing [15]. It is therefore argued that leadless pacing is the way forward in the field in order to avoid the lead complications and may provide greater flexibility to stimulate the myocardium at either single or multiple sites. It is this idea of leadless pacing that lead to the work in this dissertation.

1.4.1. Previous work on leadless pacing

As mentioned in the previous section, the concept of a totally self-contained leadless intracardiac pacemaker was first proposed in 1970 and successfully implanted in animals using a self-contained device powered by both mercury-zinc and nuclear power sources [16]. Several researchers and manufacturers have further developed it using either a totally self-contained intracardiac pacemaker, or pacing from an external energy source. The improved battery energy, endocardial fixation and novel delivery systems have been crucial in improving the concept of leadless pacing [17]. The feasibility of ultrasound-mediated energy to power a leadless electrode for direct myocardial stimulation is the first to be reported. Feasibility of this technology was first demonstrated acutely

on porcine models and later on humans [18], but the energy transmission efficacy was debated, which was only 0.07 % [19]. Also, the first two implants of wireless left ventricle (LV) pacing used to upgrade a transvenous device for resynchronization were announced in May 2011. This system however has a limited clinical application as it requires the transmitter to be over the apex, in order to transmit the energy to the implanted module. A similar system using electrical induction has also been demonstrated in animal models [20]. Despite that, this system has the potential for more efficient energy transfer, it requires a similar transmitter at apex. Also, another major concern with this technology is the potential external interference by environmental magnetic fields and the long-term safety with heat production in the receiver unit.

1.4.2. Latest trends in leadless pacing

The first ever implantation of leadless endocardial pacing using ultrasound was performed on humans using the WiCS-LV (Wireless Stimulation Endocardially for CRT Trial) system developed by EBR (EBR systems, CA, USA) [21]. This system requires a conventional pacing lead and a pulse generator to activate a single, battery-less pacing electrode in the left ventricle (LV), as shown in Fig. 1.3 [21].

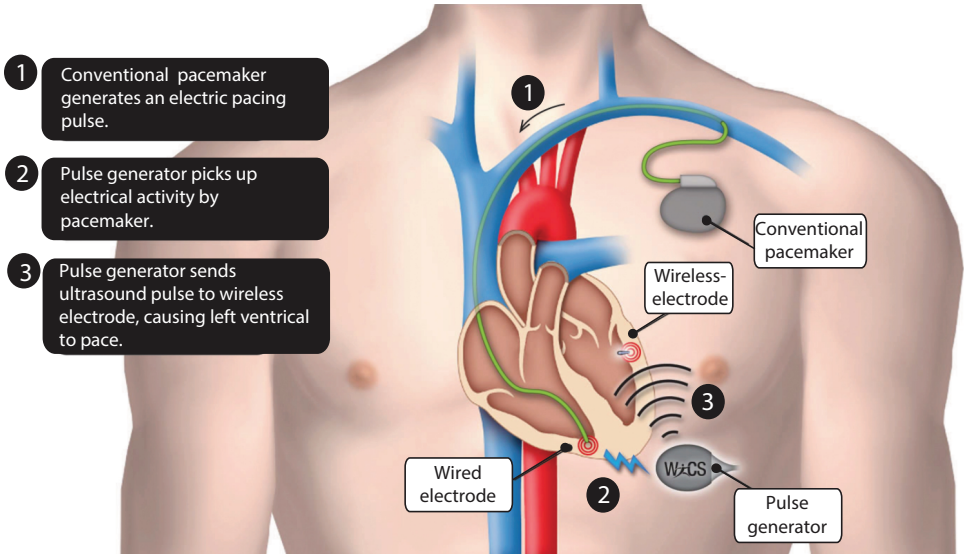

Figure 1.3. An ultrasound device (WiCS-LV) for cardiac pacing. This device requires a conventional pacing lead and pulse generator to activate a single battery-less pacing electrode [21].

WiCS-LV is co-implanted with a pacemaker or CRT device and provides bi-ventricular pacing by sensing the right ventricle RV pacing output of the co-implant. It then generates the ultrasound wave which is converted to an electrical output at the receiver wireless-electrode to pace the LV. This LV resynchronization therapy in HF patients shows that leadless pacing may be safely applied and effective, but the findings are limited and yet has to be validated by other ongoing studies.

The latest generation of leadless pacemakers have been developed by Medtronic [22], St. Jude Medical Inc. [23], and Boston Scientific Corporation (BSC) [24]. Medtronic's Micra Transcather Pacing System (TPS) has recently been approved by the United States Food and Drug Administration (FDA), while Nanostim (St. Jude's leadless pacemaker) is claimed to be the world's first commercially available leadless pacemaker and yet to get an approval by the FDA. Details on the BSC's version of the leadless pacemaker - called EMPOWER, are not fully available but it has been reported that the pre-clinical studies on this device have been completed [24]. Pictures of these single chamber and battery powered pacing devices are shown in Fig. 1.4 [22, 23].

1.5. Original Contributions

The pressing need for all the medical device companies manufacturing the pacemakers in the current era is to make the pacemaker fully wireless, so that there are no wires and no associated

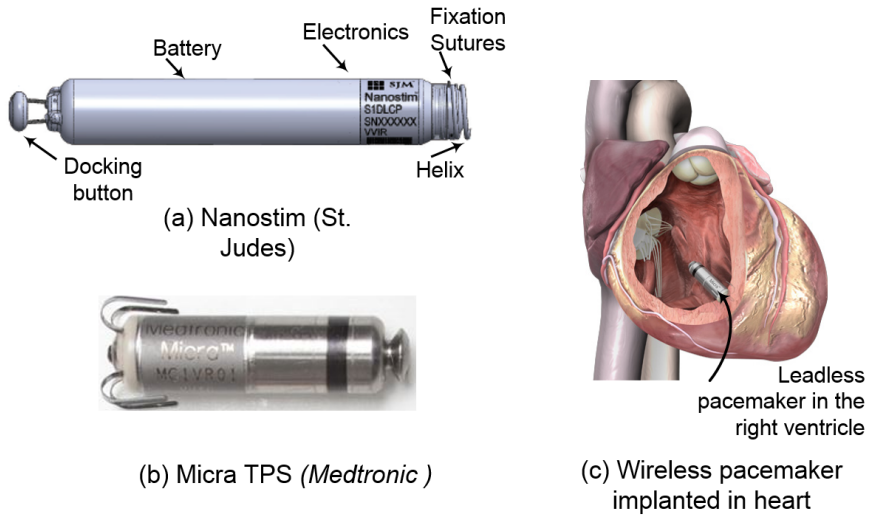

Figure 1.4. Pictures of latest single-chamber leadless pacemakers. (a) St. Jude Medical's Nanostim Leadless pacemaker system. (b) Medtronic's Micra TPS (Transcatheter Pacing System). (c) A model of Micra TPS implanted in the RV of a heart [22, 23].

complications. The above mentioned newest pacemakers however contain batteries, which have a finite life and could need replacement in the life of the patient. However, there is still a need for a batteryless device, which would potentially make multiple site pacing practical and address the unmet clinical needs of the CRT non-responders.

The objective of this research is to develop a novel method of cardiac pacing, which does not require leads or electrode batteries and has the ability to pace multiple sites of the heart, not just a single chamber. This novel method is achieved by exploring the integration of implantable antennas with RF energy harvesting techniques to power the pacemaker for myocardial stimulation. The proposed solution, as shown in Fig. 1.5 [25], has a significant advantage over all the aforementioned methods because batteries are not required for the operation of the implanted electrodes, which saves almost half of the available space. Also, the proposed technology has a significant advantage over the ultrasound system because it is completely wireless and allows multiple electrodes to be implanted without a pulse generator or pacemaker lead. This technology allows the flexibility of pacing multiple sites of the heart without the need of any leads.

This research addresses the need of leadless cardiac pacing using the technique of radio frequency for wireless power transfer. In particular, this research addresses the miniaturization

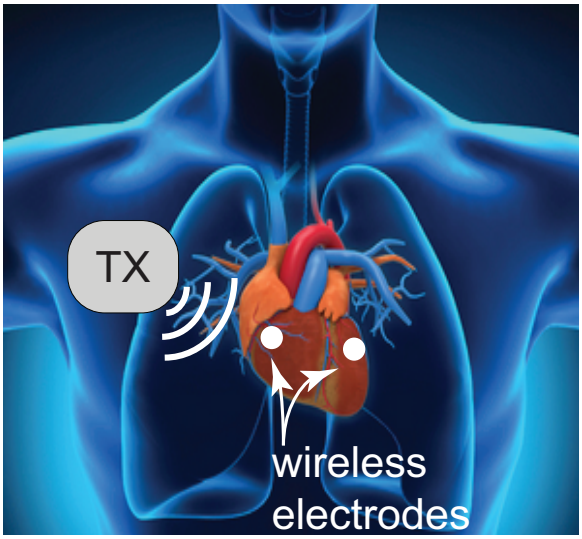

Figure 1.5. A conceptual illustration ff the proposed leadless cardiac pacing system (TX is the transmitter transmitting RF energy into the body). [25].

of the implantable antenna, and also the use of an efficient rectifier circuit to convert the power received by the implantable antenna to a DC voltage for the stimulation of the heart muscle. An asynchronous, non-demand pacing at different beats per minute is achieved using a microprocessor, powered by the harvested RF energy. To demonstrate the effectiveness and workings of this proposed technique, a manufactured prototype of a wireless and batteryless pacemaker is successfully tested in vivo in an ovine model and wireless pacing is achieved.

1.6. Research Questions and Objectives

The aim of this work is to address the following research questions.

1. Can we design and develop a numerical as well as a valid in vitro model to mimic the physiological environment for the design, development, optimization, and measurement of the implantable antennas and eventually the pacemakers?

2. Can we design and manufacture a proof-of-concept leadless pacemaker and test this prototype to demonstrate batteryless and fully wireless pacing?

3. Can the implanted pacemaker be made small enough and still capture enough "safe recommended" RF energy to allow cardiac pacing?

1.6.1. Technical objectives

The specific technical objectives of this research are summarized below.

1. To measure the path loss in the body by performing experiments on ovine models and also, to predict and estimate the receive power at the proposed implant location inside the body.

2. To investigate various types of implantable antennas and methods to achieve miniaturization. Next, use a full wave 3D electromagnetic simulation software, ANSYS-High Frequency Structure Simulator (HFSS) to design, develop, and optimize a miniaturized implantable antenna for pacemaker application. Furthermore, fabricate the implantable antenna and measure its performance to check its suitability for the proposed application.

3. To design, develop, manufacture and test an efficient rectifier circuit for power harvesting in implantable applications. Also, to integrate the rectifier circuit with the implantable antenna using a matching circuitry.

4. To fabricate the prototype of a wireless pacemaker (electrode) by the integration of the implantable antenna with the rectifier circuit, matching circuit and a microprocessor based circuit. Moreover, to test this prototype electrode in an ovine model to demonstrate pacing.

5. To design, develop and validate a wide-band numerical model in ANSYS-HFSS for the design and optimization of deeply implantable antennas for pacing applications.

1.7. Dissertation Outline

This dissertation is organized as follows. Chapter 2 presents the background and literature review on deeply implantable antennas and also summarizes various methods used for the wireless power transfer for biomedical applications. In Chapter 3, a path loss model has been developed using in vivo experiments. The uncertainty analysis of the equipment and power computation inside the body are also discussed in the same chapter. Chapter 4 describes the design, development and fabrication of the implantable antenna, rectifier and circuitry, as well as, the overall form factor of the proposed leadless pacemaker. It further explains the in-vivo measurements and presents results on a wireless pacemaker. In Chapter 5, a wide-band numerical model is designed, developed and validated for designing deeply implantable antenna applications. Finally, a general conclusion and a summary of contributions, as well as the limitations of the work and future research recommendations are presented in Chapter 6.

A theoretical derivation of specific absorption rate and its relationship with power density is discussed in Appendix A.

1.8. References

[1] R. G. Hauser *et al.*, "Clinical experience with pacemaker pulse generators and transvenous leads: An 8-year prospective multicenter study," *Heart Rhythm*, vol. 4, no. 2, pp. 154–160, 2007.

[2] Childrens Heart Institute, USA. (2017, May. 10). [Online]. Available: http://www.choc.org.

[3] U.S. National Library of Medicine. (2017, May. 10). [Online]. Available: https://www.medlineplus.gov

[4] S. Furman *et al.*, "Reconstruction of hyman's second pacemaker," *Pacing Clinical Electrophys.*, vol. 28, no. 5, pp. 446–453, 2005.

[5] A. Senning, "Cardiac pacing in retrospect," *The Amer. J. of Surgery*, vol. 145, no. 6, pp. 733–739, 1983.

[6] A. J. Greenspon *et al.*, "Trends in permanent pacemaker implantation in the united states from 1993 to 2009: Increasing complexity of patients and procedures," *J. Amer. Coll. Cardiol.*, vol. 60, no. 16, pp. 1540–1545, 1983.

[7] Transparency Market Research, USA. (2017, March 1). [Online]. Available: http://www.transparencymarketresearch.com

[8] John Hopkins Medicine, USA. (2017, March 1). [Online]. Available: http://hopkinsmedicine.org

[9] O. U. Erik *et al.*, "Incidence and predictors of short- and long-term complications in pacemaker therapy: The FOLLOWPACE study," *Heart Rhythm*, vol. 9, no. 5, pp. 728–735, 2012.

[10] M. Haghjoo *et al.*, "Predictors of venous obstruction following pacemaker or implantable cardioverter-defibrillator implantation: a contrast venographic study on 100 patients admitted for generator change, lead revision, or device upgrade," *Europace*, vol. 9, pp. 328–332, 2007.

[11] G. H. Robert *et al.*, "Risk factors for infection of implantable cardiac devices: data from a registry of 2496 patients," *Europace*, vol. 15, no. 1, pp. 66–70, 2012.

[12] S. Pakarinen *et al.*, "Short-term implantation-related complications of cardiac rhythm management device therapy: a retrospective single-centre 1-year survey," *Europace*, vol. 12, no. 1, pp. 103–108, 2009.

[13] E. E. Gul and M. Kayrak, *Common Pacemaker Problems: Lead and Pocker Complications, Modern Pacemakers - Present and Future.* InTech, 2011.

[14] R. E. Kirkfeldt *et al.*, "Risk factors for lead complications in cardiac pacing: A population-based cohort study of 28,860 danish patients," *Heart Rhythm*, vol. 8, no. 10, pp. 1622–1628, 2011.

[15] N. Derval *et al.*, "Optimizing hemodynamics in heart failure patients by systematic screening of left ventricular pacing sites: The lateral left ventricular wall and the coronary sinus are rarely the best sites," *J. of the Amer. Coll. of Cardiol.*, vol. 55, no. 6, pp. 566–575, 2010.

[16] J. W. Spickler *et al.*, "Totally self-contained intracardiac pacemaker," *J. of Electrocardiology*, vol. 3, no. 3-4, pp. 325–331, 1970.

[17] K. L. Lee, "In the wireless era: leadless pacing," *Expert Review of Cardiovascular Therapy*, vol. 8, no. 2, pp. 171–174, 2010.

[18] D. S. Echt *et al.*, "Feasibility and safety of a novel technology for pacing without leads," *Heart Rhythm*, vol. 3, no. 10, pp. 1202 – 1206, 2006.

[19] K. L. Lee *et al.*, "First human demonstration of cardiac stimulation with transcutaneous ultrasound energy delivery: Implications for wireless pacing with implantable devices," *J. Amer. Coll. Cardiol.*, vol. 50, no. 9, pp. 877 – 883, 2007.

[20] W. Heinrich *et al.*, "Leadless pacing using induction technology: impact of pulse shape and geometric factors on pacing efficiency," *Europace*, vol. 15, no. 3, pp. 453–459, 2013.

[21] A. Auricchio *et al.*, "First-in-man implantation of leadless ultrasound-based cardiac stimulation pacing system: novel endocardial left ventricular resynchronization therapy in heart failure patients," *Europace*, vol. 15, no. 8, pp. 1191–1197, 2013.

[22] Medtronic Inc., MN, USA. (2017, June 5). [Online]. Available: http://medtronic.com/en-us/micra

[23] St. Jude Medical Inc., MN, USA. (2017, June 5). [Online]. Available: http://sjm.com/leadlesspacing.

[24] Boston Scientific Corp., MN, USA. (2017, June 5). [Online]. Available: http://www.bostonscientific.com

[25] Live Science. (2017, June 5). [Online]. Available: http://www.livescience.com

2. RELATED WORK

2.1. Introduction

In this era, the demand for improved functionalities and performances of the implantable biomedical devices has surged, which is directly affecting the power requirements of these devices. To meet the power requirements, the primary option has been batteries or percutaneous leads, but they have reliability issues and risk of infection, respectively. Alternatively, researchers have been investigating the applications of energy harvesting techniques inside the body and wireless power transfer using various methods. There is a promise in this technology as it has shown the potential to deliver safe power to implantable devices and increase longevity.

This chapter presents various methods of energy harvesting technologies and their applications in implantable devices. A summary of the state-of-the-art technologies in wireless power transfer is also provided. Furthermore, the application of radio frequency (RF) energy harvesting for implantable applications is discussed and related work on the implantable antennas is reported. Finally, conclusion of the chapter is provided at the end.

2.2. Related Work on Energy Harvesting for Implantable Applications

Several methods of energy harvesting, wireless power transfer and wireless charging for implantable applications or IMDs have been reported in literature [1–4]. Some of the most relevant methods are summarized below.

2.2.1. Kinetic harvesters

These types of harvesters use human and machine (or device) motion and collect energy that can be used as an alternative to batteries in various applications [5]. Depending on the transduction method the energy harvesters in this category could be either electromagnetic, electrostatic, or piezoelectric. In 1986, Seiko introduced first prototype of a wristwatch, called 'AGM' (automatic power generating system) which used electromagnetic transducers, converting kinetic movement into electrical energy [6]. Feasibility of the same technique, developed for quartz watches, was then successfully tested as a power source for implantable cardiac pacemakers [7]. In [8], it was shown that an electrostatic transducer could generate upto 58 μW by the exploitation of a variable

capacitor. This study was aimed to supply electrical energy for in vivo applications such as a cardiac pacemaker.

2.2.2. Infrared radiation

In these energy harvesters, the power is transmitted by the infrared (IR) source from outside the body to an array of implanted photodiodes, which received the radiation and then convert them into current to charge the battery of an implanted device. A schematic of this setup is illustrated in Fig. 2.1 [9]. An IR radiation harvester based implantable system was tested on a live rat and the results are presented in [9]. It was shown that for 17 minutes of IR radiation supply at $22\,mW/cm^2$ of incident power density, the system can successfully harvest enough energy that can drive a current of $20\,\mu A$ required for a pacemaker for 24 hours. Murakawa *et al.* presented a study and demonstrated the infrared energy transmission through a chicken tissue and also showed the conversion efficiency [10].

Overall, an efficient power transfer using this method requires a large photodiode array to be placed very closed to the transmitter. These limitations make this method unsuitable for deeply implantable applications.

2.2.3. Low frequency magnetic fields

In these kind of harvesters, the low frequency magnetic fields (outside the body) are used to rotate an implanted rotor to generate power by exploiting its mechanical rotation. This method was initially proposed in [11] and later used in [12], in which it was reported that a power of up

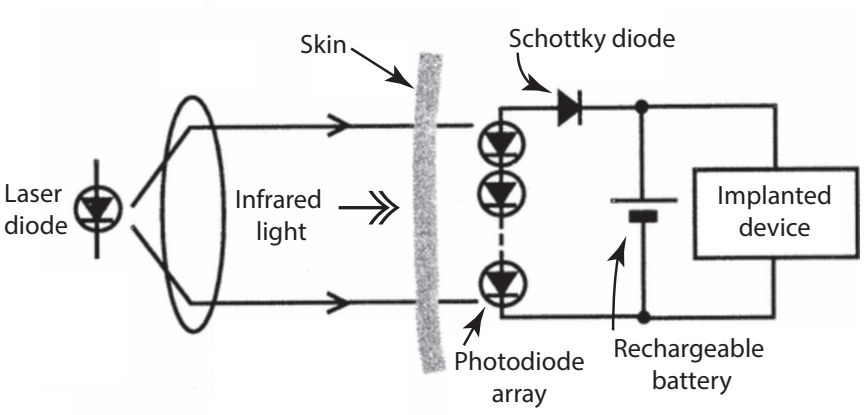

Figure 2.1. A schematic diagram of an infrared (IR) radiation harvester [9].

to 3.1 W, over a distance of 1.5 cm, could be generated. A layout of this system is shown in Fig. 2.2 [12]. This technology does allow the scavenging of high power, but the implanted rotor's large dimension, and the need for periodic substitution and lubrication of the moving parts make it impractical for implantable applications.

2.2.4. Inductive links

This method has been the most widely used for applications in implantable devices. As shown in the Fig. 2.3, this technique uses two coils, one working as a transmitter while the other as a receiver. A source of alternating current creates a variable magnetic field in the primary coil (external), which then gets coupled to the secondary coil in the implanted device, creating a voltage across it. This works on the phenomenon of Faraday-Neumann-Lenz's law. In addition to the wireless power transmission, this technique also allows bidirectional communication using the same inductive link, making it one of the most suitable methods for implantable medical applications.

An inductive coupling link uses magnetic coupling as the communication environment, which is similar to radio frequency identification techniques [13], [14]. Most of the research found in literature on inductive links is in the range of a few MHz and lower [15–17]. A frequency of 20 MHz or lower has also been used to avoid power absorption which causes heating of the tissue [18].

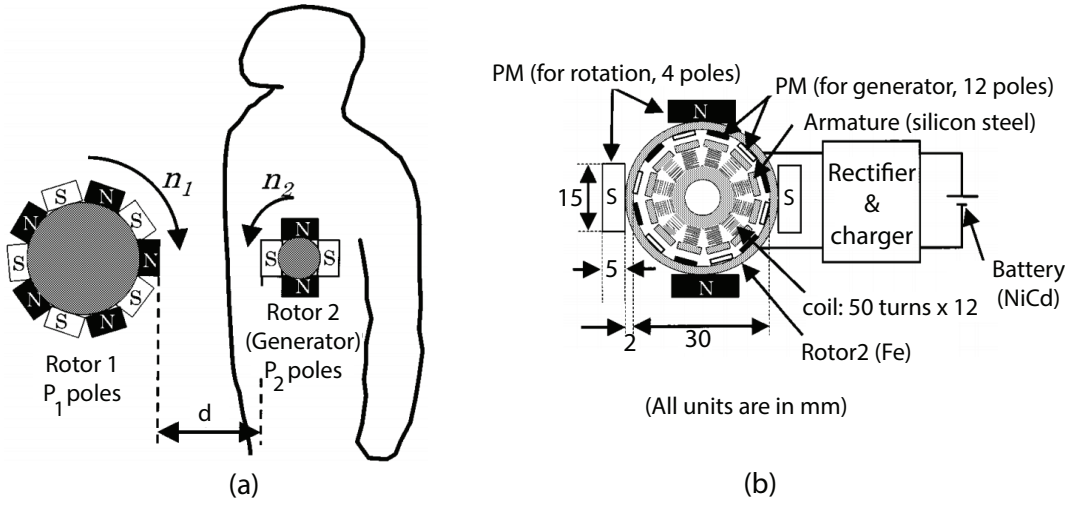

Figure 2.2. An externally applied low frequency magnetic field moves an implanted rotor, which generates electric voltage. (a) Overview of the system, and (b) details of the implanted rotor and circuits [12].

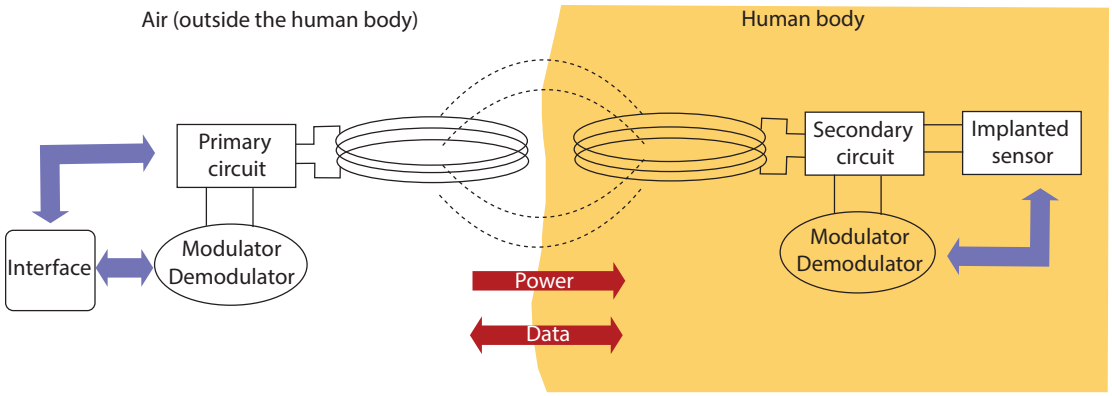

Figure 2.3. A simple overview of an inductive link with power and bidirectional data transmission [13].

In these systems, the radio frequency (RF) power signal radiates from the reader coil antenna, which transmits low power but fixed sinusoid carrier amplitude. This hence provides a stable RF signal, which is essential for good wireless transfer power. In [19], a prototype system using a spiral coil was studied to demonstrate the feasibility of the energy transfer for artificial implants such as pacemakers. Today, wireless implantable devices that can be powered or recharged with inductive links are now commercially available. Medtronic's RestoreUltra Neurostimulator is one the many products that is now FDA approved and commercially available [20]. This is a rechargeable device which stimulates the spinal cord and can be recharged without any invasive procedure.

Following are some of the drawbacks of inductive links. In order to achieve good efficiency of an inductive link, the source (primary coil) and the implanted device (having a secondary coil) have to be sized and shaped matched to one another and should be located within a few millimeters, and very carefully aligned. For proper operation, a large magnetic coupling factor between the source and implanted device coils is required. Failing to achieve these considerations can result in, (a) low efficiency energy transfer, (b) excessive heating, and (c) very reduced energy transfer [21].

2.2.5. State-of-the-art technologies in wireless power transfer for implantable applications

Contrary to the conventional two-coils inductive link method, the four-coils resonance-based technique, as shown in Fig. 2.4, was first introduced by researchers at MIT (Massachusetts Institute of Technology) featuring high efficiency at midrange [22–25]. This new system was first attempted

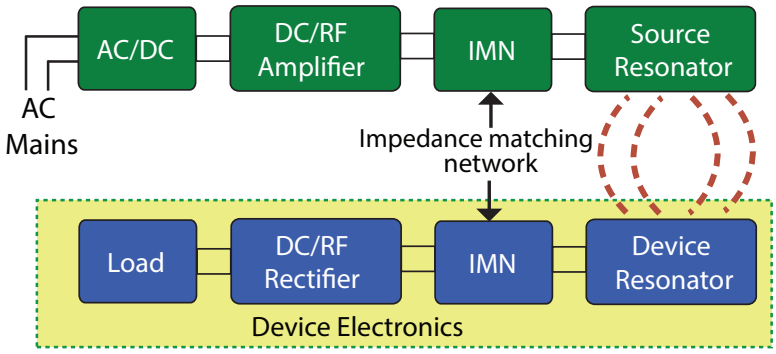

Figure 2.4. Configuration of a typical 4 coils resonance−based wireless transfer system [28].

for biomedical implants [26] but a three-coil based link was later introduced with high efficiency and power delivery [27].

WiTricity and Thoratec have been using this method, using resonant energy transfer, to develop a fully implantable and wirelessly charged left ventricular assist device (LVAD) [28]. This method is able to charge a deeply embedded implanted device by a power source several centimeters above the skin and is thereof flexible, more comfortable for the patients and poses lower risks. Furthermore, ReliantHeart Inc. and Dualis MedTech have teamed up to implement a fully wireless, Transcutaneous Energy Transfer System exclusively for the LVAD (model: HeartAssist5) [29], which uses Dualis MedBase technology. This technology achieves the wireless transmission of energy as well as data using resonant inductive coupling, and was originally introduced and developed by Dualis MedTech [30]. It has been tested on animal models and uses magnetic coils to wirelessly transfer power from outside to inside the body.

2.3. Radio Frequency (RF) Energy Harvesting for Implantable Applications

In this method, the RF signals are received by an antenna or antenna array and then converted into usable power, i.e., DC voltage. The RF source can be an ambient RF source, i.e., a cell phone tower, a television tower etc., or it can be a custom built source. While most of the applications of this technique are geared towards powering remote portable devices, sensors connected to internet of things etc., the merits of this technique in implantable medical devices cannot be ignored. While the RF energy harvesting system may have many modules, its basic architecture is shown in Fig. 2.5. It consists of a receiving antenna, an impedance matching circuit,

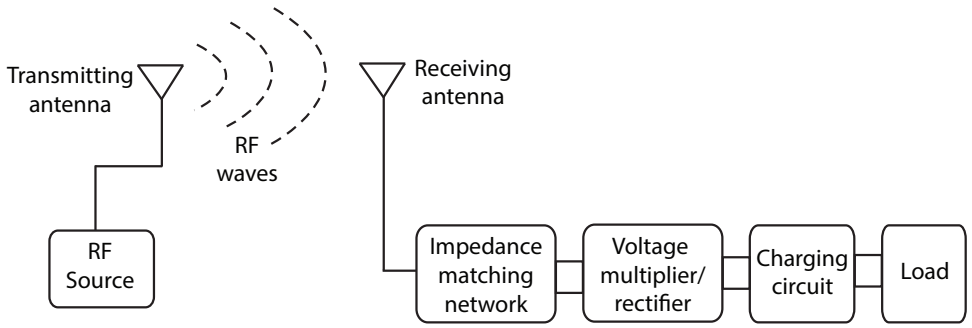

Figure 2.5. A typical layout of a wireless power transfer system using radio frequency waves.

a rectifier circuit, and also a charging circuit. These modules harvest energy from receiving RF waves and then supply it to the load, which could be a sensor or an implantable device. In case of an implantable application, the receiving antenna needs to be an implantable antenna and has to be carefully designed. Furthermore, the whole implantable device (containing the RF energy harvester) has to be enclosed in a bio-compatible enclosure due to safety and compliance considerations.

2.3.1. Related work on deeply implantable antennas

A good review of the implantable antennas designed for biomedical telemetry is summarized in [31], while a tutorial in [32] provides an analytical and complete, step-by-step guide on the numerical design, fabrication, in vitro, and in vivo testing of implantable antennas for medical telemetry applications. Implantable antennas for implantable medical devices exhibit numerous challenges in terms of design, fabrication and testing, as summarized in [31] and [33]. The guidelines for designing implantable antennas in different environments are presented in [34] and [35]. Many researchers have designed and developed different types of antennas for implantable applications including planar loops, inverted-F, monopoles, dipoles, spirals, meanders and microstrips antennas [36–47].

For cardiac telemetry, a dipole [36] and microstrip [37] embedded in the shoulder were analyzed using the finite-difference time-domain (FDTD) method. In planar implantable antennas, it has been shown that the gain of the planar antennas can be improved by making it multi-dimensional, by adding volume [38]. In [39] and [40], the use of pre-existing vascular stents as antennas has been examined, but in vivo results were not provided. It is also argued that while the

stent-antenna uses the pre-approved bio-compatible materials, it is still not ready for use in certain vessels and hence not recommended for applications in the heart chambers [40].

2.3.2. Related work on rectennas

The implantable antenna is a key component of an implantable rectenna, which consists of an implantable antenna and a rectifier circuit. An efficient rectenna is crucial for the delivery of far-field wireless power transfer. In order to improve the conversion efficiency, optimal diode RF and DC impedances for efficient rectification were obtained in [47], which help to optimize the antenna design and achieve an improved efficiency. Researchers have shown increased interest in the rectennas for applications in air [47–57], but there is limited work reported on rectennas for biomedical applications.

In [48–50], rectennas were designed for circularly polarized antennas. In [51], a high-efficiency 2.45-GHz rectenna was presented for low-input RF power. Also, a rectenna at 2.45 GHz was designed for the input power level of 0 dBm [52], while [53] reported an efficiency (RF-to-DC conversion) of only 15.7% at -20 dBm . Only few research groups have studied far-field wireless power links for biomedical applications. Marnat *et al.*, [53] designed separate transmit and receive on-chip antennas for implantable intraocular pressure monitoring applications. A triple-band implantable antenna was designed in [54] with data telemetry (402 MHz), wireless power transmission (433 MHz), and a wake-up controller (2.45 GHz). The proposed antenna can provide a conversion efficiency of 86 % when the input power is 11 dBm at 433 MHz with a 5 Ω load. In [55], a chip antenna was adopted for RF power transmission, and a resonant network consisting of a compact inductor and a chip capacitor was employed for energy harvesting. Additionally, frequency ranges for wireless power transmission into dispersive tissue was studied in [56], where the optimal frequency is above 1.0 GHz for a small receive coil and typical transmit-receive separations. In [57], a planar inverted-F antenna (PIFA) based implantable rectenna was proposed for far-field wireless power transfer applications. The antenna proposed in this method has employed a folded ground plane for size miniaturization. Also, a method of a parasitic patch over the human body was used to enhance the wireless power link and increase the received power level.

2.4. Safety Considerations of Implantable Medical Devices

Modern implantable medical devices (IMDs), especially radio frequency based IMDs are capable of real-time biomedical telemetry functionalities and can also get powered wirelessly. These

devices are offering unique possibilities in the advancement of health care but their proximity to the human body have raised many safety related questions. It should be mentioned that a RF-based IMD has additional safety-related aspects as it uses electromagnetic waves for communication or wireless power delivery. Important safety considerations for these IMDs include, (a) maximum effective radiated power in the available frequency bands, (b) maximum permissible exposure limit, (c) specific absorption limit, (d) focalized temperature limit, and (e) correct use of frequency band. Details of these mentioned parameters and also other special guidelines related to the implantable medical devices are summarized in [58–63].

2.5. Conclusion

In this chapter, a summary of related work on energy harvesting methods and various forms of wireless power transfer techniques, for implantable applications, has been presented. It is shown that most of the mentioned methods, such as kinetic harvesters, IR radiation harvesters, and low-frequency magnetic fields are not practical for some implantable applications. However, there is more potential in the application of the magnetic resonance method, and also the wireless power transfer using RF energy for implantable applications. In particular, previous work on the use of wireless power transfer using radio waves for wireless pacing is limited and therefore will be investigated in this research.

2.6. References

[1] T. Sun *et al.*, *Wireless Power Transfer for Medical Microsystems*, 1st ed. Springer, New York, USA, 2013.

[2] X. Lu *et al.*, "Wireless charging technologies: Fundamentals, standards, and network applications," *IEEE Commun. Surveys Tutorials*, vol. 18, no. 2, pp. 1413–1452, Jun. 2016.

[3] A. Kim *et al.*, "New and emerging energy sources for implantable wireless microdevices," *IEEE Access*, vol. 3, pp. 89–98, 2015.

[4] M. A. Hannan *et al.*, "Energy harvesting for the implantable biomedical devices: issues and challenges," *BioMedical Engineering OnLine*, vol. 13, no. 79, pp. 1–23, Jun. 2014.

[5] P. D. Mitcheson *et al.*, "Energy harvesting from human and machine motion for wireless electronic devices," *Proc. IEEE*, vol. 96, no. 9, pp. 1457–1486, Sept. 2008.

[6] M. Hayakawa, "Electronic wristwatch with generator," U.S. Patent 5001 685, January 24, 1991.

[7] H. Goto *et al.*, "Feasibility of using the automatic generating system for quartz watches as a leadless pacemaker power source," *Med. Biol. Eng. Comput.*, vol. 37, no. 3, pp. 377–380, 1999.

[8] R. Tashiro *et al.*, "Development of an electrostatic generator that harnesses the motion of a living body," *Int. J. Jpn. Soc. Mechan. Eng.*, vol. 43, pp. 916–922, 2000.

[9] K. Goto *et al.*, "An implantable power supply with an optically rechargeable lithium battery," *IEEE Trans. Biomed. Eng.*, vol. 48, no. 7, pp. 830–833, July 2001.

[10] K. Murakawa *et al.*, "A wireless near-infrared energy system for medical implants," *IEEE Eng. Med. Biol. Mag.*, vol. 18, no. 6, pp. 70–72, Nov. 1999.

[11] S. N. Suzuki *et al.*, "A proposal of electric power generating system for implanted medical devices," *IEEE Tran. Mag.*, vol. 35, no. 5, pp. 3586–3588, Sep. 1999.

[12] S. Suzuki *et al.*, "Electric power-generating system using magnetic coupling for deeply implanted medical electronic devices," *IEEE Trans. Mag.*, vol. 38, no. 5, pp. 3006–3008, Sep. 2002.

[13] K. Finkenzeller and D. Muller, *RFID Handbook: Fundamentals and Applications in Contactless Smart Cards, Radio Frequency Identification and Near-Field Communication.* Wiley, 2010.

[14] M. Hsia *et al.*, "An UHF passive RFID transponder using a low-power clock generator without passive components," in *IEEE Int. Midwest Symp. Circuits Syst.*, San Juan, PR, USA, 6-9 Jul., 2006.

[15] B. Smith *et al.*, "An externally powered, multichannel, implantable stimulator-telemeter for control of paralyzed muscle," *IEEE Trans. Biomed. Eng.*, vol. 45, no. 4, pp. 463–475, April 1998.

[16] B. Lenaerts and R. Puers, "An inductive power link for a wireless endoscope," *Biosensors Bioelectronics*, vol. 22, no. 7, pp. 1390 – 1395, 2007.

[17] K. M. Silay *et al.*, "Load optimization of an inductive power link for remote powering of biomedical implants," in *IEEE Int. Symp. Circuits Syst.*, Taipei, Taiwan, 24-27 May, 2009.

[18] C. Sauer *et al.*, "Power harvesting and telemetry in CMOS for implanted devices," *IEEE Trans. Circuits Syst.*, vol. 52, no. 12, pp. 2605–2613, Dec. 2005.

[19] M. Theodoridis and S. Mollov, "Distant energy transfer for artificial human implants," *IEEE Trans. Biomed. Eng.*, vol. 52, no. 11, pp. 1931–1938, Nov. 2005.

[20] Restoreulla Surescan MRI Neurostimulator. (2017, April 5). [Online]. Available: https://professional.medtronic.com/pt/neuro/scs/prod/restore-ultra-surescan/

[21] R. C. Dorf and J. A. Svoboda, *Introduction to Electric Circuits.* 8^{th} Ed. John Wiley and Sons Inc., 2010.

[22] A. Karalis *et al.*, "Efficient wireless non-radiative mid-range energy transfer," *Ann. Physics*, vol. 323, no. 1, pp. 34 – 48, 2008.

[23] A. Kurs *et al.*, "Wireless power transfer via strongly coupled magnetic resonances," *Sci.*, vol. 317, no. 1, pp. 83–86, 2007.

[24] B. Cannon *et al.*, "Magnetic resonant coupling as a potential means for wireless power transfer to multiple small receivers," *IEEE Trans. Power Electron.*, vol. 24, no. 7, pp. 1819–1825, Jul. 2009.

[25] A. Sample *et al.*, "Analysis, experimental results, and range adaptation of magnetically coupled resonators for wireless power transfer," *IEEE Trans. Ind. Electron.*, vol. 58, no. 2, pp. 544–554, Feb. 2011.

[26] A. K. RamRakhyani *et al.*, "Design and optimization of resonance-based efficient wireless power delivery systems for biomedical implants," *IEEE Trans. Biomed. Circuits Syst.*, vol. 5, no. 1, pp. 48–63, Feb. 2011.

[27] M. Kiani *et al.*, "Design and optimization of a 3-coil inductive link for efficient wireless power transmission," *IEEE Trans. Biomed. Circuits Syst.*, vol. 5, no. 6, pp. 579–591, Dec. 2011.

[28] Highly Resonant Wireless Power Transfer: Safe, Efficient, and Over Distance. (2017, April 5). [Online]. Available: http://www.witricity.com/assets/highly-resonant-power-transfer-kesler-witricity-2013.pdf

[29] Dualis MedTech and ReliantHeart Partner on Fully Implantable TET System for the Heart-Assist5® LVAD. (2017, April 5). [Online]. Available: http://www.prweb.comreleases/2015/-prweb12638371.htm

[30] Dualis MedTech GmbH. (2017, April 5). [Online]. Available: http://www.dualis-medtech.de

[31] A. Kiourti and K. Nikita, "A review of implantable patch antennas for biomedical telemetry: Challenges and solutions," *IEEE Antennas Propagat. Mag.*, vol. 54, no. 3, pp. 210–228, Jun. 2012.

[32] A. Kiourti and K. S. Nikita, "Implantable antennas: A tutorial on design, fabrication, and in vitro/in vivo testing," *IEEE Microwave*, vol. 15, no. 4, pp. 77–91, Jun. 2014.

[33] E. Chow *et al.*, "Implantable RF medical devices," *IEEE Microwave*, vol. 14, no. 4, pp. 64–73, Jun. 2013.

[34] J. Kim and Y. Rahmat-Samii, "Implanted antennas inside a human body: simulations, designs, and characterizations," *IEEE Trans. Microw. Theory Techn.*, vol. 52, no. 8, pp. 1934–1943, Aug. 2004.

[35] P. Soontornpipit *et al.*, "Design of implantable microstrip antenna for communication with medical implants," *IEEE Trans. Microw. Theory Techn.*, vol. 52, no. 8, pp. 1944–1951, Aug. 2004.

[36] C. Furse, "Designing of an antenna for pacemaker communication," *Microwave RF*, vol. 39, no. 3, pp. 73–76, Mar. 2000.

[37] J. Schuster and R. Luebbers, "An FDTD algorithm for transient propagation in biological tissue with a cole-cole dispersion relation," *IEEE Int. Symp. Antennas Propagat.*, Atlanta, GA, USA, 21-26 June, 1998.

[38] S. Soora *et al.*, "A comparison of two and three dimensional dipole antennas for an implantable retinal prosthesis," *IEEE Trans. Antennas Propag.*, vol. 56, no. 3, pp. 622–629, Mar. 2008.

[39] K. Takahata *et al.*, "Micromachined antenna stents and cuffs for monitoring intraluminal pressure and flow," *Microelectromechanical Systems, Journal of*, vol. 15, no. 5, pp. 1289–1298, Oct. 2006.

[40] E. Y. Chow *et al.*, "Fully wireless implantable cardiovascular pressure monitor integrated with a medical stent," *IEEE Trans. Biomed. Eng.*, vol. 57, no. 6, pp. 1487–1496, Jun. 2010.

[41] N. Cho *et al.*, "A planar MICS band antenna combined with a body channel communication electrode for body sensor network," *IEEE Trans. Microwave Theory Techn.*, vol. 57, no. 10, pp. 2515–2522, Oct. 2009.

[42] C. Liu *et al.*, "Compact dual-band antenna for implantable devices," *IEEE Antennas Wireless Propag. Lett.*, vol. 11, pp. 1508–1511, 2012.

[43] C. M. Lee *et al.*, "Dual-resonant Pi-shape with double L-strips PIFA for implantable biotelemetry," *Electron. Lett.*, vol. 44, pp. 1508–1511, Jul. 2008.

[44] T. Yilmaz *et al.*, "Characterization and testing of a skin mimicking material for implantable antennas operating at ISM band (2.4 GHz - 2.48 GHz)," *IEEE Antennas Wireless Propag. Lett.*, vol. 7, pp. 418–420, 2008.

[45] W. Xia *et al.*, "Performances of an implanted cavity slot antenna embedded in the human arm," *IEEE Trans. Antennas Propag.*, vol. 57, no. 4, pp. 894–899, Apr. 2009.

[46] P. Izdebski *et al.*, "Conformal ingestible capsule antenna: A novel chandelier meandered design," *IEEE Trans. Antennas Propag.*, vol. 57, no. 4, pp. 900–909, Apr. 2009.

[47] E. Falkenstein *et al.*, "Low-power wireless power delivery," *IEEE Trans. Microwave Theory Techn.*, vol. 60, no. 7, pp. 2277–2286, Jul. 2012.

[48] Z. Harouni *et al.*, "A dual circularly polarized 2.45-ghz rectenna for wireless power transmission," *IEEE Antennas Wireless Propag. Lett.*, vol. 10, pp. 306–309, 2011.

[49] M. Ali *et al.*, "A new circularly polarized rectenna for wireless power transmission and data communication," *IEEE Antennas Wireless Propag. Lett.*, vol. 4, pp. 205–208, 2005.

[50] H. Sun *et al.*, "Design of a high-efficiency 2.45 GHz rectenna for low-input-power energy harvesting," *IEEE Antennas Wireless Propag. Lett.*, vol. 11, pp. 929–932, 2012.

[51] J. A. G. Akkermans *et al.*, "Analytical models for low-power rectenna design," *IEEE Antennas Wireless Propag. Lett.*, vol. 4, pp. 187–190, 2005.

[52] A. G. Vera *et al.*, "Design of a 2.45 GHz rectenna for electromagnetic (EM) energy scavenging," in *IEEE Radio Wireless Symp.*, Jan. 2010, pp. 61–64.

[53] L. Marnat *et al.*, "On-chip implantable antennas for wireless power and data transfer in a Glaucoma-Monitoring SoC," *IEEE Antennas Wireless Propag. Lett.*, vol. 11, pp. 1671–1674, 2012.

[54] F.-J. Huang *et al.*, "Rectenna application of miniaturized implantable antenna design for triple-band biotelemetry communication," *IEEE Trans. Antennas Propag.*, vol. 59, no. 7, pp. 2646–2653, Jul. 2011.

[55] S. Hu *et al.*, "A low-cost 2.45-GHz wireless power link for biomedical devices," in *IEEE Asia-Pacific Conf. Antennas Propag.*, Singapore, 27-29 Aug., 2012.

[56] A. Poon *et al.*, "Optimal frequency for wireless power transmission into dispersive tissue," *IEEE Trans. Antennas Propag.*, vol. 58, no. 5, pp. 1739–1750, May 2010.

[57] C. Liu *et al.*, "Design and safety considerations of an implantable rectenna for far-field wireless power transfer," *IEEE Trans. Antennas Propag.*, vol. 62, no. 11, pp. 5798–5806, Nov. 2014.

[58] K. S. Nikita, "Safety issues in biomedical telemetry," in *Handbook of Biomedical Telemetry*, First ed. New Jersey: Wiley 2014., pp. 445–477.

[59] C. Liu *et al.*, "Design and safety considerations of an implantable rectenna for far-field wireless power transfer," *IEEE Trans. Antennas Propag.*, vol. 62, no. 11, pp. 5798–5806, Nov. 2014.

[60] *ETSI Standard, Electromagnetic Compatibility and Radio Spectrum Matters (ERM); Ultra Low Power Active Medical Implants (ULP-AMI) Operating in the 401 MHz to 402 MHz and 405 MHz to 406 MHz Bands; System Reference Document*, vol. V1.1.1, no. TR 102 343, 2004.

[61] *IEEE Standard for Safety Levels with Respect to Human Exposure to Radio Frequency Electromagnetic Fields, 3 kHz to 300 GHz*, IEEE standard C95.1-2005.

[62] U.S. Food and Drug Agency. (2017, March 1). [Online]. Available: https://www.fda.gov/-MedicalDevices

[63] ICNIRP, "Guidelines for limiting exposure to time-varying electric, magnetic, and electromagnetic fields (up to 300 GHz)," *Health Physics Society*, vol. 4, no. 74, pp. 494–522, Nov. 1997.

3. COMPUTATION OF AVAILABLE RF POWER INSIDE THE BODY AND PATH LOSS USING IN VIVO EXPERIMENTS

3.1. Abstract

A radio frequency (RF)-based implantable medical device (IMD) implanted deep inside a human body can be wirelessly powered using RF energy transmitted from out-inside the body. However, this wireless power transfer method experiences loss in the form of attenuation and absorption, which is caused by the lossy human body. The need of a path loss (PL) model is therefore necessary to characterize these losses. This chapter presents a novel PL model which is based on the $|S_{21}|$ measurements, obtained from a series of experiments on two different Dorset breed ovine models. Also, uncertainty analysis of the equipment used in the experiments has been performed and available radio frequency (RF) power inside the body at a proposed implant location has been computed. The results are then used to develop and propose an equivalent model for PL in an anechoic chamber. Overall, an approximate PL of $3.5\,dB/cm$ in the ovine body was measured at 1.2 GHz. Moreover, it was concluded that, with the inevitable errors in the equipment, the total PL, for 6 cm deep implant location, was approximately $21\,dB \pm 2.034\,dB$. The PL method presented in this chapter[1] is novel and has a great potential to be used for the design and development of RF-based leadless implantable devices, especially leadless pacemakers.

3.2. Introduction

Radio frequency (RF)-based implantable medical devices (IMDs) have been gaining huge consideration for monitoring, diagnosis and therapeutic procedures [1]. Some of the most crucial challenges for the RF-based IMDs are related to the modeling, designing and testing of an implantable antenna, which is an important part of the IMD and essential for communication with the external monitoring equipment [2]. In addition to the use of an implantable antenna for communications, it is also demonstrated that an implantable antenna, when integrated with a

[1] The material presented in this chapter is currently under internal review and will be submitted for publication in a peer review journal.

rectifier circuit, can also be used as an RF energy harvesting device to power an IMD, such as a pacemaker [3, 4].

An important step in the development of an RF-based IMD for human body is to understand the propagation loss. RF waves propagating from an on-body transmitter to a deeply implanted receiver antenna are attenuated considerably because human body is a lossy medium. For an implantable system, accurate link budget calculation is a critical design consideration [5], but involves various challenges, mainly due to the heterogeneous nature of the human body and its frequency dependent dielectric properties [6].

Unlike many propagation models developed for wireless applications in air, there is limited work for biomedical applications especially for deeply implanted IMDs. Furthermore, the focus of PL studies found in the literature is mainly on the characterization and optimization of on-body or in-body communication and not on the wireless power delivery inside the body. Gupta et al. presented the first results for an in-body propagation model [7]. In [8], insulated dipoles implanted in human muscle tissue were used to develop a path loss (PL) model at 2.45 GHz. Furthermore, in [9], an empirical PL model based on homogenous tissues was developed, and also, the relationship between PL and the variation of relatively permittivity ϵ_r, conductivity σ and distance was reported. Later, a multilayered medium was investigated to devise an analytical PL model, which was antenna independent model and validated only with simulations [10]. In [11], liquid phantoms using dielectric properties, similar to human muscle tissues, were used to derive PL in the human body. The use of homogenous propagation medium however limits the validity of this model. As reported in [12], modeling and characterization of PL for wireless implants has mostly been aimed for radio channels and communication links. Therefore, to better understand the RF power received at a certain implant location inside a human body, a separate investigation is necessary.

In this chapter, a novel PL model based on $|S_{21}|$ measurements, performed on ovine models, is presented. In particular, two identical horn antennas were used to study the wave propagation in the animal models and results were used to devise a PL model. In addition, an uncertainty analysis of the equipment was performed to compute the errors caused by the overall experiments. Finally, the PL was validated experimentally as well as analytically. The aim of this PL model was

to effectively estimate power received at a proposed implant location, i.e., at the heart of an ovine model.

3.3. Development of Path Loss Model

In order to develop a PL model for a practical scenario, a leadless pacemaker implanted at 6 cm deep inside an ovine model is considered as a proposed application. In order to determine and predict the power, P_r, available to an implanted leadless pacemaker on the surface of the heart of the ovine model, computations and measurements were performed as follows.

Initially, a reasonable gain for the antenna on the transmitter, denoted as G_t, used to send RF energy into the model was assumed, as well as, for the antenna on the implanted leadless pacemaker, denoted as G_r. The maximum transmit power allowed by the IEEE standards was denoted as P_t. Finally, the path loss (PL) between the transmitting antenna and the antenna on the implanted IMD was computed. Then, the following equation for computing the power available for pacing by the pacemaker was used (derived from Friis's equation [13]) :

$$P_r = P_t + G_t + G_r + PL, \tag{3.1}$$

where again P_r is the receive power (power available on the pacemaker), P_t is the transmit power (power transmitted by an on-body transmitter), G_t is the gain of the transmitting antenna, G_r is the gain of the receiving antenna on the implanted pacemaker and PL is the path loss between the transmitter and the receiver pacemaker. The gain value G_t describes the power density of the field from the transmitting antenna in any direction. The higher the value of G_t in a particular direction, the higher the power density.

For example, if $G_t = \infty$ all of the power from the transmitting antenna is focused on a single point. If $G_t = 1$ then the power density is the same in all directions from the transmit antenna. Note that all of the units in equation (3.1) are in decibels or dB. Finally, power in Watts or W can be converted to dB with the following equations:

$$P(dB) = 10 \log_{10}(P(W)/1W) \tag{3.2}$$

and

$$P(dBm) = 10\log_{10}(P(W)/1e-3). \tag{3.3}$$

This proposed PL model is based on the measurement of $|S_{21}|$, performed on the ovine models. Since the measured $|S_{21}|$ values are port quantities, equation (3.1) can be re-arranged to give the PL values in the following manner:

$$PL = P_r - P_t - G_t - G_r. \tag{3.4}$$

Next, it can be shown that

$$\left|10\log\left(\frac{P_2}{P_1}\right)\right| = \left|20\log\left(\frac{V_2}{V_1}\right)\right| \tag{3.5}$$

$$= |S_{21}|. \tag{3.6}$$

Then, expanding the left side of (3.5) gives:

$$\left|10\log\left(\frac{P_2}{P_1}\right)\right| = P_r(dBm) - P_t(dBm). \tag{3.7}$$

Substituting (3.7) into (3.5) gives:

$$|S_{21}| = P_r(dBm) - P_t(dBm). \tag{3.8}$$

Then, substituting (3.8) into (3.4) gives:

$$PL = |S_{21}| - G_t - G_r. \tag{3.9}$$

Equation (3.9) is the final equation used to compute the measured path loss (PL).

3.4. Method, Experiments and Results

3.4.1. Selection of ovine models

Large animal models such as canine, porcine and ovine are used in numerous clinical studies because these models have similar clinical features when compared to human body, and are especially favored for heart failure studies [14]. In this study, two separate adult Dorset breed ovine

models were selected and used for in vivo measurements at the Animal Nutrition and Physiology Center, North Dakota State University, ND, USA. The similarity of Dorset breed's cardiac activity and anatomy with human's heart was the primary reason behind their selection for this study. In an effort to accomodate different test subjects, two ovine models with distinct features were obtained. The first model weighed 161 *lb*, while the second model weighed 91 *lb*. To ensure the reliability of the results, all measurements were performed on freshly deceased models.

3.4.2. Experimental setup and procedure

A layout of the in vivo experiment configuration is shown in Fig. 3.1 (a). To measure the path loss and estimate power received at a certain distance inside the ovine model's body, simple wave propagation experiments were performed to measure $|S_{21}|$ in dB. The transmitting antenna TX and receiving antenna RX, as shown in Fig. 3.1 (b), were identical TDK horn antennas (1-18 GHz; model: HRN-0118). The use of these antennas had two major benefits: (1) the gain of the antennas were known and could be used in equation (3.1) for both G_t and G_r, and (2) both were wide-band antennas. Next, the distance between the antennas was denoted as D. For the measurements, the TX antenna was connected to Port 1 of a vector network analyzer with a semi-rigid coaxial cable (with a known loss) and the RX antenna was connected to Port 2 of

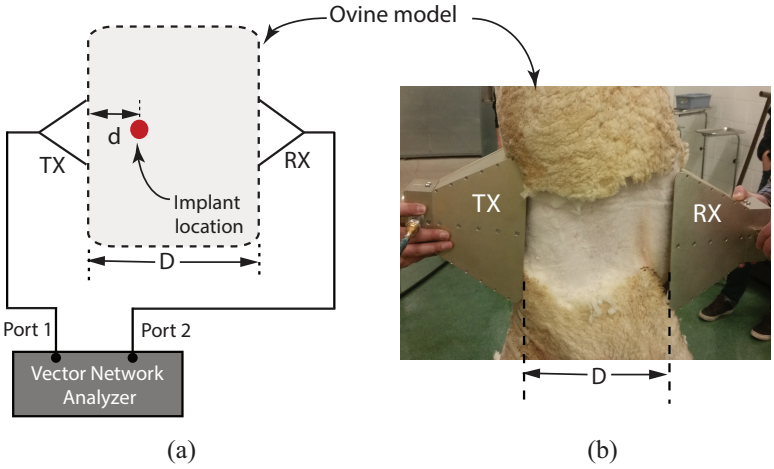

Figure 3.1. (a) A layout of the experimental setup used for path loss (PL) measurements, and (b) a close-up view of an in vivo experiment, showing transmit (TX) and receive (RX) horn antennas and part of an ovine model.

the network analyzer with an identical coaxial cable. Then, $|S_{21}|$ (dB) was measured after a full two-port calibration of the analyzer.

A procedure on how the in vivo experiments were performed is stated below:

1. Preparation of the animal model: This involved orienting the deceased model in a hanging position such that its rear legs are tied to the ceiling using a pulley and a rope. This enabled accurate measurements as the model's body was completely fixed. Furthermore, wool in the torso area was removed to enable a good coupling of antenna to the body of the model.

2. Orientation of antennas: During each experiment, both horn antennas, transmit and receive, were positioned in the same orientation, such that there was no polarization mismatch. Also, the distance in-between was measured during each experiment.

3. The magnitude of $|S_{21}|$ in dB was measured in different positions of the model, i.e., dorsal-ventral and lateral-lateral.

4. Results were saved following each measurement and repeated three times for each ovine model.

3.4.3. Results: Measured s-parameters and computation of path loss

The results of measurements performed on the first ovine model, weighing 161 lb, are shown in Fig. 3.2 (a) and (b), while the results of the measurements performed on the second ovine model, weighing 91 lb, are shown in Fig. 3.2 (c) and (d). For each model, three sets of measurements were taken in the lateral-lateral and dorsal-ventral postures. These results are in good agreement, as shown separately in Fig. 3.2 (a) and (c) and Fig. 3.2 (b) and (d).

These results show several different propagation bands that could be used for sending RF energy into the body, but the lower band, especially between 1 and 1.2 GHz, is most favorable due to its less loss. To compute the PL at 1.2 GHz, the average of the measured $|S_{21}|$ results taken in lateral-lateral posture for both the animal models, as shown in Fig. 3.2 (a) and (c), were analyzed. This decision was based upon envisioning a potential application of a leadless pacing system, as demonstrated at the frequency of 1.2 GHz in [3]. For the first ovine model, weighing 161 lb, the approximate measured distance between the horn antennas in the lateral-lateral posture was 22.0 cm. Finally, following the results of S-parameters from Fig. 3.2(a) and using the equation (3.9), the PL was computed to be approximately 3.1 dB/cm at 1.2 GHz. Similarly, the distance between the

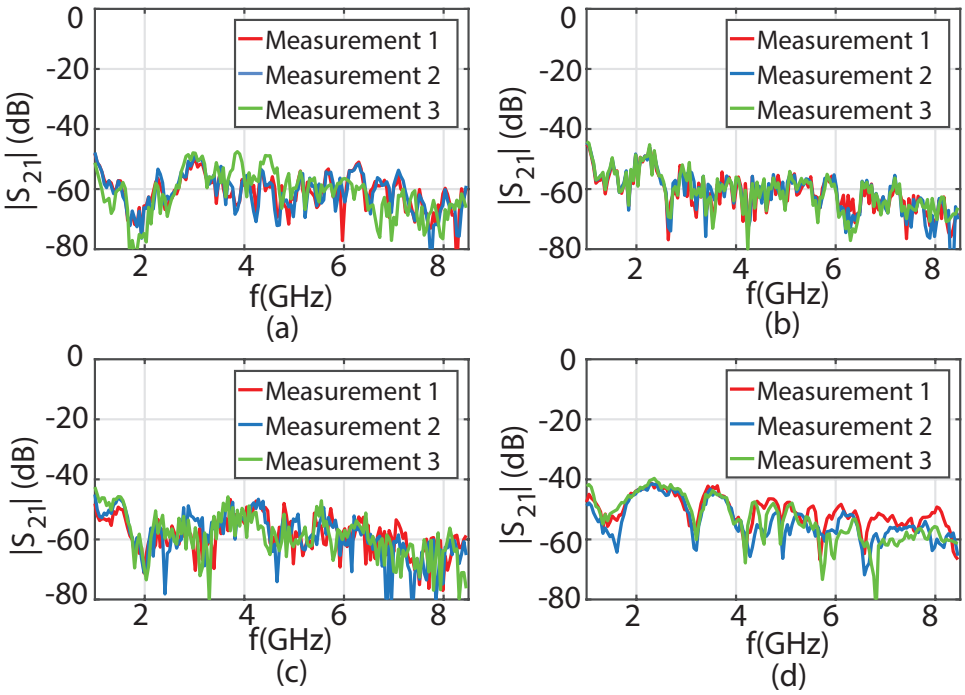

Figure 3.2. Measured results showing the magnitude of $|S_{21}|$ in dB of the (a) lateral-lateral experiment of 161 *lb* ovine model, (b) dorsal-ventral experiment of 161 *lb* ovine model, (c) lateral-lateral experiment of 91 *lb* ovine model, and (d) dorsal-ventral experiment of 91 *lb* ovine model.

horn antennas in lateral-lateral posture of the second ovine model, weighing 91 *lb*, was measured to be approximately 15.0 cm. S-parameters results from Fig. 3.2(b) were used in equation (3.9), which gave a PL value of 4.1 dB/cm at 1.2 GHz.

Because of the variations in the models and results, the average PL in this work was concluded to be 3.5 dB/cm. To predict the PL between the transmitted and the implanted pacemaker, the distance between the thorax and the heart surface (apex) was measured in a separate in vivo experiment and found to be approximately 6.0 cm. The overall PL from the transmitter to the implanted leadless pacemaker was hence computed to be approximately 21.0 dB.

3.5. Uncertainty Analysis

In order to compute the uncertainty in the path loss results, a comprehensive uncertainty analysis of the equipment, used in this study, was performed. The uncertainty analysis method was based on the technique reported in [15]. This analysis was important as it measured the inevitable errors in the experimental setup and measurements, which were then used to compute the final

Table 3.1. Details of the equipment used for the path loss study.

Equipment/Part	**Model/Details**	**Insertion Loss (IL) / Uncertainty/ Tolerance (all in dB)**
Coaxial Cable	UTIFLEX Micro-coax 26.5 GHz (6 ft.)	IL = -0.236/ft with a tolerance of ±0.0118
Network Analyzer	Agilent VNA E5071C (100 KHz-8.5 GHz)	Tolerance $T_{NA} = \pm 1.30$
Horn Antenna	TDK RF, HRN-0118 (1-18 GHz)	Gain= frequency dependent [16], Tolerance of gain $T_{G_h} = \pm 2$

values of the path loss. Table 3.1 presents important information about the equipment used in the experimental setup, which is also illustrated in Fig. 3.1(a).

The experimental setup comprised of the following equipment: a vector network analyzer, two 6 feet-long identical coaxial cables and two identical horn antennas. The insertion loss of the coaxial cables and its tolerance or uncertainty is denoted as C_l and T_{c_l}, respectively. Furthermore, the tolerance of the Vector Network Analyzer (VNA) is denoted as T_{NA}, while that of the horn antenna is denoted as T_{G_h}. Finally, the power transmitted and received by the VNA is denoted as P_{tNA} and P_{rNA}, respectively. Prior to performing the experiments, the equipment was fully calibrated and it was assumed that each respective data sheet had presented true uncertainty information.

The uncertainty of the insertion loss of the coaxial cables in watts can be computed by the following expression,

$$\pm U_{C_l} = \frac{\left| 10^{\frac{C_l + T_{C_l}}{10}} - 10^{\frac{C_l - T_{C_l}}{10}} \right|}{2}. \tag{3.10}$$

Similarly, the uncertainty of the network analyzer in watts (W) is given by the following expression,

$$\pm U_{NA} = \frac{\left| 10^{\frac{P_{tNA} + T_{NA}}{10}} - 10^{\frac{P_{tNA} - T_{NA}}{10}} \right|}{2}. \tag{3.11}$$

Also, the actual power transmitted by the VNA can be written as,

$$P_t = P_{tNA} - C_l, \tag{3.12}$$

while the actual power received by the VNA can be written as,

$$P_r = P_{rNA} - C_l. \tag{3.13}$$

Next, the uncertainty of the power transmitted by the VNA is given as,

$$U_{P_t} = \pm\sqrt{(\frac{\partial P_t}{\partial P_{tNA}} \times U_{NA})^2 - (\frac{\partial P_t}{\partial C_l} \times U_{C_l})^2}. \tag{3.14}$$

Similarly, the uncertainty of the power received by the network analyzer is given as,

$$U_{P_r} = \pm\sqrt{(\frac{\partial P_r}{\partial P_{rNA}} \times U_{NA})^2 - (\frac{\partial P_r}{\partial C_l} \times U_{C_l})^2}. \tag{3.15}$$

Using equations (3.14) and (3.15), the uncertainty for $|S_{21}|$ can be written as,

$$U_{S_{21}} = \pm\sqrt{(\frac{\partial S_{21}}{\partial P_r} \times U_{P_r})^2 - (\frac{\partial S_{21}}{\partial P_t} \times U_{P_t})^2}. \tag{3.16}$$

It should be mentioned that the gain of the given wide-band horn antennas is frequency dependent and has its own uncertainties [16]. The uncertainty for the gain of the transmit horn antenna in watts is,

$$\pm U_{G_t} = \frac{\left|10^{\frac{P_t+G_h+T_{G_h}}{10}} - 10^{\frac{P_t+G_h-T_{G_h}}{10}}\right|}{2}. \tag{3.17}$$

Similarly, the uncertainty for the gain of the receive horn antenna in watts can be written as,

$$\pm U_{G_r} = \frac{\left|10^{\frac{P_r+G_h+T_{G_h}}{10}} - 10^{\frac{P_r+G_h-T_{G_h}}{10}}\right|}{2}. \tag{3.18}$$

Finally, following the path loss equation (3.9), the uncertainty for the path loss can be expressed as follows:

$$U_{PL} = \pm\sqrt{(\frac{\partial P_L}{\partial S_{21}} \times U_{S_{21}})^2 - (\frac{\partial P_L}{\partial G_t} \times U_{G_t})^2 - (\frac{\partial P_L}{\partial G_r} \times U_{G_r})^2}. \tag{3.19}$$

The uncertainty in the PL as reflected in the measured values of $|S_{21}|$ (in dB) was calculated using a script written in MATLAB for each of the ovine model. The average of three measurements showing the magnitude of $|S_{21}|$ (in dB) and uncertainties of the lateral-lateral and dorsal-ventral experiments of 161 *lb* ovine model are plotted in Fig. 3.3 (a) and (b), respectively. Similarly, the average of three measurements showing the magnitude of $|S_{21}|$ (in dB) and uncertainties of the lateral-lateral and dorsal-ventral experiments of 91 *lb* ovine model are plotted in Fig. 3.3 (c) and (d), respectively. It should be mentioned that these results are a close-up of the uncertainties from 1 to 2 GHz only. Following the computation of the PL and available RF power from Section 3.4.3 and considering the uncertainties, the final power received at the proposed implant location is $21dB \pm 2.034\,dB$.

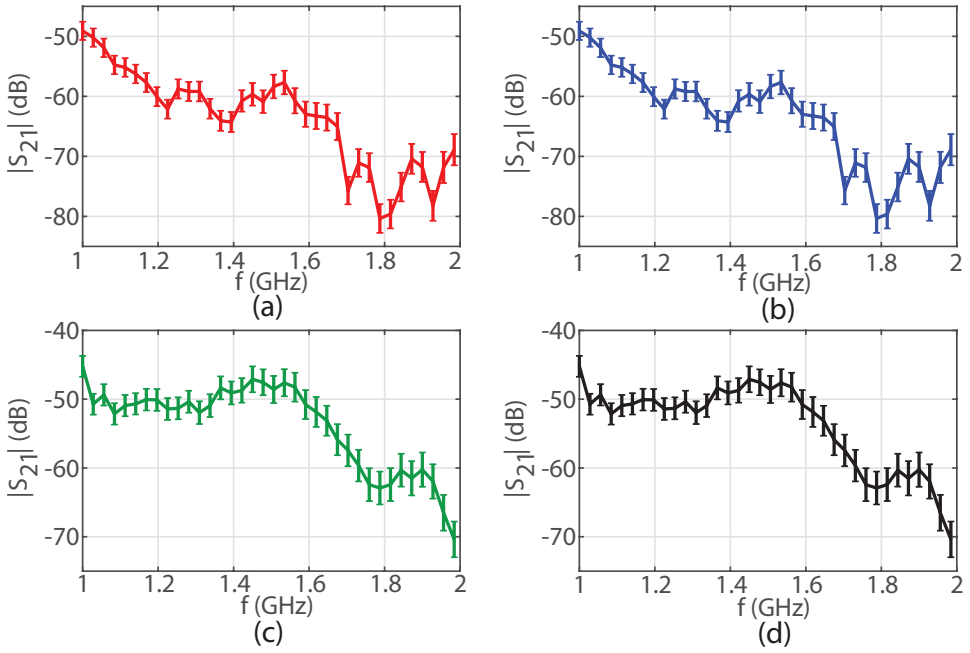

Figure 3.3. Average of three measurements, showing the magnitude of $|S_{21}|$ in dB and uncertainties of the (a) lateral-lateral experiment of 161 *lb* ovine model, (b) dorsal-ventral experiment of 161 *lb* ovine model, (c) lateral-lateral experiment of 91 *lb* ovine model, and (d) dorsal-ventral experiment of 91 *lb* ovine model.

3.6. Computation of Received Power and Validation

3.6.1. Receive power computations

A reasonable gain for the antenna on the implanted leadless pacemaker for this band and size is $-5.0\,dB$ and a reasonable gain for the transmitter (TX) antenna for the same band and size is $6.5\,dB$ (horn antenna). The gain of the TX antenna can be related to the effective aperture (A_e) of the antenna using the following equation [13]:

$$G = \frac{4\pi}{\lambda^2} A_e, \tag{3.20}$$

where λ is the wavelength in meters, G is the gain (not in dB) and the units of A_e are m^2. For a 6.5 dB gain antenna, $G = 4.46$ (solving $6.5 = 10\log(\mathrm{G})$) and the wavelength is $\lambda = (3{\times}10^8/1.2$ GHz$) = 25.0\,cm$. Solving for A_e in (3.9) then gives 221 cm^2.

Next, for continuous exposure at any frequency *f*, the IEEE standards [17] define the power density limit as $P_D = [f(MHz)/1500]\ mW/cm^2$. This then gives $P_D = 0.8$ mW/cm^2 for 1200 MHz. Therefore, for an aperture of $A_e = 221\ cm^2$ and $P_D = 0.8$ mW/cm^2, the maximum power that can be transmitted into the body is $P_t = P_D A_e = 176.8$ mW $= 22.47$ dBm. The predicted available, power deep inside the body, can now be computed using (3.1) and is given as:

$$P_r = 22.47dBm + 6.5 - 5.0 - 21.0 = 2.97dBm = 1.9mW.$$

Considering the polarization mismatch between the TX and RX antennas, and port mismatching between the horn antenna and the signal generator (caused by the biological tissue loading the aperture of the horn antenna), a correction factor of 0.25 or 25% was used. This then gave a predicted available RF power of approximately 475 μW, which was assumed for the power budget on the pacemaker designed for leadless pacing by Asif *et al.* [3].

3.6.2. Validation of the theory using Friss's equation

In order to validate the theory, the power values computed from the equation (3.5) were compared with the results of Friis's equation of the following form [13]:

$$Received\ power = P_r = P_t\left(\frac{G_t G_r \lambda^2}{(4\pi R)^2}\right), \tag{3.21}$$

where P_t was the transmitted power, while R was the distance between the transmitter and receiver antennas having gains, G_t and G_r, respectively. An experiment setup, as illustrated in Fig. 3.4, was developed in an anechoic chamber which used two identical horn antennas, HRN 0118, each to transmit (TX) and receive (RX) the power at a distance of 0.5 m.

The transmitted power was 10 dBm in the frequency band of 1 to 2.5 GHz. $|S_{21}|$ (in dB) was then measured and received power (P_r) was computed using the following equation:

$$P_r = |S_{21}| + P_t + CL, \tag{3.22}$$

where P_t was the transmitted power and CL was the measured cable loss. The measured P_r using this experiment was then compared with the computed P_r from the Friis's equation, as well as with the results from a separate experiment in which P_r was directly measured at the receiver with a spectrum analyzer (SA). The comparison of the power received using each method is presented in Fig. 3.5, which shows good agreement between the results.

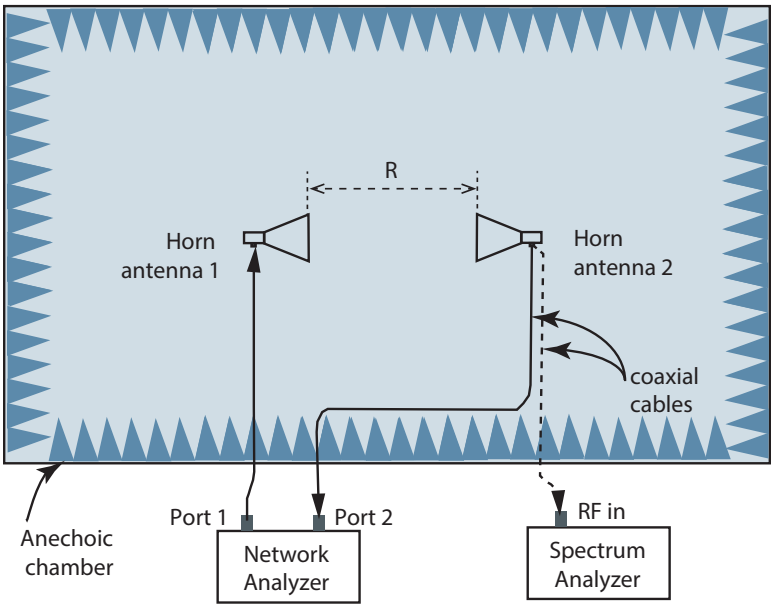

Figure 3.4. A complete layout of the experiment setup in an anechoic chamber is illustrated (R is the distance between the transmitter TX (horn antenna 1) and receiver RX (horn antenna 2)).

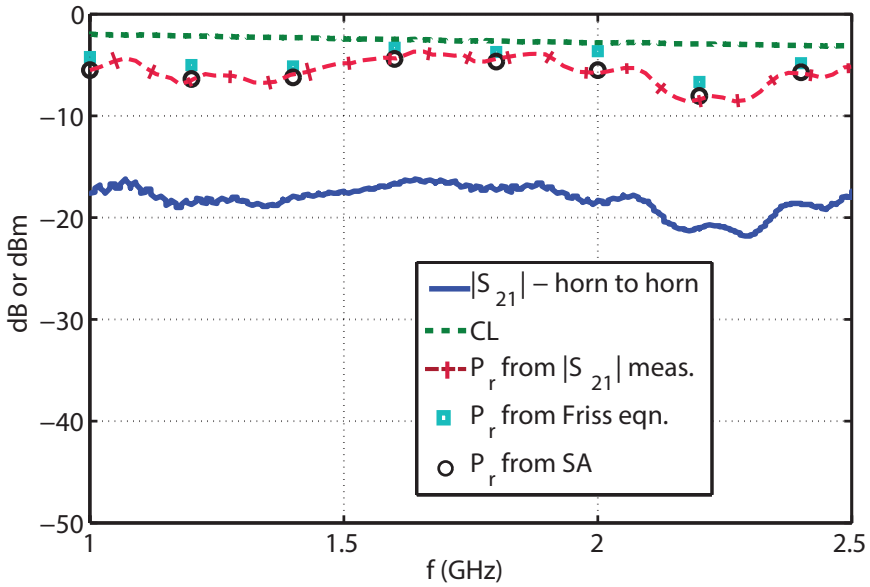

Figure 3.5. A comparison of power received using differenet methods (CL represents the cable loss).

3.7. Discussion

The available RF power (that can be received at the implant location) and path loss computations presented in this work are performed specifically for a frequency of 1.2 GHz. This method can certainly be used for other frequencies, as in vivo results ($|S_{21}|$) are measured for a frequency range of 1 GHz to 8.5 GHz. Furthermore, it is important to note that the results of the computation of power at this frequency band were demonstrated in the development of a leadless pacing system, as demonstrated in Chapter 4 [3].

In general, a specific IMD with a custom made antenna can be implanted at a certain location inside an animal model and the same PL study can be repeated. A more extensive research on this topic will certainly improve the understanding of the RF propagation for IMD applications. This is an on-going research which will be extended to study the PL in live human subject. An experimental protocol is currently being devised, which will forwarded to the Institutional Review Board (IRB) for review and approval.

3.8. Conclusion

In this work, a novel PL model, based on in vivo experiments, is proposed at 1.2 GHz. It is shown that PL model can be developed using the $|S_{21}|$ measurements using ovine models and

available Rf power at a certain implant location, inside the body, can be computed. Furthermore, variations of the results due to the uncertainty of the equipment is presented. Finally, the validity of the proposed model is validated experimentally, in an anechoice chamber, and also analytically. Moreover, it is concluded that for the given ovine models, the PL at 1.2 GHz is approximately $3.5\,dB/cm$.

3.9. References

[1] E. Chow *et al.*, "Implantable RF medical devices," *IEEE Microwave*, vol. 14, no. 4, pp. 64–73, Jun. 2013.

[2] A. Kiourti and K. Nikita, "A review of implantable patch antennas for biomedical telemetry: Challenges and solutions," *IEEE Antennas Propagat. Mag.*, vol. 54, no. 3, pp. 210–228, Jun. 2012.

[3] S. M. Asif *et al.*, "Design and in vivo test of a batteryless and fully wireless implantable asynchronous pacing system," *IEEE Trans. Biomed. Eng.*, vol. 63, no. 5, pp. 1070–1081, May 2016.

[4] S. M. Asif and B. D. Braaten, "Design of a compact implantable rectenna for wireless pacing applications," in *2016 IEEE Intl. Symp. Antennas Propag.*, Fajardo, PR, USA, 26 Jun. - 1 Jul. 2016, pp. 167–168.

[5] A. Sani *et al.*, "Numerical characterization and link budget evaluation of wireless implants considering different digital human phantoms," *IEEE Trans. Microw. Theory Techn.*, vol. 57, no. 10, pp. 2605–2613, Oct. 2009.

[6] C. Gabriel, *Compilation of the Dielectric Properties of Body Tissues at RF and Microwave Frequencies*. Brooks Air Force, TX, USA.: Tech. Rep. Report N.AL/OE-TR-. 31-CB, 1996.

[7] S. K. S. Gupta *et al.*, "Towards a propagation model for wireless biomedical applications," in *IEEE Int. Conf. Commun.*, Anchorage, AK, USA, 11-15 May, 2003.

[8] D. Kurup and W. Joseph, "Path loss model for in-body communication in homogeneous human muscle tissue," *Electron. Lett.*, vol. 45, no. 9, pp. 453–454, Apr. 2009.

[9] D. Kurup *et al.*, "In-body path loss model for homogeneous human tissues," *IEEE Trans. Electromagn. Compat.*, vol. 54, no. 3, pp. 556–564, June 2012.

[10] D. Kurup and G. Vermeeren, "In-to-out body antenna-independent path loss model for multilayered tissues and heterogeneous medium," *Sensors*, vol. 15, no. 1, pp. 408–421, Dec. 2015.

[11] R. Chavez-Santiago *et al.*, "Experimental path loss models for in-body communications within 2.36-2.5 GHz," *IEEE J. Biomed. Health Informat.*, vol. 19, no. 3, pp. 930–937, May 2015.

[12] J. Li *et al.*, "Characterization of in-body radio channels for wireless implants," *IEEE Sensors J.*, vol. 17, no. 5, pp. 1528–1537, Mar. 2017.

[13] W. L. Stutzman and G. A. Thiele, *Antenna Theory and Design*. 3rd Edition, New York: Wiley, 2012, pp. 100–127.

[14] S. R. Houser *et al.*, "Animal models of heart failure," *Circulation Research*, vol. 111, no. 1, pp. 131–150, 2012. [Online]. Available: http://circres.ahajournals.org/content/111/1/131

[15] J. W. Hansen and others., "A far-field radio-frequency experimental exposure system with unrestrained mice," *SpringerPlus*, vol. 4, pp. 1–1, Nov. 2015.

[16] TDK RF Solutions. (2017, April 10). [Online]. Available: http://www.tdkrfsolutions.com

[17] *IEEE Standard for Safety Levels with Respect to Human Exposure to Radio Frequency Electromagnetic Fields, 3 kHz to 300 GHz*, IEEE standard C95.1-2005.

4. DESIGN, DEVELOPMENT, AND IN VIVO TEST OF A FULLY WIRELESS IMPLANTABLE ASYNCHRONOUS PACEMAKER

4.1. Abstract

Goal: The aim of this study[1] is to develop a novel fully wireless and battery-less technology for cardiac pacing. *Methods*: This technology uses radio frequency (RF) energy to power the implanted electrode in the heart. An implantable electrode antenna was designed for 1.2 GHz; then, it was tested in vitro and, subsequently, integrated with the rectifier and pacing circuit to make a complete electrode. The prototype implanted electrode was tested in vivo in an ovine subject, implanting it on the epicardial surface of the left ventricle. The RF energy however was transmitted to the implanted electrode using a horn antenna positioned 25 cm above the thorax of the sheep. *Results*: It was demonstrated that a small implanted electrode can capture and harvest enough safe recommended RF energy to achieve pacing. Electrocardiogram (ECG) signals were recorded during the experiments, which demonstrated asynchronous pacing achieved at three different rates. *Conclusion*: These results show that the proposed method has great potential to be used for stimulating the heart and provides pacing, without requiring any leads or batteries. It hence has the advantage of potentially lasting indefinitely and may never require replacement during the life of the patient. *Significance*: The proposed method brings forward transformational possibilities in wireless cardiac pacing, and also in powering up the implantable devices.

4.2. Introduction

Cardiac resynchronization therapy (CRT) devices are of significance in the current era, as they have the potential to greatly improve patient outcomes. Today, more than three million people worldwide have a pacemaker and its need is even increasing, as heart failure (HF) alone affects more than 5.1 million people in the United States and 25 million worldwide [1]. Although the conventional

[1]The material presented in this chapter was co-authored by S. M. Asif, J. W. Hansen, M. S. Khan, S. D. Walden, M. O. Jensen, B. D. Braaten and D. L. Ewert. Sajid was the primary developer of the conclusion advanced here. Sajid also drafted and revised all versions of this chapter.

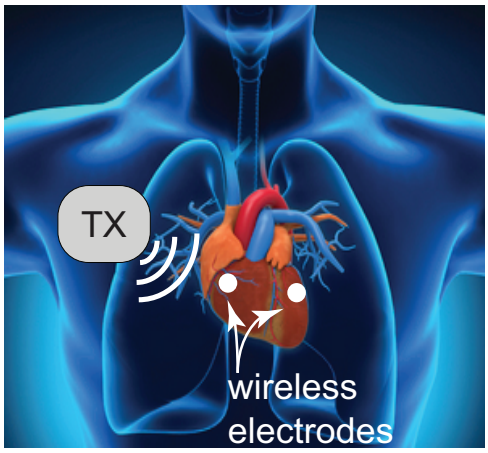

Figure 4.1. Conceptual diagram of the proposed wireless cardiac pacing system. The transmitter (TX) placed above the thorax, sends the RF signals to the implanted electrode in the heart, which is converted into DC power by the on-board rectenna to power the pacemaker and stimulate the heart tissue [14].

cardiac pacemakers improve the quality of life and reduce mortality, there are problems associated with them, due to many potential procedure- and device-related complications [2]. Amongst all components, the pacing lead is considered to be the weakest link of the cardiac pacing system, but serves as a conduit for the delivery of energy pulses to provide myocardial stimulation [3]. Leads can produce venous obstruction and are prone to insulation breaks, conductor fracture and even infection [4–7]. In addition to the lead complications, CRT is currently delivered epicardially via coronary sinus, whose anatomy can make implantation difficult to achieve the optimal pacing site [8].

Inductive Radio Frequency (RF) based pacemakers were first reported in [9, 10]. Very recently, the first ever implantation of leadless endocardial pacing using ultrasound was performed on humans [11]. Also, St. Jude [12] and Medtronic [13] have recently been developing miniaturized prototype pacemakers, which are currently going through clinical trials in Europe and the USA. Both St. Jude's Nanostim and Medtronic's Micra TPS (Transcatheter Pacing System) are the latest innovative devices for implantation in the right ventricle. However, there is still a need for a batteryless device, which would potentially make multiple site pacing practical and address the unmet clinical needs of the CRT non-responders.

The objective of this paper is to propose and demonstrate a novel method of leadless cardiac pacing, which does not require leads or electrode batteries and has the ability to pace multiple sites of the heart, not just a single chamber. This novel method, as depicted in Fig. 4.1, is achieved by exploring the integration of implantable antennas with radio frequency (RF) energy harvesting techniques to power the pacemaker for myocardial stimulation. The proposed solution has a significant advantage over all the aforementioned methods because batteries are not required for the operation of the implanted electrodes, which saves almost half of the available space. Also, the proposed technology has a significant advantage over the ultrasound system because it is completely wireless and allows multiple electrodes to be implanted without a pulse generator or pacemaker lead. This technology allows the flexibility of pacing multiple sites of the heart without the need of any leads.

In particular, this work presents the design and demonstration of a complete wireless and battery-less electrode for cardiac pacing. The electrode is comprised of an implanted rectenna, impedance matching circuit, and charging circuit, as well as a microprocessor-based pacing circuit. A detailed flow diagram of the system design is depicted in Fig. 4.2. A planar microstrip receiver antenna with complimentary split ring resonator (CSRR) loaded ground plane was first optimized for miniaturization and then matched with an efficient rectifier circuit for maximum power transfer between the rectenna and the pacing circuit. A ceramic capacitor was used to store the charge before delivering it to the pacing circuit to provide pacing and stimulate the tissue. The two layer wireless electrode prototype was fabricated in house and enclosed in a small enclosure. Finally, the wireless electrode was tested in vivo (ovine subject) to validate the concept and demonstrate the pacing. The electrocardiogram (ECG) results showed that pacing was achieved at three different rates of 110, 120 and 130 beats per minute (bpm).

Implantable antennas and energy harvesting for the implantable biomedical devices exhibit numerous challenges in terms of design, fabrication and testing, as summarized in [15–17]. The guidelines for designing implantable antennas in different environments are presented in [18, 19]. Many researchers have designed and developed different types of antennas for implantable applications including planar loops, inverted-F, monopoles, dipoles, spirals, meanders and microstrips antennas [15, 20–32]. For many years, inductive telemetry has been used to power pacemakers [33] and for data transmission in implantable applications [34, 35] but its uses have been limited by

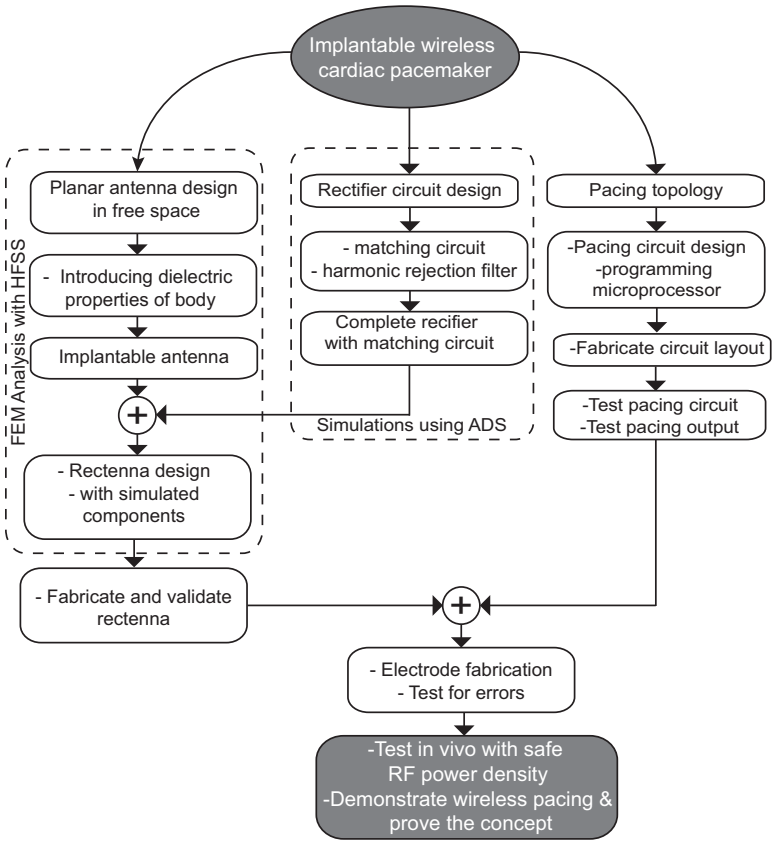

Figure 4.2. Flow diagram for the design, analysis and test of the proposed radio frequency powered wireless cardiac pacemaker system.

the quality and size of the implanted coil. For cardiac telemetry, a dipole [21] and microstrip [22] embedded in the shoulder were analyzed using the finite-difference time-domain (FDTD) method. Recently, the use of pre-existing vascular stents as antennas have been examined, but no in vivo results have been presented [24, 25]. Although the stent-antenna uses pre-approved bio-compatible materials, it is still not ready for use in certain vessels and hence not recommended to be used in the heart chambers [25]. A miniaturized circularly polarized microstrip antenna has recently been tested in pork for implantable applications [36].

The key components of an implantable rectenna are the implantable antenna, rectifier circuit and matching circuit. An efficient rectenna is crucial for the delivery of wireless power [32, 37–46]. While there has been a huge interest in the rectennas for air, limited work has been reported for implantable applications. An implantable rectenna design for triple-band biotelemetry communication has been demonstrated in vitro [43]. Marnat *et al.*, designed an on-chip antenna for

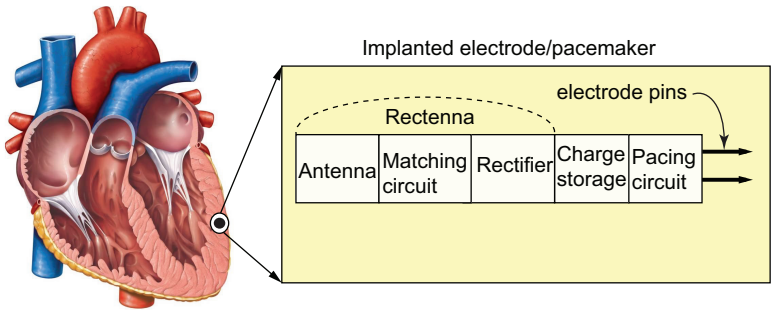

Figure 4.3. Proposed location for implanting the wireless electrode and system topology, with all the parts depicted in order [50].

wireless power and data transfer for implantable intraocular pressure monitoring applications [42]. A flexible dipole rectenna array fabricated on cellulose membrane has been proposed for biomedical applications, but has a large size and only 56 % conversion efficiency [47]. Recently, a miniature energy harvesting rectenna using PIFA (Planar inverted-F antenna) and a spiral design was proposed for deep brain stimulation but no in vivo results have been shown [48]. Previous studies described in [25] and [49] used HFSS and conducted in vivo experiments to validate the power transfer from a stent-based radiator implanted deep within the body.

This chapter is structured as follows; Section 4.3 is a preliminary section, in which the system design topology and its constraints are presented. Section 4.4 is dedicated to the selection and design of the implantable antenna, its concepts, workings, and parametric analysis. Section 4.5 discusses the topology of the rectifier circuit and its efficiency, as well as illustrates the full schematic of the system. Section 4.6 describes the pacing circuit and the load, while Section 4.7 explains the validation and fabrication of the prototype. Measurement and in vivo surgeries are described in Section 4.8, while results and discussions are summarized in Section 4.9. The paper ends with a conclusion and future work recommendations in Section 4.10.

4.3. System Design Topology and Physical Constraints

The topology configuration of the proposed implantable electrode for cardiac pacing is shown in Fig. 4.3. Designing a system with an antenna for use in the deep human body is comparatively different and more complex than designing it for air or subcutaneous applications, due to the physical constraints and electromagnetic specifications. As shown in Fig. 4.3, the antenna is not the only implant, but is a part of the complete active implantable system. Hence, it needs to

be miniaturized without compromising on its gain. Critical to its practicality, the volume of this system must be small and able to fit in a small housing. Furthermore, since the human body tissue is highly conductive and prone to the adverse tissue reaction, the device has to be embedded well in a bio-compatible insulation to avoid these issues [51–53]. Compact packaging is required to reduce the overall volume. The complete system is hence designed in layers as discussed in section 4.7. The actual antenna manufacturing process has limitations too, which have to be considered during the simulation and optimization stage.

4.4. Implantable Antenna Design

This section describes the realization of an efficient biocompatible implantable antenna at 1.2 GHz.

4.4.1. Design methodology and selection of the antenna

The intended goal was to design a linearly polarized antenna at 1.2 GHz for implantation on the heart tissue, deep inside the body. Considering the overall volume of the electrode, the antenna dimensions were set to 10×10 mm^2. To overcome all the physical and design constraints, the following design procedures were followed:

1. The antenna was designed in free space without considering any dielectric substrates and phantoms. This process helped in reducing the simulation time and allowed an approximation to select an efficient design.
2. The excitation methods were investigated and the antenna topology was selected accordingly.
3. The antenna design was tuned after adding the dielectric substrate and body phantom.
4. The antenna structure was modified to integrate the matching and rectifier circuit.

These steps are helpful to understand how we developed the design of the required antenna and achieved the final structure. Besides the miniaturization and biocompatibility, the selected antenna model should allow extensive parametrization and a good degree of freedom in the design. An extensive study of the antenna designs, such as meander line, spiral, multilayered and microstrip patch, was performed to choose an antenna structure that was efficient for the given volume and that had a fast computational performance (in free space). Following the analysis of the radiation characteristics and the concept of current distribution of these antennas [54], a microstrip patch

was selected. Microstrip patch design has a good history in implantable applications and provides flexibility in the design, shape and conformability, as reviewed in [15]. The use of a patch antenna allows several miniaturization techniques [53] that can be employed to achieve the required size and resonance frequency. The antenna having to be implanted into the heart tissue helped further in miniaturization because tissue has a higher dielectric constant than fat.

4.4.2. Human body model and numerical methods

Many possibilities of the equivalent body models are available with different complexities, as reported in [55–57]. Realization of a single body phantom for different frequency ranges is complex [58] and hence a broad frequency range was achieved only with equivalent properties of a skull in [59]. Following the recommendations in [60], a simple homogeneous cylinder with values of dielectric properties of the muscle [61]- [62] is used in this work. This is an approximation but it does provide a standard and is useful to realize conditions for the antenna measurements in less time [63]. The electric properties of the tissue model used in the simulations at 1.2 GHz are given in Table 4.1.

Table 4.1. Tissue electric properties at 1.2 GHz

Permittivity (ε_r)	Conductivity (σ [S/m])	Loss Tangent (loss δ)	Mass Density (ρ [kg/m^3])
53.4	1.0554	0.2904	1040

Performance of the antenna was examined using the properties given in Table 4.1. The antenna was implanted 6 cm under the skin, deep inside the tissue, with its ground being placed on the heart's surface. All the simulations were performed using a full wave 3D electromagnetic simulation tool, Ansoft-ANSYS High Frequency Structure Simulator (HFSS), which enabled efficient modeling of anatomical body parts. To achieve the stability of the numerical calculations and extend the radiation infinitely far, the absorbing boundaries were set at $\lambda/2$ (λ is the wavelength in tissue medium) away from the antenna in the simulation setups.

4.4.3. Miniaturization of the antenna using complimentary split ring resonator (CSRR)

Complimentary Split Ring Resonators (CSRRs) have attracted much attention and have been used extensively due to their metamaterial properties and attractive performance character-

istics [64]. Applications of metamaterials in medical imaging, microwave hyperthermia, wireless strain sensing and specific absorption rate (SAR) reduction have been reviewed recently in [65]. Applications of CSRRs for miniaturization and improving directivity have been investigated in [66]. The CSRR unit cell was introduced in the ground to miniaturize the antenna, which also facilitated a good impedance match to the source, a nearly broadside radiation pattern, and a high radiation efficiency. In addition to CSRR, several other methods have been presented in the literature to reduce the size of patch antennas, including the use of shorting posts [67], loading of reactive elements [68], and the use of reactive impedance surfaces [67]. An investigation into the design of compact patch antenna loaded with CSRR and reactive impedance surfaces, together with their performance analysis has been reported in [69]. Very recently, a combination of CSRRs and reactive pin loading has been presented in [70], which demonstrated a size reduction of 30 % and 44 %, while using CSRR alone and with the addition of active pins, respectively.

Unlike the work reported in [66], Cheng et al., proposed the use of a CSRR in the radiating patch instead and designed a compact patch antenna for wireless endoscopy [71]. Despite its proposed implantable application, the body dielectric properties were not considered in this design and also no in vitro or in vivo results were measured. A similar concept of miniaturization using the CSRR is employed in our work. We have also considered the equivalent body model with correct dielectric properties, which strongly influences the antenna design.

4.4.4. Complimentary split ring resonator unit cell

The metamaterial property of the CSRR unit cell (i.e., its negative permittivity and left handed propagation) has been realized in [64]. It is an electrically small resonator that operates as an indcutor-capacitor (LC) tank circuit with a high Q-factor, the equivalent circuit model for which is shown in Fig. 4.4. Since the electrical length of a metamaterial unit cell is much smaller than the wavelength of the operating wave, the CSRR hence becomes a useful tool for miniaturization. Changing the physical size of the CSRR unit cell changes the L_2 and C_2, as given by:

$$f_0 = \frac{1}{2\pi\sqrt{L_2 C_2}} \tag{4.1}$$

The desired resonant frequency hence can be achieved by controlling the L_2 and C_2. The layout of a patch antenna loaded with an optimized CSRR unit cell at 1.2 GHz and its dimensions are

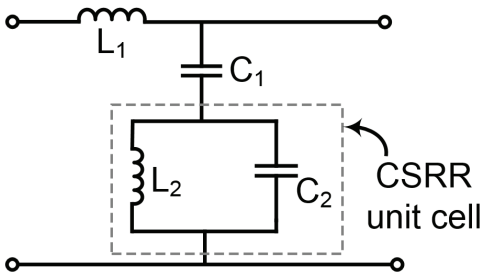

Figure 4.4. Equivalent circuit model of the complimentary split ring resonator (CSRR) unit cell [64].

illustrated in Fig. 4.5. This design layout was achieved after extensive parametrization, summarized in the next section.

4.4.5. Parametric analysis

In the first attempt, a 50 Ω matched microstrip patch antenna was designed within a 8.5×9.8 mm^2 area, which resonated at 4.6 GHz. As shown in Fig. 4.6 (a), no CSRR loading was employed in this case. Various dimensions of the CSRR were tested at all the practical locations on the ground plane to see its effects and changes on the antenna performance. Several combinations of

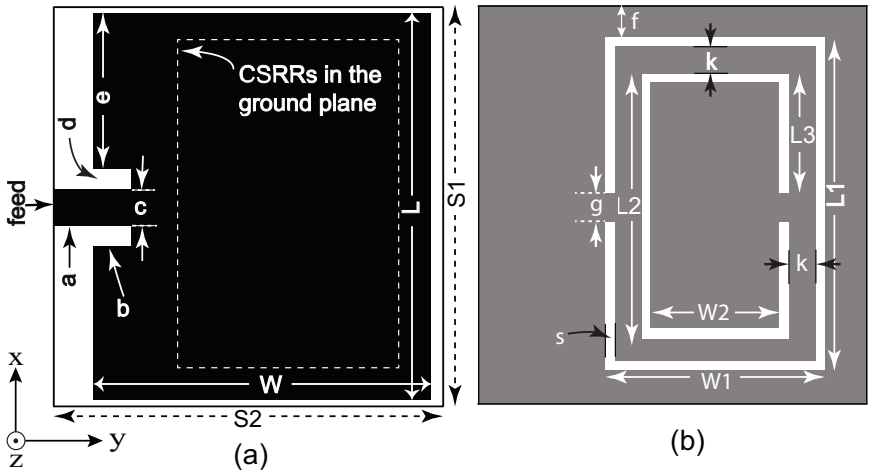

Figure 4.5. Geometry of the optimized patch antenna loaded with CSRR in the ground plane. (a) Top view and (b) bottom view. Structure characteristics are (in mm): $a = 2.3$, $b = 1.1$, $c = 1.2$, $d = 0.5$, $e = 3.8$, $W = 8.5$, $L = 9.8$, $S_1 = 10$, $S_2 = 10$, $f = 0.5$, $g = 0.6$, $s = 0.25$, $L_1 = 9$, $L_2 = 8$, $W_1 = 6.57$, $W_2 = 4.5$, $L_3 = 3.7$.

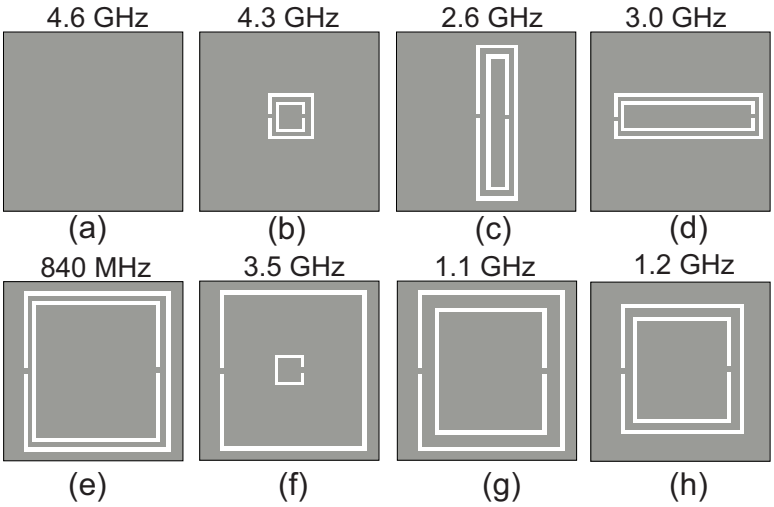

Figure 4.6. Different geometries of the CSRRs (etched in the ground plane of the same antenna), resulting in different resonant frequencies.

these geometries together with the resonant frequencies are shown in Fig. 4.6 (b) - (h). It should be noted that the substrate material used in the HFSS simulations was Rogers TMM 10i.

Initially the CSRR was etched exactly below the center of the patch with the smallest possible dimensions ($L_1 = 3.5$ mm, $W_1 = 2.5$ mm), that can be milled in house. No significant frequency shift was observed but it did however seem to be an effective method. Putting the CSRR at the center location, as shown in the Fig. 4.6 (b), provided maximum flexibility for the parametrization analysis. In order to better understand the effect of each parameter on the resonant frequency and miniaturization, let us consider the following cases:

1. *Case I- variations in the widths.* The widths W_1 and W_2 of the CSRR were extended from the center to the maximum value (W), while keeping all the other parameters constant. As a result, the resonance frequency got shifted to the lower band as the width increased but it was not very effective to achieve a resonance below 3 GHz, as shown in Fig. 4.6 (d).

2. *Case II- variations in the lengths.* Next, the lengths, L_1 and L_2 of the CSRR were increased, while keeping all the other parameters constant. This method revealed a better shift in the resonance to the lower band, as frequency as low as 2.6 GHz was achieved in this case, as shown in Fig. 4.6 (c).

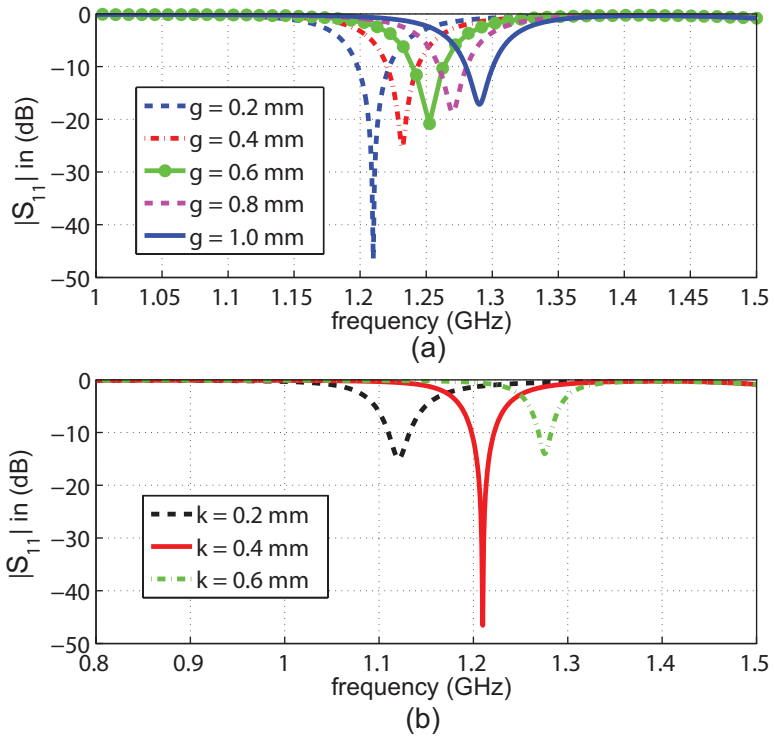

Figure 4.7. Results of the parametric analysis of the antenna. (a) Variations of the space (g), and (b) variations of the gap (k) in the CSRR.

3. *Case III- variations in the lengths and widths together.* Following the first two cases, the lengths and widths of the CSRR were then increased proportionally and found to be an effective method to achieve a lower resonance. The maximum practical dimensions of the CSRR, as shown in Fig.4.6 (e), helped the antenna resonated at 840 MHz. The parameter, *'g'* however played an important role in achieving a good match at this frequency.

4. *Case IV- variations in the gap, 'g'.* This was an important parameter in the CSRR unit cell. Fig. 4.7 (a) shows the results of the implantable antenna with variations of the gap *'g'*.

5. *Case V- variations of the space, 'k' in the CSRR.* Studying the variations of the space *'k'*, showed significant changes in the resonance frequency too. This parameter was found to be very effective in achieving the required resonance frequency of 1.2 GHz. A parametric analysis of *'k'* is shown in Fig. 4.7 (b).

4.4.6. Effects of the substrate and insulation

Substrate materials with high-permittivity properties are selected for implantable antennas because they shorten the effective wavelength and result in lower resonance frequencies. Correct use of the substrate material is hence critical in the design of the implantable antenna. Superstrate layers are however used to insulate the implantable antennas from high-permittivity tissue. The operating frequency is reported to be increased by the thicker superstrates, which also increase the physical size to refine the resonance [15]. For implantable antennas, substrates with high permittivity and superstrates with low thicknesses are hence the preferred choice. Another method to insulate the antenna is to cover the antenna with a thin layer of low-loss biocompatible coating, as reported in [20, 72]. In our design, we used Rogers TMM 10i substrate with the permittivity $\varepsilon_r = 9.8$, dissipation factor $\tan\delta = 0.0020$ and thickness $t = 1.52$ mm. Also, to keep the overall volume of the antenna to a minimum, a conformal coating was used instead of the superstrate, which did not only insulate the antenna but also helped in reducing the overall size. Effects of the proposed insulation layer, (i.e., the conformal coating) were tested experimentally to observe the changes in the performance of the antenna, but were found nominal.

4.5. Rectenna Design

4.5.1. Rectifier topology and efficiency

As shown in Fig. 4.8, two half wave rectifiers are combined to make a basic symmetrical voltage multiplier circuit. The addition of a second diode and a capacitor to the output of a standard half-wave rectifier increased its output by a set amount. Since one of the diodes is conducting in

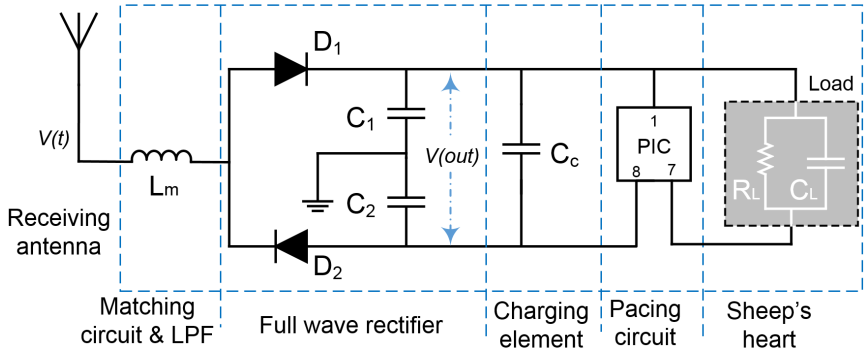

Figure 4.8. Complete block diagram with the schematic diagram of the matching circuit, full wave rectifier, charging and pacing circuits.

each half cycle as in a full wave rectifier circuit, it hence can also be called a Full Wave Series Multiplier [73]. The above mentioned rectifier circuit operates as follows. If *v(t)* is the induced voltage at the antenna port and is positive, then C_1 charges up through diode D_1 and when *v(t)* is negative, capacitor C_2 charges up through diode D_2. The output voltage *v(out)* is taken across the two series connected capacitors (C_1 and C_2).

The impedance matching stage, as shown in Fig. 4.8, is essential in providing maximum power transfer from the antenna to the rectifier circuit. Since a rectifier is a nonlinear load with complex impedance that varies with frequency hence, designing the matching network is required. As reported by [74], one design approach is to model the rectifier circuit using experimental characterization at the minimum power level required by the application. This can be achieved by measuring the input impedance of the rectifier circuit without the matching network at that power level. The results of the rectifier's input impedance from the experimental characterization helped in the design of the matching network for 50 Ω. A simple matching circuit comprising of only one inductor (12 nH) was used between the antenna and the rectifier. This inductor also served the purpose of a low pass filter, allowing RF energy at 1.2 GHz, but rejecting the unwanted higher order harmonics. Also, the use of this filter was necessary to stop the radiation of harmonics generated by the non linear diodes, required for the rectification.

Fig. 4.9 depicts the efficiency (η) of the full wave series multiplier circuit, which was measured using the fabricated prototype. The experimental setup for measuring the η included two horn antennas (HRN-0118, TDK), each used to transmit and receive the continuous sinusoidal signal, generated by the Agilent N5181A (Analog Signal Generator). η was measured as a function of the input RF power from -10 to 15 dBm and calculated using the following formula,

$$\eta = \frac{Harvested\,Power\,(DC)}{Input\,RF\,Power\,to\,the\,Rectifier} = \frac{P_{DC}}{P_{RF}}. \tag{4.2}$$

For most rectifier circuits, η changes with the RF input power, impedance matching, operating frequency, and diode properties. In this work, the operating frequency was kept constant at 1.2 GHz, and also two identical diodes were chosen, while the power was altered to get the efficiency characteristics.

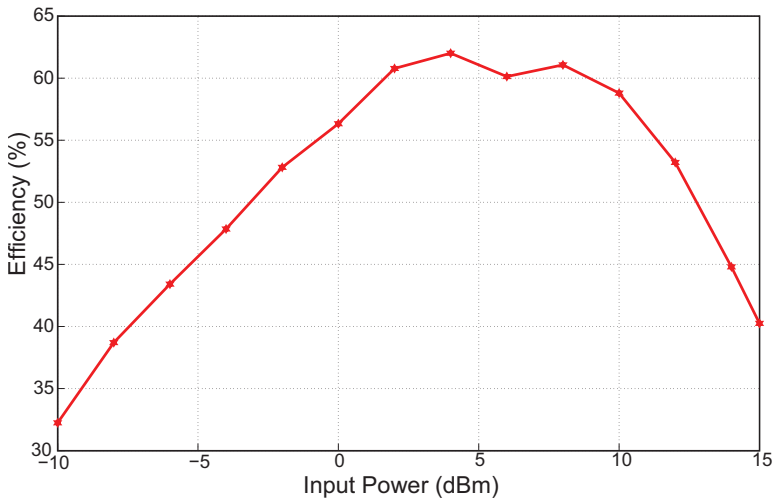

Figure 4.9. Measured efficiency (η) of the rectifier circuit at 1.2 GHz.

4.6. Pacing and Charging Circuit

4.6.1. Pacing circuit

The asynchronous, non-demand pacing signal was generated using an 8-bit PIC microcontroller, PIC12LF1840 [75], as shown in Fig. 4.8. The turn-on voltage for the microcontroller was 1.8 V, but it was programmed to remain in the sleep mode for the first second. The heart rate of a sedated ovine model has been reported to be 100 beats per minute (bpm) [76], so the pacing signal was hence generated at a higher rate to observe the changes in the cardiac rhythm. In order to test and overdrive the heart, the selected rates were chosen higher than 100 bpm but not too high to drive the ventricular fibrillation. Measurements of the three sets of successive, but different paced rhythms, generated during this study have been shown in Fig. 4.10, and summarized as follows:

1. *Rhythm I- 110 bpm.* 18 pulses were first generated, as the PIC paced for 1 msec each time, while went to sleep for 544 msec in each cycle. This resulted in $(1/\,0.545)\times 60 = 110.1\,(\approx 110)$ bpm.

2. *Rhythm II- 120 bpm.* Next, 20 pulses were generated, where the PIC paced for 1 msec, but remained in sleep mode for 496 msec in each cycle. This combination hence resulted in $(1/\,0.496)\times 60 = 120.7\,(\approx 120)$ bpm.

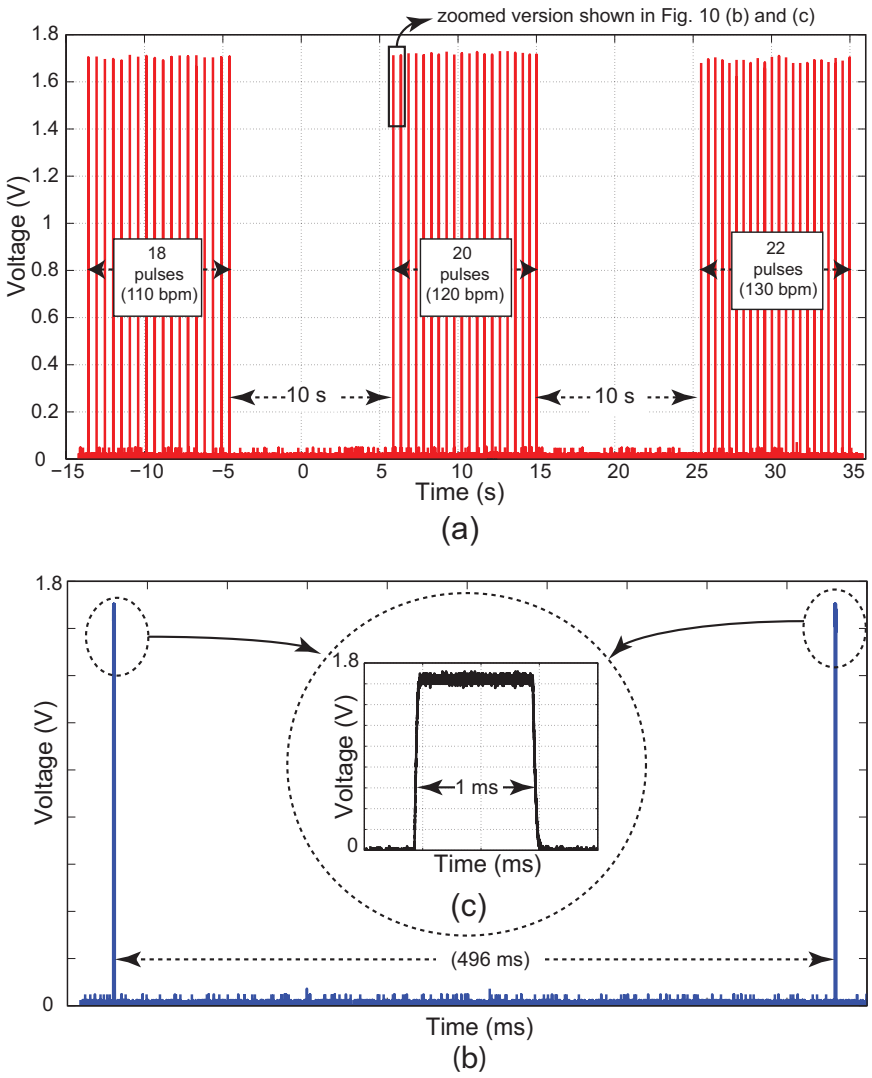

Figure 4.10. Measured pacing profile showing, (a) a complete pacing cycle including 18, 20 and 22 pulses, (b) two (out of 20) pulses with the time (496 msec) between them, generating 120 bpm, and (c) profile of a single pulse, its voltage level (1.7 V) and width (1 ms).

3. *Rhythm III - 130 bpm.* Finally, 22 pulses were generated, where the PIC paced for 1 msec but slept for 456 msec in each cycle. This resulted in $(1/\,0.456)\times 60 = 131.3\ (\approx 130)$ bpm.

4.6.2. Charging circuit and the load

Next, the output DC voltage of the rectenna was supplied to a bulk capacitor C_c, which was placed across the output of the rectifier circuit and in parallel to the load (which also contains the microprocessor), as shown in Fig. 4.8. This capacitor charges up when the voltage from the rectifier

rises above that of the capacitor and provides the required current from the stored charge, when the rectifier voltage falls. For a full wave rectifier (FWR), the ripple voltage is estimated using, $V_{ripple} = I_{load} / (2fC)$. This equation provides sufficient accuracy for our load, which draws only 30μA [75]. Although, the capacitor discharge behavior for a purely resistive load is exponential, the inaccuracy introduced by the linear approximation is very small for low values of the ripples. The total load of our system is not only the pacing circuit, but it is the combination of the pacing circuit and the impedance of the heart tissue. A good approximation of the impedance of the heart tissue has hence to be determined.

An initial experiment on the heart of an ovine model was performed to approximate the impedance of the heart tissue. A $100\,\Omega$ resistor was connected in series with the heart tissue, using two test probe pins (8 mm apart) inserted at the left ventricle. Next, a digital signal (amplitude = 1 volt, frequency = 5 KHz) was supplied to the series connected resistor and the heart tissue and voltages measured. A complete profile of voltage and current was recorded and finally, a Fast Fourier Transformation (FFT) was performed on the recorded signals using ohm's law ($fft(V_{heart})/fft(I_{100\Omega})$) to compute the impedance. The fft impedance plot showed the spectral contents with 0^{th} harmonic (real impedance) and other higher order harmonics (imaginary impedance). The computed values were found to be, $R = 665\,\Omega$ *and* $C = 59.3\,nF$, which was the impedance (approx.) of the heart tissue during the pacing.

4.7. Validation and Fabrication of the Battery-less and Wireless Prototype Implantable Electrode

4.7.1. Validation of the rectenna in HFSS

The implantable antenna designed and discussed in Section 4.4 was integrated with the rectifier circuit, discussed in Section 4.5. To accommodate the rectifier and matching circuit on the same substrate, the overall antenna dimensions were increased by extending the antenna in the -y axis (direction) and cutting the microstrip feed short. To validate the design, all the additional components, (i.e., the matching inductor (L_m), the diodes (D_1, D_2) and the capacitors (C_1, C_2)) were simulated as lumped components in HFSS to minimize the error in measurements. This process incurred a mismatch and also shifted the resonance frequency to a higher band. It is to be noted that the size of the radiating patch was not changed and was kept the same as previously mentioned in Fig. 4.5. The CSRR parameters in the ground plane were finally modified to re-achieve

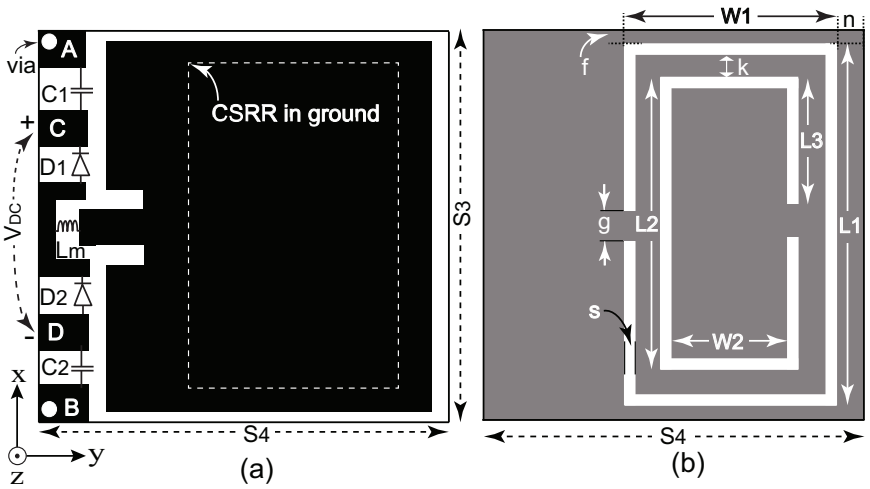

Figure 4.11. Complete layout configuration of the rectenna. (a) Top view-antenna, matching and the rectifier circuit (D_1,D_2 are the diodes, C_1, C_2 are the capacitors and L_m is the matching inductor), and (b) bottom view-final geometry of the CSRR. Structure characteristics are (in mm): $g = 0.6$, $f = s = 0.25$, $k = 0.5$, $W_1 = 7.4$, $W_2 = 5$, $L_1 = 9.5$, $L_2 = 8$, $L_3 = 3.7$, $n = 0.4$.

a good impedance match at 1.2 GHz. The final layout configuration, together with the rectifier and matching components has been illustrated in Fig. 4.11.

As depicted in Fig. 4.11 (a), two vias (0.2 mm in radius) were made in pads A and B, to connect the capacitors C_1 and C_2, respectively to the ground. The rectified output DC voltage was received between the pads C and D, which eventually was supplied to the pacing circuit (layer 2) beneath the antenna, as discussed in Section 4.7.3.

4.7.2. Effects of the pacing circuit's substrate on the implantable antenna

As discussed earlier in this section, the pacing circuit had to be glued directly beneath the antenna, making it a two layer design. The dielectric properties of the pacing circuit board (substrate) would hence strongly influence the performance of the antenna and had hence been analyzed prior to its selection. Various substrates (i.e., TMM 4, TMM 6, TMM 10i and TMM 13i with different dielectric properties, $\varepsilon_r = 4.5$, 6.02, 9.8 and 10.2), respectively were used to study the dielectric loading and results were compared and analyzed. As shown in Fig. 4.12, the use of TMM 13i showed good results and was hence finally selected as a substrate for the pacing circuit.

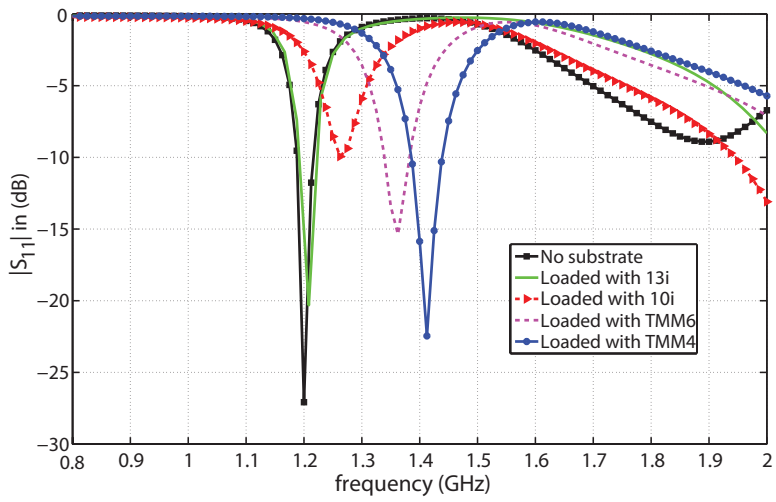

Figure 4.12. Study of the dielectric loading of the implantable antenna with different substrates, having different permittivity values.

The resonant frequency of the implantable antenna shifted to a higher band, when it was loaded with a substrate of low permittivity values but remained unchanged, when loaded with TMM 13i, having $\varepsilon_r = 10.2$. It was observed that the smaller the permittivity of the substrate, the higher the shift in the resonance frequency incurred. As a result, Rogers TMM 13i was used for the pacing circuit fabrication.

4.7.3. Prototype fabrication approach

A step-by-step assembly process of the prototype fabrication approach is shown in Fig. 4.13 (a). As seen in Fig. 4.13, the rectenna and the matching circuit were fabricated on layer 1, which sat atop layer 2, containing the pacing circuit and the charging capacitor, C_c. As depicted in the Figs. 4.13 (a), (b) and (c), the rectified DC voltage was supplied to the bottom of layer 2, to the charging capacitor and to supply power to the pacing circuit. Layers 1 and 2 were eventually bonded together using super glue (Loctite). Finally, the back probe pins were soldered in place to the output of the pacing circuit and tips sharpened for easy implantation. The assembled electrode, as shown in Fig. 4.13 (c), was then secured in the 3D printed enclosure and insulated using a conformal coating and allowed to dry at room temperature. Various parts of the prototype electrode and a complete manufactured electrode is shown in Fig. 4.14.

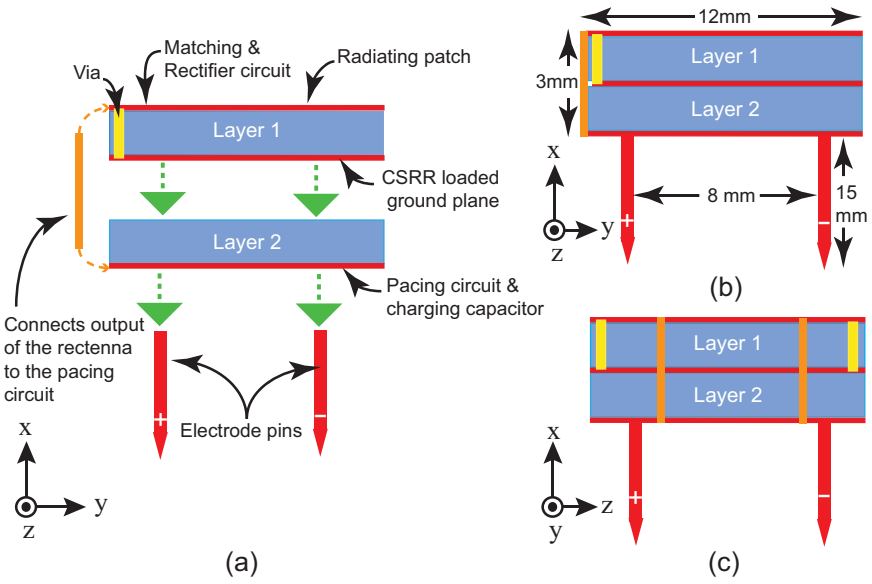

Figure 4.13. Assembly process of the prototype. (a) Step-by-step assembly process of the rectenna with the pacing board and the electrode pins. (b) Assembled prototype and its dimensions shown. (c) Different orientation of the assembled prototype, showing the DC voltage connection from the top layer to the bottom of the second layer.

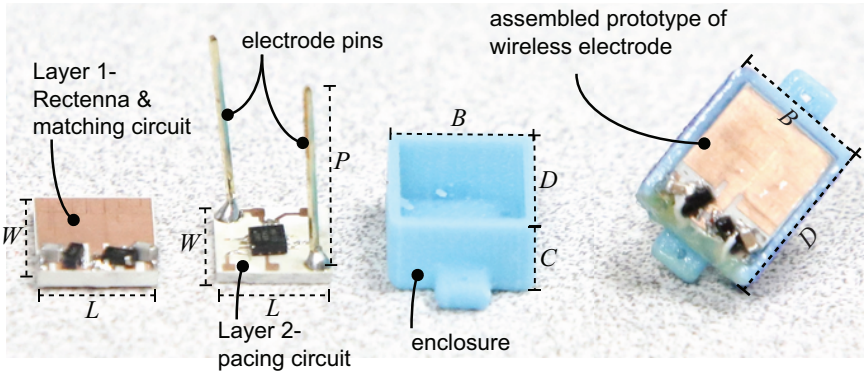

Figure 4.14. Various pictures of the fabricated prototype electrode. Dimensions are (in mm): $W = 12$, $L = 10$, $P = 15$, $B = 12.4$, $C = 4.5$, and $D = 14.4$.

The rectenna as well as the pacing circuit was fabricated using the LPKF milling maching (Protomat S63) on TMM 10i and TMM 13i, respectively. The 3D printed enclosure, which house the antenna and the pacing circuit was designed in Solidworks and printed in house. Details of all the components of the manufactured prototype wireless electrode are shown in Table 4.2.

Table 4.2. Details of all the components used to manufacture a prototype leadless pacemaker.

Component / Part	**Model / Details**
Rectenna substrate	Rogers TMM 10i, thickness = 1.52mm, Cu thickness = 35μm, $\varepsilon_r = 9.8$
Pacing circuit substrate	Rogers TMM 13i, thickness = 1.52mm, Cu thickness = 35μm, $\varepsilon_r = 10.2$
Capacitors - C_1, C_2	120 pF, SMD 0603-Ceramic, High Q (251R15S221JV4S)
Inductor - L_m	12 nH, 0402, High Frequency- Ceramic, L-07C27NJV6S
Diodes - D_1, D_2	Avago-HSMS 2850 zero bias Schottky detector diode
Capacitor - C_c	4 μF, SMD 0402-Ceramic, High Q (LLL1U4R60G435ME22L), Murata
Microprocessor	PIC12(L)F1840, SMD 8-Pin Flash, Microchip Technology
Pins	Back Probe Pins, Pamona Electronics 6411, 501-1678-ND
Enclosure	Thermoplastic, ABS plus-P430, Stratasys

4.7.4. In vitro measurements and results

The final version of the insulated implanted antenna (only, i.e., without the rectifier circuit) was tested in a porcine tissue. All measurements were taken using a calibrated Agilent E5071C ENA Network Analyzer, in an anechoic chamber. The measured return loss was compared with the simulations and found in good agreement, as shown in Fig. 4.15 (a). HFSS simulations showed a return loss of -26 dB at 1.2 GHz, while the measured return loss was -17 dB at 1.25 GHz, which showed agreement within 1.04 %. Also, simulated and measured normalized radiation patterns in *xz (H)* - and *yz (E)* - planes have been presented in Fig. 4.15 (b) and (c), which showed good agreement. Furthermore, the simulated actual maximum gain and simulated realized gain of the proposed antenna was 0.58 and 0.53 dBi, but the measured realized gain was -1.5 dBi. The slight frequency shift was attributed in part to the fabrication imperfection associated with the resolution of the milling machine and to the difference in electrical properties of the tissue.

4.8. Measurement and In Vivo Surgeries

To explore how using the ovine subject would affect the performance of the prototype wireless electrode in the human body, collaboration was developed with the Animal Nutrition & Physiology Center (ANPC) at NDSU. The in vivo measurements were performed in two models, 8 and 4 year old adult of dorset breed. The models weighed 129 and 143 lb, respectively. Dorset models are often used as research subjects as their cardiac activity and especially the coronory anatomy of their hearts are similar to the anatomy of the human heart. They hence have been

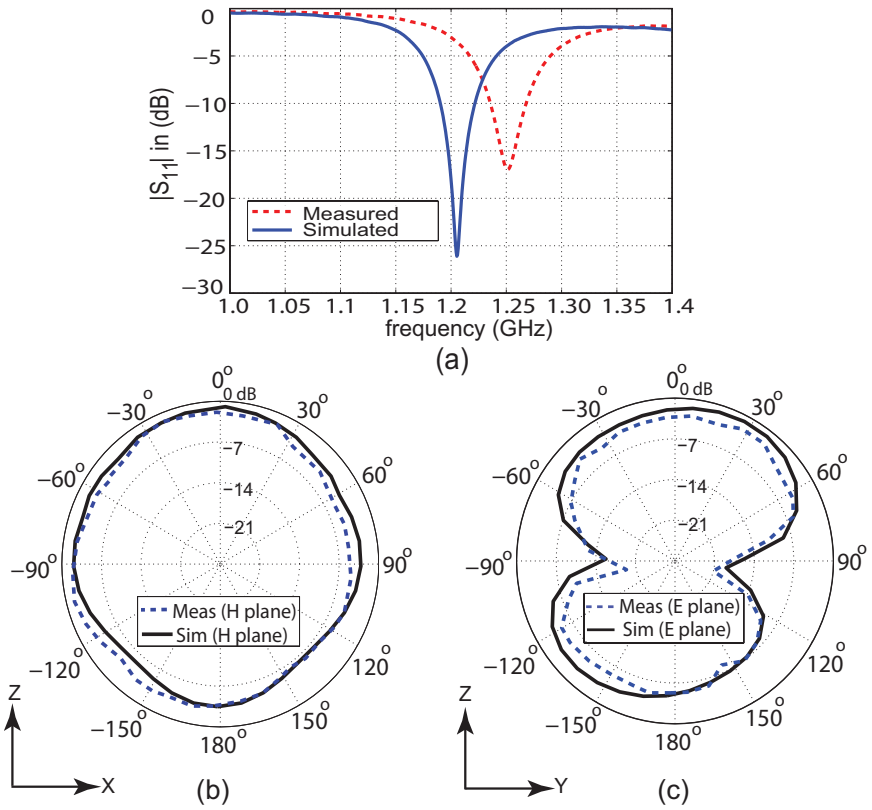

Figure 4.15. Simulated and measured (in vitro) results of the implantable antenna. (a) Matching performance ($|S_{11}|$ in dB), (b) Normalized radiation pattern in *xz (H)*-plane, and (c) Normalized radiation pattern in *yz (E)*-plane.

a preferred choice for research in the heart failure treatment [77]. All the surgical procedures and in vivo measurements were carried out in accordance with the Institutional Animal Care and Use Committee (IACUC) protocol (No. A15028). For long-term in vivo studies, the implantable systems need be enclosed in a medical-grade biocompatible material but a toulene and xylene free conformal coating was used to insulate the implantable electrode in this short-term acute animal study.

A complete blood count (CBC) and metabolic panel was conducted and examined before the animal was declared fit and suitable to be used for the study. During the surgery, a combination of IV Ketamine (5 mg/kg) and Valium (0.25 mg/kg) were used for the anesthetic induction. In each experiment, the sheep was intubated, with an endotracheal tube and maintained under the anesthesia with Isoflurane (0-5 %) under positive ventilation. The sheep was continuously monitored to assure surgical plane of anesthesia by heart rate, blood pressure, respiratory rate, O_2 saturation,

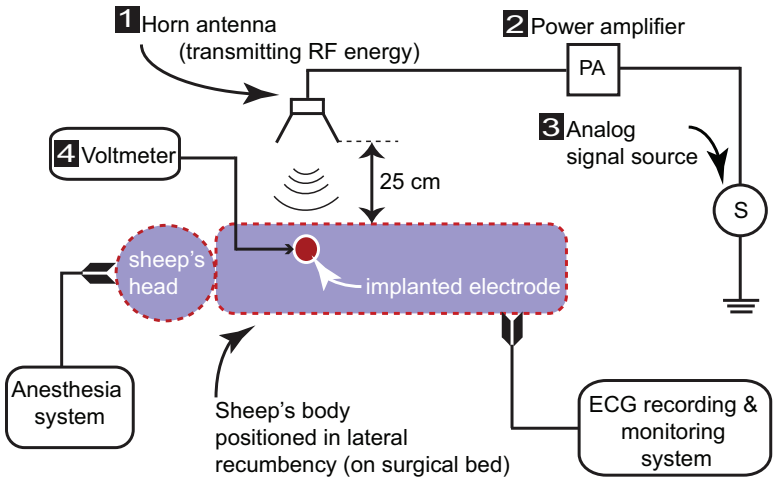

Figure 4.16. Layout of the in vivo experiment setup and RF energy transmission method with exterior system. Details of the equipment used in the exterior system are: 1 - Horn antenna = TDK-HRN-0118, 2 - Power amplifier = Mini-Circuits (ZHL-30W-252-S+), and 3 - Analog signal source = Agilent-N5181A.

and capnometry (exhaled CO_2 levels) at 35-45 mmHg as well as jaw tone, ocular and palpebral reflexes.

Following adequate general anesthesia, the ovine subject was positioned in the right lateral decubitus (recumbency) position and an antero-lateral left thoracotomy was performed. To gain access to the left thorax, the extremities were positioned and held in place using rope. The left chest was shaved with a no. 40 clipper blade and three alternating scrubs using betadine followed by an alcohol rinse were used to prep the surgical site. After site preparation, surgical drapes and lighting were setup and incandescent lights were used to maintain the body temperature.

For in vivo studies, our experimental and surgical setup, shown in Fig. 5.14, consists of the ovine test subject, horn antenna, power amplifier, signal generator and a voltmeter. The implantation of our wireless electrode began with the incision made on the front and left side of the chest of the selected model. The incision was carried down to the ribs using a muscle splitting technique and the seventh interspace was entered into the pleural space. Next, the pericardium was incised vertically and the heart was delivered into the pleural space, taking care not to compromise venous return. Cautery was disconnected at this time to avoid damage to the electrode once it was implanted.

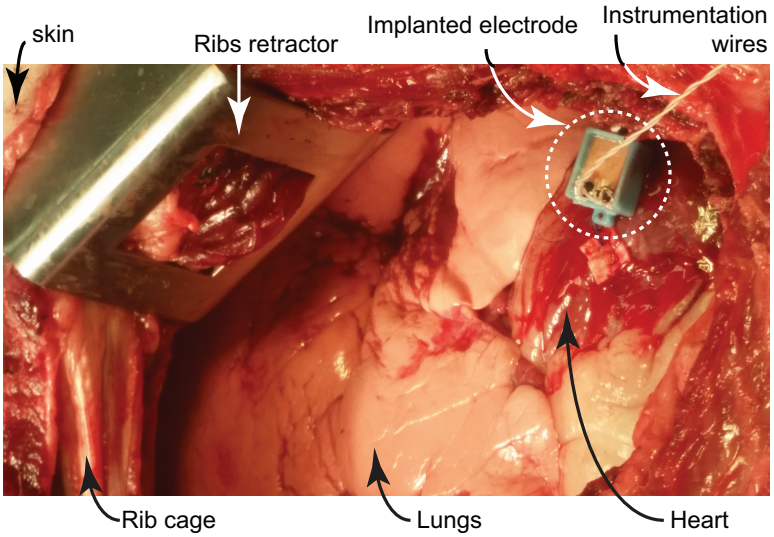

Figure 4.17. Picture of the open-thorax of the sheep, showing implanted electrode secured on the epicardial surface with surgical suture. Instrumentation wires, used to monitor the harvested voltage by the implanted electrode can be seen.

The heart was examined and a clear area was located to the left of the LAD (left anterior descending coronary artery), on the epicardial surface of the left ventricle. This flat area above the apex was selected to insert the electrode pins directly into the myocardium. Two previously placed non-conductive pledgeted prolene 5-0 sutures were placed through small plastic loops, located on the sides of the electrode's enclosure for stabilization. Instrumentation wires from the electrode were gently brought through the medial aspect of the thoracotomy to monitor the rectified voltage harvested by the implanted electrode, as shown in Fig. 4.17. Once the electrode was implanted and secured, a rib approximator was used to complete the cardiothoracic procedure and the chest was sealed with a vicryl (Ethicon Inc.) suture.

4.9. Results and Discussion

The results from the in vivo studies validated the ability of the wireless electrode, implanted deep inside the body of the model to receive the RF energy and harvest it to provide enough power for the microprocessor to provide pacing. As shown in the layout (Fig. 5.14), the horn antenna was placed approximately 25 cm above the thorax and supplied the RF energy to the implanted pacemaker. The distance of 25 cm was the maximum allowed to power and interrogate the implant under the safe level of RF exposure, as summarized in [78]. In our in vivo studies, pacing at three

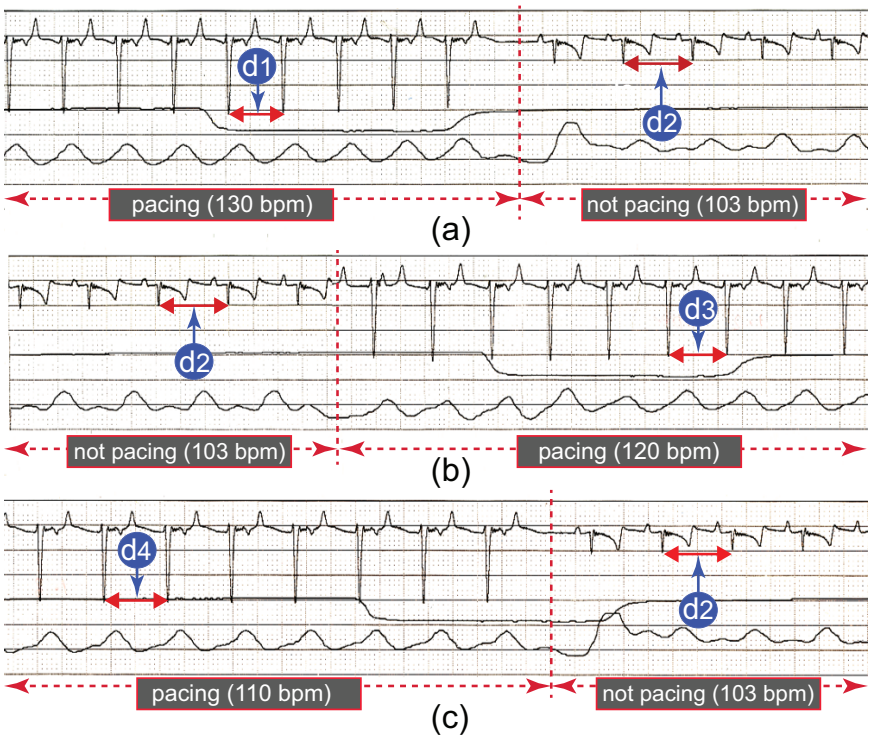

Figure 4.18. Electrocardiogram (ECG) results showing native heart beat, as well as pacing achieved at different rates, i.e., (a) 130 bpm ($d_1 = 11.5$ mm (≈ 0.46 sec), and $d_2 = 14.5$ mm (≈ 0.58 sec)), (b) 120 bpm (d_3=12.5 mm (≈ 0.49 sec)), and (c) 110 bpm ($d_4 = 13.5$ mm (≈ 0.54 sec)). Paper speed is 25 mm / sec.

different rates, 110, 120 and 130 bpm were achieved and demonstrated. These results were measured live and saved using a six lead ECG module connected to the ovine model during the course of the experiment. Some results are shown in Fig. 4.18. IEEE limits for the maximum permissible exposure (MPE) in the controlled environment [78] were followed and the safe power density at the operating frequency of 1.2 GHz was computed as , $1200\,MHz/1500 = 0.8\,mW/cm^2$. In our experimental setup, the power density S, incident on the surface of the thorax was computed using the following formula [79],

$$S = \frac{G_t P_t}{4\pi R^2}. \tag{4.3}$$

G_t(= 6.5 dBi) was the gain of the horn antenna at 1.2 GHz, while P_t (= 10 dBm) was the approximate power transmitted from the horn, which also included the gain of the power amplifier. R was the distance between the horn and the thorax, which was measured to be 25 cm (approx). The power density using these values was computed to be 0.0082 mW/cm^2, which was well under

the required safe level and hence met the MPE specifications. Furthermore, an analytical derivation of the SAR and its relationship with power density is presented in Appendix A. Some additional pictures of the fabricated prototype leadless pacemaker are shown in Appendix B.

Energy transmission using a horn antenna, held on the top of a subject might not seem practical, but the aim of this work was to prove the concept of the wireless energy transfer in vivo and the feasibility of wireless cardiac pacing. It is envisioned that the clinical use of our system will require; (a) a wearable battery operated transmitter system with a miniaturized conformal antenna, and (b) a miniaturized cylindrical shaped biocompatible electrode that can be fully inserted into the myocardium. Furthermore, the operation frequency of 1.2 GHz was used because a set of preliminary experiments indicated that this frequency produced good propagation through the tissue and also, this frequency matched efficient performance of the available Schottky diodes, which resulted in a more efficient rectifier circuit.

4.10. Conclusion and Future Work

This chapter considers the problem of leads and batteries required for the conventional cardiac pacemakers and presents the design and in vivo test of a battery-less and fully wireless implantable asynchronous cardiac pacemaker. The prototype implanted electrode has been successfully tested on the left ventricle of an ovine model. It is shown that a small implanted pacemaker can be wirelessly powered using an external radio frequency (RF) source and can provide leadless pacing. Pacing at three different rates (110, 120, 130 bpm) has been achieved and demonstrated in this work. This proposed RF powered wireless cardiac system employs a unique technique, which completely eliminates the use of the leads and batteries in cardiac pacing. This method provides a new frontier of research in wireless cardiac pacing, which may be extended to other areas in the wireless biomedical sensors. Once clinically proven, this technology has the potential to allow multiple electrodes to be implanted in the heart, without the need for any leads or batteries.

Future work will include further miniaturization, and also the design and test of the electrode for Industrial, Scientific and Medical (ISM) bands. Moreover, we will investigate the efficiency of the Complimentary Split Ring Resonator (CSRR) antenna for different subjects and study its effects on the pacemaker performance.

4.11. References

[1] Centers for Disease Control and Prevention, Atlanta GA, USA. [Online]. Available: http://-www.cdc.gov/heartdisease/facts.htm

[2] K. L. Lee, "In the wireless era: leadless pacing," *Expert Rev. of Cardiovascular Therapy*, vol. 8, no. 2, pp. 171–174, 2010.

[3] R. E. Kirkfeldt *et al.*, "Risk factors for lead complications in cardiac pacing: A population-based cohort study of 28,860 Danish patients," *Heart Rhythm*, vol. 8, no. 10, pp. 1622–1628, 2011.

[4] R. G. Hauser *et al.*, "Clinical experience with pacemaker pulse generators and transvenous leads: An 8-year prospective multicenter study," *Heart Rhythm*, vol. 4, no. 2, pp. 154–160, 2007.

[5] M. Haghjoo *et al.*, "Predictors of venous obstruction following pacemaker or implantable cardioverter-defibrillator implantation: a contrast venographic study on 100 patients admitted for generator change, lead revision, or device upgrade," *Europace*, vol. 9, pp. 328–332, 2007.

[6] R. G. Hauser *et al.*, "Risk factors for infection of implantable cardiac devices: data from a registry of 2496 patients," *Europace*, vol. 15, no. 1, pp. 66–70, 2012.

[7] S. Pakarinen *et al.*, "Short-term implantation-related complications of cardiac rhythm management device therapy: a retrospective single-centre 1-year survey," *Europace*, vol. 12, no. 1, pp. 103–108, 2009.

[8] N. Derval *et al.*, "Optimizing hemodynamics in heart failure patients by systematic screening of left ventricular pacing sites: The lateral left ventricular wall and the coronary sinus are rarely the best sites„" *J. Am. Coll. Cardiol.*, vol. 55, no. 6, pp. 566–575, 2010.

[9] L. Cammilli *et al.*, "Radio-frequency pacemaker with receiver coil implanted on the heart," *Ann. N. Y. Acad. Sci.*, vol. 111, pp. 1749–6632, 1964.

[10] W. D. Widmann *et al.*, "Radio-frequency cardiac pacemaker," *Ann. N. Y. Acad. Sci.*, vol. 111, pp. 992–1006, 1964.

[11] A. Auricchio *et al.*, "First-in-man implantation of leadless ultrasound-based cardiac stimulation pacing system: novel endocardial left ventricular resynchronization therapy in heart failure patients," *Europace*, vol. 15, no. 8, pp. 1191–1197, 2013.

[12] St. Jude Medical Inc., MN, USA.(2017, June 5). [Online]. Available: http://sjm.com/leadless-pacing.

[13] Medtronic Inc., MN, USA. (2017, June 5). [Online]. Available: http://medtronic.com/us-en/-micra.html

[14] Live Science. (2017, June 5). [Online]. Available: http://www.livescience.com

[15] A. Kiourti and K. Nikita, "A review of implantable patch antennas for biomedical telemetry: Challenges and solutions," *IEEE Antennas Propagat. Mag.*, vol. 54, no. 3, pp. 210–228, Jun. 2012.

[16] E. Chow *et al.*, "Implantable RF medical devices," *IEEE Microwave*, vol. 14, no. 4, pp. 64–73, Jun. 2013.

[17] M. Hannan *et al.*, "Energy harvesting for the implantable biomedical devices: issues and challenges," *BioMed Eng Online*, vol. 13, no. 79, pp. 1–23, Jun. 2014.

[18] J. Kim and Y. Rahmat-Samii, "Implanted antennas inside a human body: simulations, designs, and characterizations," *IEEE Trans. Microw. Theory Techn.*, vol. 52, no. 8, pp. 1934–1943, Aug. 2004.

[19] P. Soontornpipit *et al.*, "Design of implantable microstrip antenna for communication with medical implants," *IEEE Trans. Microw. Theory Techn.*, vol. 52, no. 8, pp. 1944–1951, Aug. 2004.

[20] A. Kiourti and K. S. Nikita, "Implantable antennas: A tutorial on design, fabrication, and in vitro/in vivo testing," *IEEE Microwave*, vol. 15, no. 4, pp. 77–91, Jun. 2014.

[21] C. Furse, "Designing of an antenna for pacemaker communication," *Microwaves RF*, vol. 39, no. 3, pp. 73–76, Mar. 2000.

[22] J. Schuster and R. Luebbers, "An FDTD algorithm for transient propagation in biological tissue with a cole-cole dispersion relation," *IEEE Int. Symp. Antennas Propagat.*, Atlanta, GA, USA, 21-26 June, 1998.

[23] S. Soora *et al.*, "A comparison of two and three dimensional dipole antennas for an implantable retinal prosthesis," *IEEE Trans. Antennas Propag.*, vol. 56, no. 3, pp. 622–629, Mar. 2008.

[24] K. Takahata *et al.*, "Micromachined antenna stents and cuffs for monitoring intraluminal pressure and flow," *J. Microelectromech. Syst*, vol. 15, no. 5, pp. 1289–1298, Oct. 2006.

[25] E. Chow *et al.*, "Evaluation of cardiovascular stents as antennas for implantable wireless applications," *IEEE Trans. Microw. Theory Techn.*, vol. 57, no. 10, pp. 2523–2532, Oct. 2009.

[26] N. Cho *et al.*, "A planar mics band antenna combined with a body channel communication electrode for body sensor network," *IEEE Trans. Microw. Theory Techn.*, vol. 57, no. 10, pp. 2515–2522, Oct. 2009.

[27] C. Liu *et al.*, "Compact dual-band antenna for implantable devices," *IEEE Antennas Wireless Propag. Lett.*, vol. 11, pp. 1508–1511, 2012.

[28] C.-M. Lee *et al.*, "Dual-resonant pi-shape with double l-strips pifa for implantable biotelemetry," *Electron Lett.*, vol. 44, pp. 1508–1511, Jul. 2008.

[29] T. Yilmaz *et al.*, "Characterization and testing of a skin mimicking material for implantable antennas operating at ism band (2.4 GHz-2.48 GHz)," *IEEE Antennas Wireless Propag. Lett.*, vol. 7, pp. 418–420, 2008.

[30] W. Xia *et al.*, "Performances of an implanted cavity slot antenna embedded in the human arm," *IEEE Trans. Antennas Propag.*, vol. 57, no. 4, pp. 894–899, Apr. 2009.

[31] P. Izdebski *et al.*, "Conformal ingestible capsule antenna: A novel chandelier meandered design," *IEEE Trans. Antennas Propag.*, vol. 57, no. 4, pp. 900–909, Apr. 2009.

[32] E. Falkenstein *et al.*, "Low-power wireless power delivery," *IEEE Trans. Microw. Theory Techn.*, vol. 60, no. 7, pp. 2277–2286, Jul. 2012.

[33] M. Theodoridis and S. Mollov, "Distant energy transfer for artificial human implants," *IEEE Trans. Biomed. Eng.*, vol. 52, no. 11, pp. 1931–1938, Nov. 2005.

[34] M. Catrysse *et al.*, "An inductive power system with integrated bi-directional data-transmission," *Sens. Actuators A: Phys.*, vol. 115, no. 2-3, pp. 221–229, 2004.

[35] U.-M. Jow and M. Ghovanloo, "Design and optimization of printed spiral coils for efficient transcutaneous inductive power transmission," *IEEE Trans. Biomed. Circuits Syst.*, vol. 1, no. 3, pp. 193–202, Sept. 2007.

[36] L.-J. Xu *et al.*, "Miniaturized circularly polarized loop antenna for biomedical applications," *IEEE Trans. Antennas Propag.*, vol. 63, no. 3, pp. 922–930, Mar. 2015.

[37] Z. Harouni *et al.*, "A dual circularly polarized 2.45-ghz rectenna for wireless power transmission," *IEEE Antennas Wireless Propag. Lett.*, vol. 10, pp. 306–309, 2011.

[38] M. Ali *et al.*, "A new circularly polarized rectenna for wireless power transmission and data communication," *IEEE Antennas Wireless Propag. Lett.*, vol. 4, pp. 205–208, 2005.

[39] H. Sun *et al.*, "Design of a high-efficiency 2.45-ghz rectenna for low-input-power energy harvesting," *IEEE Antennas Wireless Propag. Lett.*, vol. 11, pp. 929–932, 2012.

[40] J. Akkermans *et al.*, "Analytical models for low-power rectenna design," *IEEE Antennas Wireless Propag. Lett.*, vol. 4, pp. 187–190, 2005.

[41] A. G. Vera *et al.*, "Design of a 2.45 GHz rectenna for electromagnetic (em) energy scavenging," in *IEEE Symp. Radio and Wireless*, New Orleans, LA, USA, Jan. 2010, pp. 61–64.

[42] L. Marnat *et al.*, "On-chip implantable antennas for wireless power and data transfer in a Glaucoma-Monitoring SoC," *IEEE Antennas Wireless Propag. Lett.*, vol. 11, pp. 1671–1674, 2012.

[43] F.-J. Huang *et al.*, "Rectenna application of miniaturized implantable antenna design for triple-band biotelemetry communication," *IEEE Trans. Antennas Propag.*, vol. 59, no. 7, pp. 2646–2653, Jul. 2011.

[44] S. Hu *et al.*, "A low-cost 2.45-GHz wireless power link for biomedical devices," in *IEEE Asia-Pacific Conf. Antennas Propag.*, Singapore, 27-29 Aug., 2012.

[45] A. Poon *et al.*, "Optimal frequency for wireless power transmission into dispersive tissue," *IEEE Trans. Antennas Propag.*, vol. 58, no. 5, pp. 1739–1750, May. 2010.

[46] C. Liu *et al.*, "Design and safety considerations of an implantable rectenna for far-field wireless power transfer," *IEEE Trans. Antennas Propag.*, vol. 62, no. 11, pp. 5798–5806, Nov. 2014.

[47] S. Yang and J. Kim, "Wireless power transmission using dipole rectennas made on flexible cellulose membrane," *IET Microw. Antenna P.*, vol. 6, no. 7, pp. 756–760, May. 2012.

[48] H. M. K. *et al.*, "A miniature energy harvesting rectenna for operating a head-mountable deep brain stimulation device," *IEEE Access*, vol. 3, pp. 223–234, Jan. 2015.

[49] E. Y. Chow *et al.*, "Fully wireless implantable cardiovascular pressure monitor integrated with a medical stent," *IEEE Trans. Biomed. Eng.*, vol. 57, no. 6, pp. 1487–1496, Jun. 2010.

[50] InnerBody. (2015, June 5). [Online]. Available: http://www.innerbody.com.

[51] T. Dissanayake *et al.*, "Dielectric loaded impedance matching for wideband implanted antennas," *IEEE Trans. Microw. Theory Techn.*, vol. 57, no. 10, pp. 2480–2487, Oct. 2009.

[52] F. Merli *et al.*, "The effect of insulating layers on the performance of implanted antennas," *IEEE Trans. Antennas Propag.*, vol. 59, no. 1, pp. 21–31, Jan. 2011.

[53] P. S. Hall and Y. Hao, *Antennas and Propagation for Body-Centric Wireless Communications.* Artech House, 2012, pp. 63–107.

[54] S. Best and J. Morrow, "On the significance of current vector alignment in establishing the resonant frequency of small space-filling wire antennas," *IEEE Antennas Wireless Propag. Lett.*, vol. 2, no. 1, pp. 201–204, 2003.

[55] W. Scanlon *et al.*, "Radiowave propagation from a tissue-implanted source at 418 MHz and 916.5 MHz," *IEEE Trans. Biomed. Eng.*, vol. 47, no. 4, pp. 527–534, Apr. 2000.

[56] K. Ito, "Human body phantoms for evaluation of wearable and implantable antennas," *The 2nd Europ. Conf. Antennas and Propag.*, pp. 1–6, Edinburgh, UK, November 2007.

[57] K. Ito *et al.*, "Development and characteristics of a biological tissue-equivalent phantom for microwaves," *Electon. Commun. Jpn*, vol. 84, no. 4, pp. 1–6, 2001.

[58] T. Karacolak *et al.*, "Design of a dual-band implantable antenna and development of skin mimicking gels for continuous glucose monitoring," *IEEE Trans. Microw. Theory Techn.*, vol. 56, no. 4, pp. 1001–1008, April 2008.

[59] Y. Okano *et al.*, "The SAR evaluation method by a combination of thermographic experiments and biological tissue-equivalent phantoms," *IEEE Trans. Microw. Theory Techn*, vol. 48, no. 11, pp. 2094–2103, Nov. 2000.

[60] *ETSI Standard, Electromagnetic Compatibility and Radio Spectrum Matters (ERM); Ultra Low Power Active Medical Implants (ULP-AMI) Operating in the 401 MHz to 402 MHz and 405 MHz to 406 MHz Bands; System Reference Document*, vol. V1.1.1, no. TR 102 343, 2004.

[61] C. Gabriel, *Compilation of the Dielectric Properties of Body Tissues at RF and Microwave Frequencies.* Brooks Air Force, TX, USA.: Tech. Rep. Report N.AL/OE-TR-. 31-CB, 1996.

[62] C. Gabriel *et al.*, "The dielectric properties of biological tissues," *Phys. Med. Biol.*, vol. 41, no. TR 102 343, pp. 2231–2293, 1996.

[63] F. Merli *et al.*, "Design, realization and measurements of a miniature antenna for implantable wireless communication systems," *IEEE Trans. Antennas Propag.*, vol. 59, no. 10, pp. 3544–3555, Oct. 2011.

[64] J. D. Baena *et al.*, "Equivalent-circuit models for split-ring resonators and complementary split-ring resonators coupled to planar transmission lines," *IEEE Trans. Microw. Theory Techn.*, vol. 53, no. 4, pp. 1451–1461, April 2005.

[65] S. Raghavan and V. Rajeshkumar, "An overview of metamaterials in biomedical applications," *PIERS Proc.*, pp. 368–371, Mar. 2013.

[66] M.-C. Tang and R. Ziolkowski, "A study of low-profile, broadside radiation, efficient, electrically small antennas based on complementary split ring resonators," *IEEE Trans. Antennas Propag.*, vol. 61, no. 9, pp. 4419–4430, Sept. 2013.

[67] L. Desclos *et al.*, "Patch antenna size reduction by combining inductive loading and short-points technique," *Microw Opt. Technol. Lett.*, vol. 30, no. 6, pp. 385–386, Feb. 2001.

[68] K. Rajab *et al.*, "Size reduction of microstrip patch antennas with left-handed transmission line loading," *IET Microw. Antenna P.*, vol. 1, no. 1, pp. 39–44, Feb. 2007.

[69] Y. Dong *et al.*, "Design and characterization of miniaturized patch antennas loaded with complementary split-ring resonators," *IEEE Trans. Antennas Propag.*, vol. 60, no. 2, pp. 772–785, Feb. 2012.

[70] S. Gupta and G. Mumcu, "Circularly polarised printed antenna miniaturised using complementary split-ring resonators and reactive pin loading," *IET Microw. Antenna P.*, vol. 9, no. 2, pp. 118–124, 2015.

[71] X. Cheng *et al.*, "A compact omnidirectional self-packaged patch antenna with complementary split-ring resonator loading for wireless endoscope applications," *IEEE Antennas Wireless Propag. Lett.*, vol. 10, pp. 1532–1535, 2011.

[72] L. Kneisz *et al.*, "The short-term effects of antenna insulation thickness on path losses in wireless telemetry implants at microwave frequencies," *Eur. J. transl. Myol.*, vol. 23, pp. 91–94, 2013.

[73] S. H. Ward, Ed., *The ARRL Handbook for Radio Communications*. ARRL, 2010.

[74] U. Olgun *et al.*, "Low-profile planar rectenna for batteryless RFID sensors," in *IEEE Intl. Symp. Antennas Propag.*, Toronto, ON, Canada, Jul. 2010, pp. 1–4.

[75] Microschip Technology.(2015, June 5). [Online]. Available: http://www.microschip.com

[76] C. K. W. *et al.*, *Veterinary Anaesthesia*. Saunders Elsevier, 2014, ch. Section2: Anaesthesia of the species, pp. 345–384.

[77] E. Monnet and J. Chachques, "Animal models of heart failure: What is new?," *Ann. Thorac. Surg.*, vol. 79, pp. 1445–1453, 2004.

[78] *IEEE Standard for Safety Levels with Respect to Human Exposure to Radio Frequency Electromagnetic Fields, 3 kHz to 300 GHz*, IEEE standard C95.1-2005.

[79] W. L. Stutzman and G. A. Thiele, *Antenna Theory and Design*. 3rd Edition, New York: Wiley, 2012, pp. 100–127.

5. SIMULATION, OPTIMIZATION, AND VALIDATION OF A WIDE-BAND NUMERICAL MODEL AND ITS APPLICATIONS IN DEEPLY IMPLANTABLE ANTENNAS FOR LEADLESS PACING

5.1. Abstract

Goal: The study presented in this chapter[1] is aimed to design, develop, and validate a wide-band numerical model and demonstrate its application in deeply implantable antennas for leadless pacing. *Methods*: A wide-band tissue simulating liquid (TSL) was acquired from SPEAG and characterized by measuring its frequency dependent properties. The design, development and numerical characterization of the TSL was performed using a novel hybrid simulation method in High Frequency Structure Simulator (HFSS). The proposed numerical model was validated using a reference microstrip patch antenna. Also, the application of this model as well as the TSL was demonstrated by the design, development, manufacture and measurement of a novel metamaterial based deeply implantable conformal antenna at 2.4 GHz. *Results*: The measured properties of the TSL agreed well with the data sheet. Also, the results of reference antenna simulated in the numerical model were in good agreement with both experimental and analytical results. This validated the numerical model developed for the deeply implantable antennas. Moreover, the matching performance of the conformal antenna also showed good agreement between its simulated and measured results. *Conclusion*: It is evident from the results that the proposed numerical model can be used to design deeply implantable antennas for any frequency, ranging from 800 MHz to 5800 MHz. Furthermore, the proposed conformal antenna presents a great potential for future leadless pacing applications.

5.2. Introduction

Wireless powering and recharging of implantable cardiac devices such as pacemakers is not new [1–3], but is lately receiving significant attention [4–6]. Research in wireless power transfer

[1]The material presented in this chapter is under review and will be submitted for publication in a reputable journal in the field of biomedical engineering.

(WPT) for biomedical applications in particular is considered very important, because wireless power is almost a requirement for the implantable biomedical devices for the reasons of effectiveness, longevity and more importantly, safety.

For example, in conventional pacemakers, the transvenous leads and batteries are the biggest problems [7]. The leads can clog the vein and result in pneumothorax, tricuspid valve insufficiency and infection. Furthermore, the battery has lifetime issues and when depleted, it has to be replaced through a surgical procedure, which is both costly and painful for the patient. Moreover, every 14^{th} patient having a pacemaker device in the chest is likely develop an infection in the pacemaker pocket and among these cases, every 5^{th} may result in dealth [8].

To overcome these limitations and side effects of the conventional pacemakers, researchers have been investigating various modalities to achieve wireless or leadless pacing. Some of the common methods include inductive coupling, magnetic resonance, ultrasonic, radio frequency waves and even solar power [7, 9, 10]. Recent developments in the quest for a practical leadless pacemaker include the successful development of Micra TPS (Transcatheter Pacing System) and Nanostim by Medtronic [11] and St. Jude Medical [12], respectively. Unfortunately, such devices are impractical for multi-site pacing because they are single chamber and serves the needs of only 10-15% of the total heart failure patients. The need for a similar leadless pacemaker with multi-site pacing capability is critical to address the unmet clinical needs of heart failure patients needing cardiac resynchronization therapy (CRT) [13]. However, the development of such a device is challenging and remains an open problem.

In an effort to investigate a method with a possible solution to the aforementioned problem, a novel leadless pacemaker using implantable rectenna has been demonstrated in [4]. While the concept of energy harvesting deep inside the body, for leadless pacing, reported in [4] is novel, it is only a proof of concept and hence needs further developments, as well as improvements towards its practicality. The work described in this chapter is the advancement of the work described in [4] and is a step forward towards a practical leadless and multi-site pacing system. In particular, the contributions of this work are as follows:

1. Design, development and validation of a wide-band human body tissue simulation model for the development of deeply implantable antennas for leadless pacing applications.

2. Characterization and application of a wide-band human body tissue simulating liquid for the development and measurement of deeply implantable antennas.

3. Design, development, manufacturing and testing of a novel metamaterial based conformal and deeply implantable antenna for leadless pacing.

In this work, a full-wave 3D simulation tool, ANSYS High Frequency Structure Simulator (HFSS), was used to design, develop and validate a wide-band numerical model (WBNM). Employing a reference microstrip patch antenna, the numerical model was validated experimentally as well as analytically. It is mentioned that this numerical model was based on a human body tissue simulating liquid (TSL) acquired from SPEAG (Schmid & Partner Engineering AG, Switzerland) [14]. To the best of authors' knowledge, there is no similar wide-band numerical model for the design and optimization of deeply implantable antennas that is reported in the literature. The characterization of TSL was achieved by measuring its electrical properties using a dielectric probe. The application of this WBNM was also demonstrated by designing a novel compact conformal antenna at 2.45 GHz. Furthermore, the feasibility of the integration of these proposed antennas with a leadless pacemaker model, similar to Micra TPS [11] and Nanostim [12] has been demonstrated. Manufactured on a flexible 10 mil thick Roger's substrate, the implantable antenna prototypes was conformed on a 3D printed mock-up leadless pacemaker and measured in TSL. Results of the measurements agree well with the simulation. The compact and cylindrical design of manufactured prototype antenna and its integration with a miniaturized pacemaker model make this method feasible for leadless pacing applications.

The remaining of this chapter is organized as follows: In Section 5.3 related work on deeply implantable antennas proposed for wireless powering is discussed. Relevant details on work related to the dielectric properties and numerical modeling of human body as well as the challenges and limitations of the experimental human body phantoms are also presented in the same section. Section 5.4 is dedicated to the investigation of SPEAG's human body tissue simulating liquid and its characterization and results. In Section 5.5, the design, development and validation of a wide-band numerical tissue model is discussed by employing a reference microstrip patch antenna. Moreover, the application of the developed numerical model is demonstrated in Section 1.6, which includes the development, manufacturing and measurement of a metamaterial based deeply implantable

conformal antenna proposed for integration with a leadless pacemaker. Finally, Section 5.7 presents the discussion while the paper is concluded in Section 5.8.

5.3. Related Work

Every radio frequency (RF)-based implantable medical device (IMD) includes at least one implantable antenna, which is usually integrated with additional circuitry, the complexity of which depends upon the nature of the application of that IMD. Every part of a RF based IMD has its own importance and role in the overall functioning and application, however, the performance of the implantable antenna is critical without which the device may not even function. This highlights the importance of a correct modeling method for the design and development of an implantable antenna, which mainly includes (a) a human body tissue simulation model, and (b) measurements using an experimental human body phantom.

5.3.1. Deeply implantable antennas for wireless powering

There is a plethora of work reported on wearable and implantable antennas for biomedical telemetry related applications [15–18] but not much is available on deeply implantable antennas, especially for far-field wireless power transfer (WPT) applications. As mentioned in [19], one of the main obstacles for wireless powering of implantable devices is the attenuation of power density experienced by the propagation of the EM (electromagnetic) waves in a lossy human body. Furthermore, IEEE recommended limits for safe power density and SAR (specific absorption rate) have to be considered for safety, as reported in [19, 20].

Various antennas have been reported for WPT at shallow depths or subcutaneous applications [21–24]. However, it is mentioned that implantable antennas for WPT in deep tissue applications is very scarce in the literature. Some patents filed in the area of WPT for endoscopic capsules using magnetic coupling of coils are summarized in [25]. Furthermore, a midfield wireless powering method using coils was proposed for deep-tissue microimplants [26]. A wireless neural recording device using an implantable antenna at a depth of 12 mm inside a phantom has recently been reported in [27]. In [28], a RF-based wireless biomedical system with an on-chip antenna and CMOS diodes are proposed for Glaucoma intraocular and cardiovascular pressure monitoring. In [4], a far-field RF-based powering of a leadless pacemaker at 1.2 GHz has used a planar rectenna, which was implanted 5 cm deep inside an ovine model. Previous work has been progressive, however

this chapter presents new results on two miniaturized and conformal deeply implantable antennas for the WPT method similar to reported in [4].

5.3.2. Dielectric properties and numerical modeling of the human body

A summary of literature on the dielectric properties and various methods of modeling of human body tissues is described in [18, 29]. Implanted antennas are completely embedded inside the human body, which consists of time-varying lossy dielectric materials (including skin, fat and muscle etc.). It is hence critical that besides the modeling and optimization of the antennas, special consideration is given to the human body modeling in the available simulation tools. Some advanced 3D electromagnetic solvers for the design and development of implantable antennas and other RF based-biomedical devices and systems include, (1) ANSYS-High Frequency Structure Simulator (HFSS), which is based on the finite element method (FEM) [30]; (2) Computer Simulation Technology Microwave Studio (CST MWS), which is based on FDTD (Finite-Difference Time Domain) method [31]; and (3) ZWT-SPEAG's Sim4Life, which also uses FDTD method [32].

Based on the capabilities of CST and HFSS, researchers have been designing their own anatomical numerical models of human body tissues and have also employed digital human body phantoms readily available in these tools [33, 34]. It is noted that the selection of these tools has mostly been dependent upon the availability and personal preference rather than the performance, as both have similar characteristics. Nevertheless, the computational cost (processing power of the machine and the time etc.) is all dependent upon the model and structure of the antenna and also on the complexity of the tissue.

There are various ways in which these numerical simulations can be employed for the design of the implantable antennas. Anatomical human tissue models may provide better and more realistic results but the associated cost and the computational time is higher. Examples of some digital phantoms with high resolution of the human body in HFSS is shown in Fig. 5.1. Different geometries, uniform and nonuniform models can be designed with single or multilayer configurations, as presented in the examples illustrated in Fig. 5.2. In [34], it is shown that similar results can be achieved while using a multilayer canonical model as compared to a realistic human chest model. Also, the performance of another implantable patch antenna, designed in [35], shows similar agreement when results of using a three-layer spherical model were compared against the study repeated using an anatomical model of the human head.

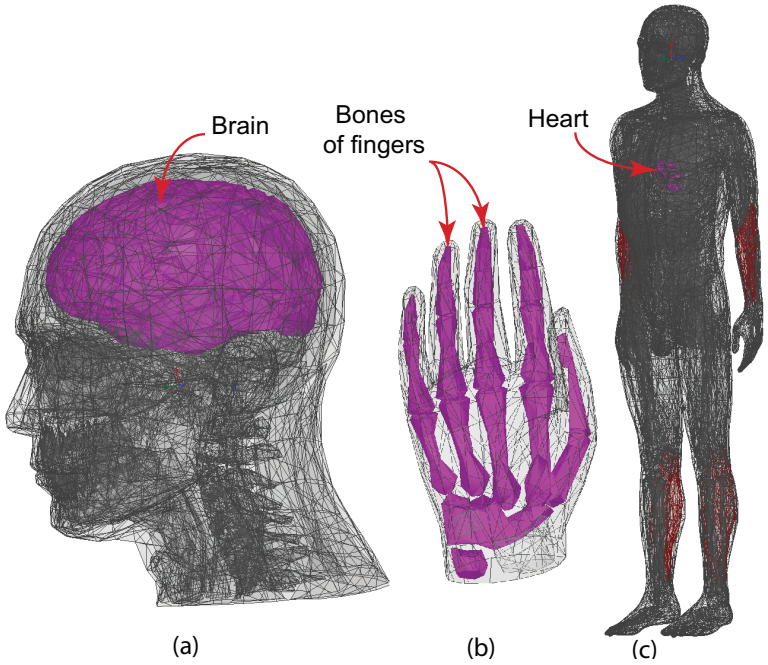

Figure 5.1. Different examples of digital human body phantoms with 2 mm resolution, available in ANSYS-HFSS [30]: (a) A human head (brain highlighted), (b) a human left hand (bones highlighted), and (b) a full human body phantom of 35 years old male (heart highlighted).

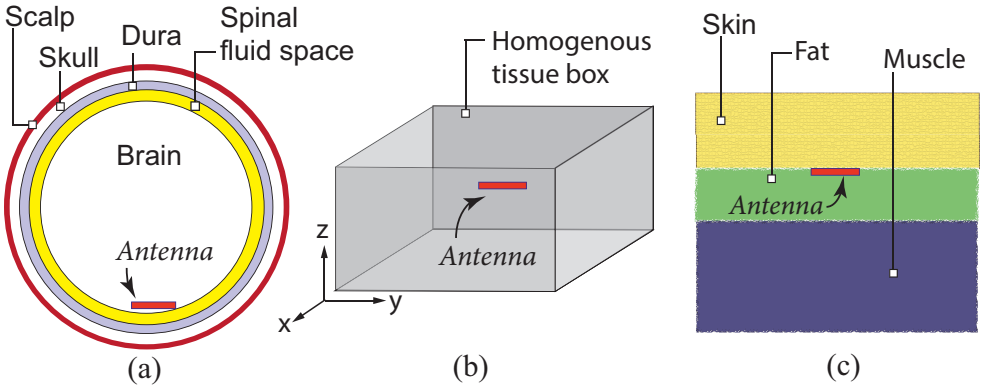

Figure 5.2. Various examples of phantom geometries (not drawn to the scale) used in numerical methods for the design and development of implantable antennas. (a) A spherical multi-layer head model, (b) a muscle equivalent phantom, and (c) a 3-layer model representing skin, fat and muscle of the human body.

The multilayer canonical models are proven to provide an acceptable model for the human body. When considering a detailed design modeling of the human body, each biological tissue is

assigned specific properties including the relative permittivity ε_r, conductivity σ and mass density ρ values. These frequency dependency of these properties (ε_r, σ) is taken into consideration by employing various algorithms based on the Cole-Cole models [36] or Debye models [37]. An extensive detail of the dielectric properties of the human body tissues at a range of radio frequency and microwave frequencies is available in literature [38], [39].

5.3.3. Challenges and limitations of experimental human body phantoms

Following the design, optimization and fabrication of an implantable antenna, accurate measurements of its performance parameters are very important. The implantable antenna's performance can be measured in various kinds of phantoms, which emulates the accurate dielectric properties of the human body. These phantoms provide a practical platform for testing of the implantable antennas and the process depends on the type of phantom being used. A fabricated prototype is either fully immersed, inserted or carefully placed inside the phantom and then results are taken using a calibrated network analyzer. To fully validate a model, it is recommended to create an identical scenario to the one used in the numerical tool and also consider the overall application.

The main challenge with these phantoms is the overall formulation. The final phantom should be free of any air bubbles and also during preparation, the mixture has to be carefully stirred while being heated and also, the ingredients have to be added at certain temperatures during the process. Furthermore, most of these phantoms are very narrow band and a little imperfection in the preparation process can be unfavorable.

The ingredients of the phantom recipes mainly include DI (Deionized) water, salt, sugar, gelatine, soap, and also oil. It is shown that increasing the sugar concentration decreases ε_r, while also contributes towards a slight decrease in σ. Also, adding more salt to the solution causes a significant increase in σ, while the ε_r decreases [36]. Overall, the available phantoms can be categorized into three types, i.e., liquid, semisolid, and solid phantoms [18].

5.3.3.1. Liquid phantoms

These types of phantoms have to be contained in a container, the properties of which have to be carefully selected as they can often influence the overall dielectric properties of the liquid phantom. These types of phantoms are relatively easy to prepare and can be contained in a variety of geometries similar to the anatomical parts, such as a limb or a torso. Unfortunately, the

available liquid phantoms reported in the literature covers frequencies up to 6 GHz only, as shown in [14]. Examples of different phantoms and tissue recipes are summarized in Table 5 in [35]. These phantoms can be manufactured for narrow- or wide-band frequencies, but a slight variation in their preparation method can present different results.

5.3.3.2. Semi-solid phantoms

These types of phantoms are also known as gel-phantoms and they do not need a container to hold its shape. These phantoms can be used to manufacture a layered heterogeneous phantom and are preferred for their long term stability and ease of use. In [40], a preparation method and characterization of different types of narrow-band and ultra-wide-band human tissues mimicking phantom has been proposed for a frequency range of 500 MHz to 20 GHz. Some other examples of semi-solid phantoms are proposed in [41–43].

5.3.3.3. Solid phantoms

As compared to the semi-solid phantoms, these types of phantoms have a longer shelf life but are only available up to frequencies of 6 GHz. They are very expensive to manufacture because their manufacturing process is complex and requires extremely high temperatures and pressures. Depending on the application, some methods to prepare these kind of phantoms are reported in [44–46].

5.4. SPEAG's Human Body Tissue Simulating Liquid

In order to design, develop and optimize a human body tissue simulating liquid (TSL) in a numerical tool, such as HFSS, a commercially available wide-band tissue simulating model (phantom), acquired from SPEAG (Schmid & Partner Engineering AG, Switzerland) [47] was selected in this work. The rationale behind this choice was to select a standard TSL, and also to minimize the limitations of the available phantoms, as mentioned in the previous section.

The category of simulating liquid acquired for this work was human body Tissue Simulating Liquid (TSL) and its product and batch numbers were 'SM AAM U16 BD' and '160218-1', respectively. The recommended frequency range for this specific TSL was from 800 MHz - 5800 MHz. It is worth mentioning that SPEAG's TSL is mainly used for SAR (specific absorption rate) measurements and that its use in the design and measurement of implantable antennas is not available in the literature. The application of TSL for implantable antennas presented in this paper is the first reported on a standard commercially available TSL.

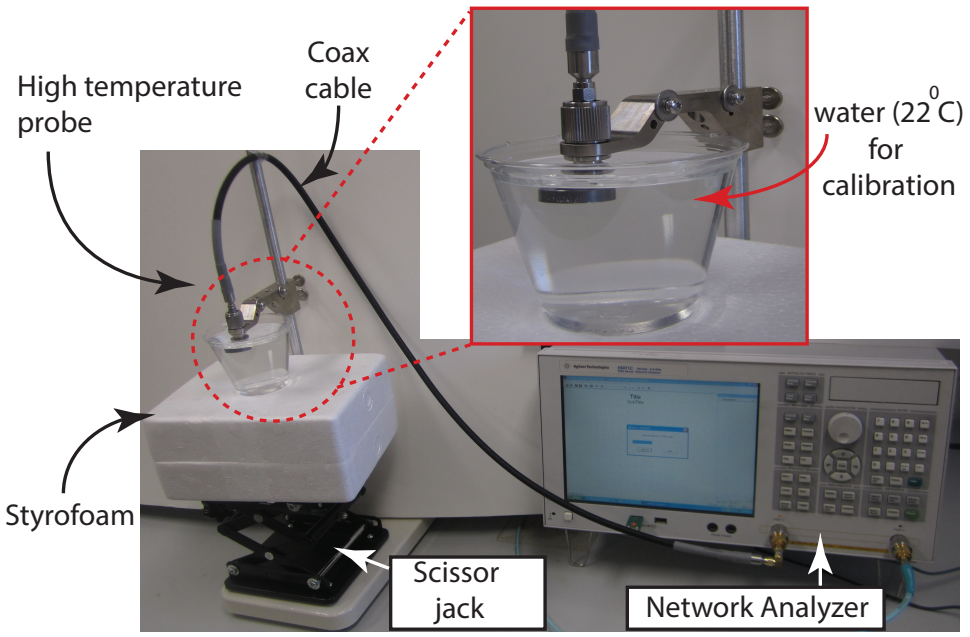

Figure 5.3. Picture of complete calibration setup of the Keysight N1501A - High Temperature Dielectric Probe Kit (inset shows the probe inserted in water at 22 °C).

5.4.1. Characterization of body tissue simulating liquid

SPEAG, the manufacturer of the body tissue simulating liquid (TSL), provided the dielectric properties of the given TSL, which were measured using a DAK 3.5 dielectric kit [48]. However, in an effort to fully characterize the acquired TSL and validate its properties given in the datasheet, a separate study was performed. The dielectric properties included relative permittivity-real ε_r', relative permittivity-complex ε_r'', conductivity σ and loss tangent $tan\,\delta$.

A Keysight N1501A Dielectric Probe Kit [49] was used to re-measure these properties at the Applied Electromagnetics Laboratory at North Dakota State University, Fargo, ND, USA. The N1500A materials measurement suite was first installed on a Keysight E5071C vector network analyzer (VNA) and then the high temperature probe was connected to the VNA using a coaxial cable to take the measurements. The calibration setup is shown in Fig. 5.3.

The actual measurement procedure is summarized as follows: (a) Select the range of frequencies and the type of sweep to be performed. (b) Calibrate the entire system by using three known standards, i.e., air, a short circuit and water. (c) Insert the probe into a sample of the BTSL

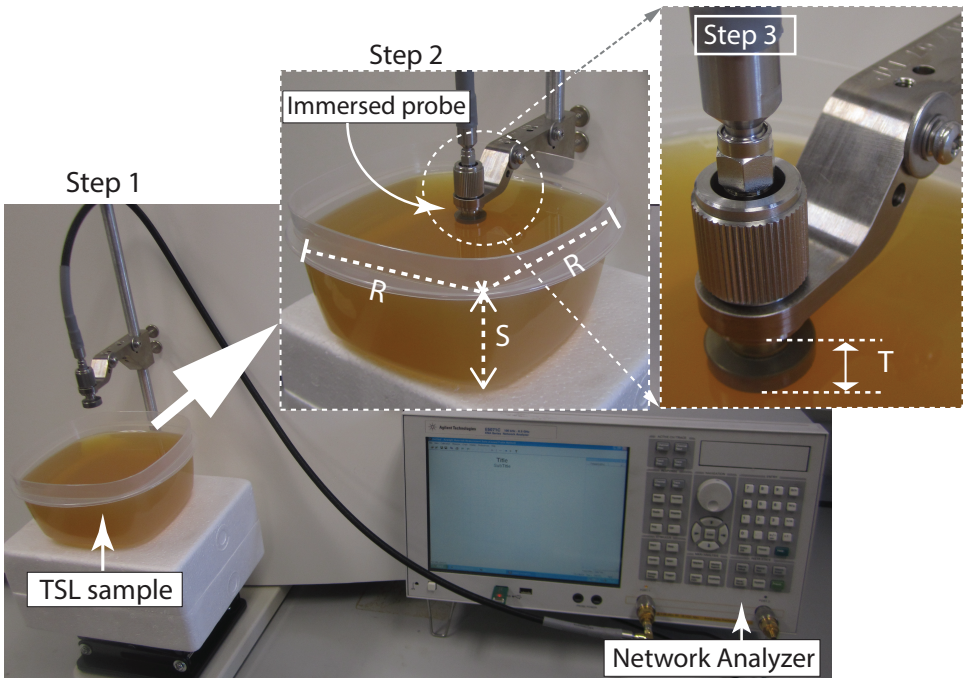

Figure 5.4. Experiment setup for measuring the dielectric properties of the SPEAG's human body tissue simulating liquid (TSL). Dimensions are (in cm): $R = 15$, $S = 6.5$ *and* $T = 1.2$.

and take the required measurements. Each property (ε_r, σ, etc.) is measured separately and one at a time.

Following the calibration procedure, the measurement setup, specifically the coaxial cable and the high temperature probe, should not be moved or else calibration may get affected. In this method, a metallic scissor jack was used to support the container (containing the sample of TSL) and provide stability to the measurement setup. To minimize the effect of the metallic scissor jack on the actual measurements, a 10 cm thick Styrofoam block ($\varepsilon_r = 1.03$) was inserted between the scissor jack and the measuring sample. The properties of the Speag's human body TSL were measured using the above stated method and the experiment setup is shown in Fig. 5.4. The quantities directly measured by the this probe were, (a) real part of the relative permittivity ε_r' (b) complex part of the relative permittivity ε_r'', (c) loss tangent $tan\,\delta$, and (d) Cole-Cole diagram. The conductivity (S/m) of the TSL was computed using the following expression:

$$\sigma = 2\pi f \varepsilon_r'' \varepsilon_o \quad (S/m), \tag{5.1}$$

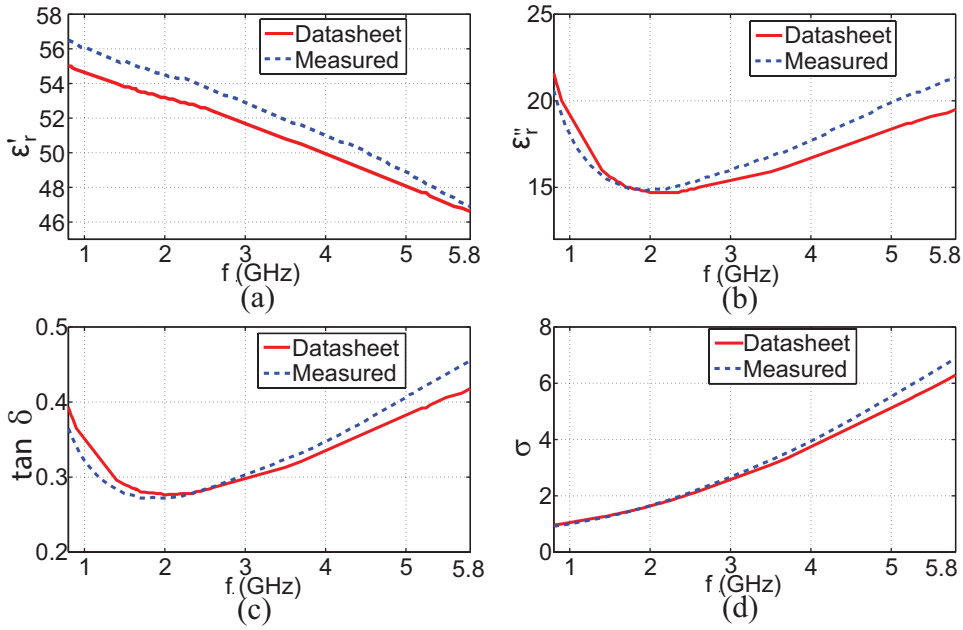

Figure 5.5. Comparison of the measured properties of SPEAG's TSL with the datasheet. (a) Real part of the relative permittivity ε_r', (b) complex part of the relative permittivity ε_r'', (c) loss tangent $tan\,\delta$, and (d) conductivity σ.

where f is the frequency in Hz, ε_r'' is the complex permittivity measured by the probe at a specific frequency f, and ε_o is the free space permittivity ($\varepsilon_o = 8.85412 \times 10^{-12} F/m$).

5.4.2. Comparison of measured dielectric properties with data sheet

Several measurements were performed to confirm the repeatability of the results within an acceptance margin. The measured dielectric properties of the TSL were compared with the values provided in the data sheet which showed a good agreement, as shown in Fig. 5.5. The agreement between the datasheet and measured values of the TSL properties confirmed the validity of the reported properties of the TSL. This further validated the SPEAG's TSL phantom suitability for implantable antenna measurements for a range of frequencies, i.e., 800 MHz to 5800 MHz.

5.5. Design, Development and Characterization of the Simulation Model

ANSYS-High Frequency Structure Simulator (HFSS), version 17.1, was used to design and develop the simulation model for the implantable antennas. A step-by-step procedure with a brief description of each process is presented in Fig. 5.6. With regards to the selection of the phantom type, an exact replica was created in HFSS, which matched the experimental setup designed and manufactured for the measurement of the implantable antenna prototype. This consisted of a

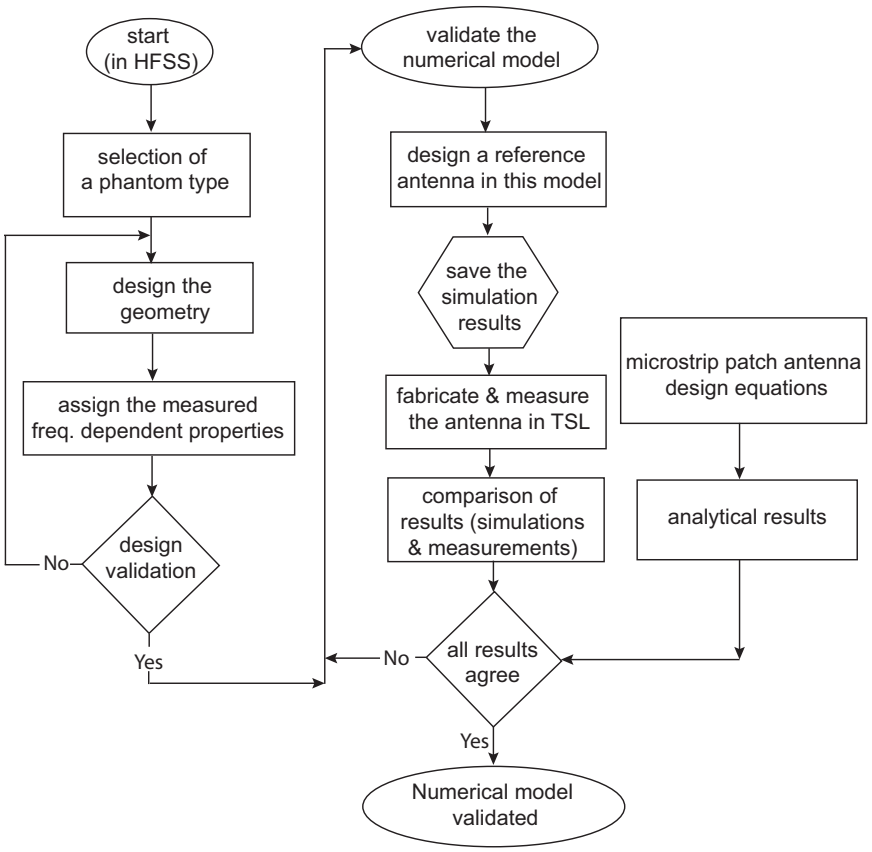

Figure 5.6. A flowchart showing important steps performed in the design, development and validation of the numerical model for deeply implantable antennas.

cubical Plexiglas container measuring approximately 30 cm on each side and filled with SPEAG's TSL (up to 8.0 cm $\approx$ 7.0 liters). The dielectric properties, relative permittivity ε_r and conductivity σ assigned to the Plexiglas container (in simulation) were 3.4 and 0, respectively. In addition, the measured frequency dependent properties (from 800 MHz - 5800 MHz) were assigned to the TSL model in HFSS. To satisfy the boundary conditions in simulation, this setup was enclosed in a radiation box, which was kept at a distance of $\lambda_o/4$ away from the structure (λ_o being the free space wavelength). A 3D sketch of this model, created in HFSS, is shown in Fig. 5.7.

5.5.1. Designing a reference microstrip patch antenna

In order to fully validate the simulation model developed for the implantable antennas, it was important to complete the characterization and testing of the proposed model using a reference antenna. Therefore a reference microstrip patch antenna was designed in HFSS for air. A patch

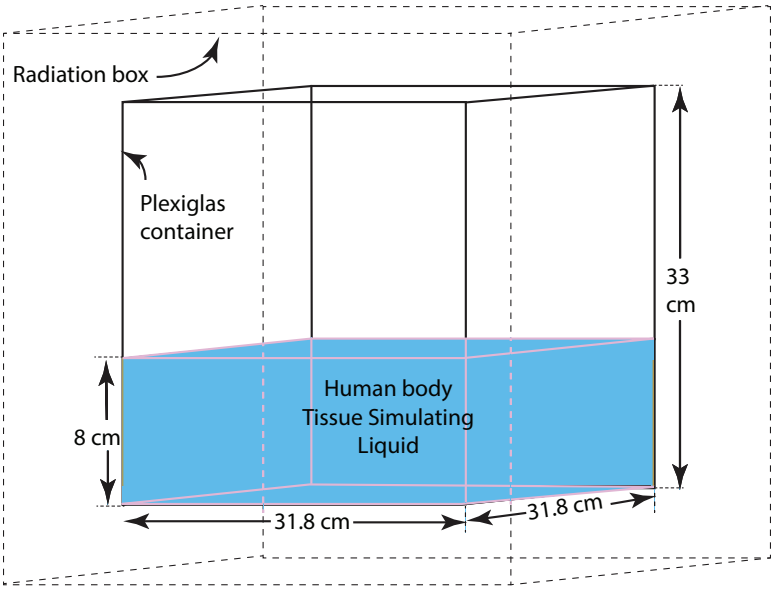

Figure 5.7. An illustration of the geometry (with complete dimensions) of the experimental setup of the tissue simulating model developed in HFSS.

antenna was selected because its a low profile antenna, easy and inexpensive to manufacture, and more importantly, can be validated using the equations given in [50]. Reviewing the range of the frequency dependent properties of the given TSL, 5.0 GHz was selected as the target resonant frequency for the design of this reference patch antenna (RPA). The aim was to design a microstrip RPA that would resonate at a higher frequency in air or free space, and then model and measure the same prototype in the TSL to observe a frequency shift. It was therefore envisioned that for the same reference antenna, when tested in SPEAG's human body TSL (being a lossy medium), a lower resonant frequency would be achieved.

5.5.2. Prototype fabrication and measurements in air

A patch antenna with an inset microstrip feed line (matched to 50 Ω) was designed, simulated and optimized using a 3D full wave electromagnetic solver, HFSS. This antenna was designed and fabricated on a 1.52 mm thick Rogers TMM4 substrate, having a relative permittivity ε_r of 4.5, loss tangent $tan\,\delta$ of 0.002, and copper lamination thickness of 17.5 μm. The antenna was manufactured in-house using a LPKF ProtoMat S63 milling machine, with a resolution (X/Y) of approximately 0.5 μm. A complete 3D model with details of the geometry and a picture of the antenna prototype are shown in Fig. 5.8 (a) and (b). Following the fabrication of the antenna, a 50 Ω

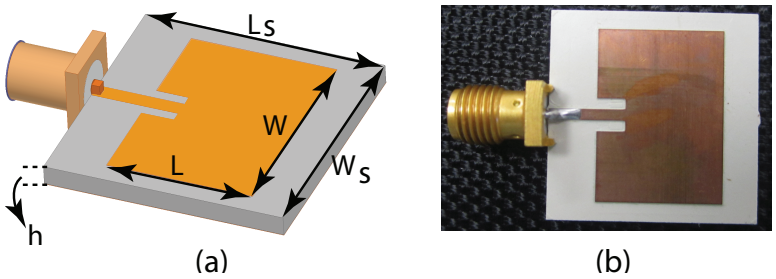

Figure 5.8. A 5.0 GHz reference microstrip patch antenna. (a) Design created in HFSS (Dimensions are as follows (all in mm): $L = 13.38$, $W = 18.24$, $L_s = W_s = 22$, $h = 1.52$), and (b) a picture of the manufactured prototype reference microstrip patch antenna.

SMA connector was soldered to its feed line and whole prototype antennas was insulated with a thin layer (approximately 0.01 μm) of conformal coating. The antenna was insulated because eventually it had to be tested in the TSL (which is conductive) and effects on the resonant frequency in both cases, air and the TSL were of interest.

The reflection coefficients ($|S_{11}|$ in dB) of the manufactured prototype antenna were measured in a calibrated anechoic chamber and results were compared with simulations. Fig. 5.9 (a) shows good agreement between the simulated and measured results. The simulated 3D radiation plot showing a total gain of 5.8 dB is shown in Fig. 5.9(b).

5.5.3. Simulation setup in HFSS

Following the successful design and measurement of the RPA in air, the same antenna (without any modification) was inserted as a 3D component into the TSL inside the Plexiglas container in the numerical model created in HFSS. Because of the larger electrical size of the setup and to save both the computational time and cost, an integral equation solver (Domain Decomposition) in a hybrid simulation type was employed for this complex case.

Specifically, the configuration of hybrid simulation was performed as follows: First, the RPA was enclosed in a small box, measuring $8\,mm \times 14\,mm \times 20\,mm$, and was assigned the measured frequency dependent properties of the TSL. The walls of this box were kept $\lambda_{TSL}/10$ away from each corner of the antenna model. This small box was then subtracted from the TSL (filled in the Plexiglas), with a clone object tool selected. The TSL outside the small box was then defined as a dielectric cavity.

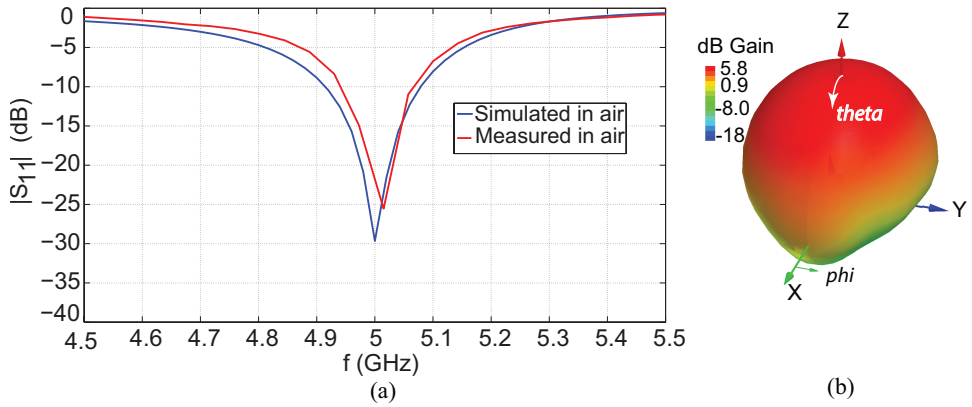

Figure 5.9. Performance of the reference microstrip patch antenna. (a) Comparison of the simulated and measured reflection coefficients ($|S_{11}|$ in dB), and (b) a simulated 3D radiation plot showing total gain (in dB).

This process essentially divided the whole TSL into two regions, one with the antenna enclosed in a smaller box and the second with the TSL outside the small box. The main reason for this segregation was to enable HFSS to solve the antenna including the smaller box with finite element method and the remaining geometry (including the TSL) with method of moment. The model used in HFSS is illustrated in Fig. 5.10. All the simulations were performed under a high performance computing (HPC) license on a powerful machine, having two processors (Intel Xeon(R) CPU E5-2699 v3 2.30 GHz) with 16 cores each and 192 GB of dedicated RAM.

5.5.4. Comparison and validation of the results in tissue simulation liquid

Results obtained from the HFSS simulations were then compared with the measurements performed in the TSL. As shown in Fig. 5.11, results agreed well with each other and as expected, the resonant frequency of the RPA got shifted from 5.0 GHz, in air, to a lower resonance, i.e., 1.5 GHz when inserted in TSL. This was further validated using the equations given in [51].

The wavelength in air for the given case is computed as,

$$\lambda_{air} = \frac{c}{f\sqrt{\epsilon_r}}. \tag{5.2}$$

Then by using the given values, the wavelength in air is,

$$\lambda_{air} = 28.28\ mm. \tag{5.3}$$

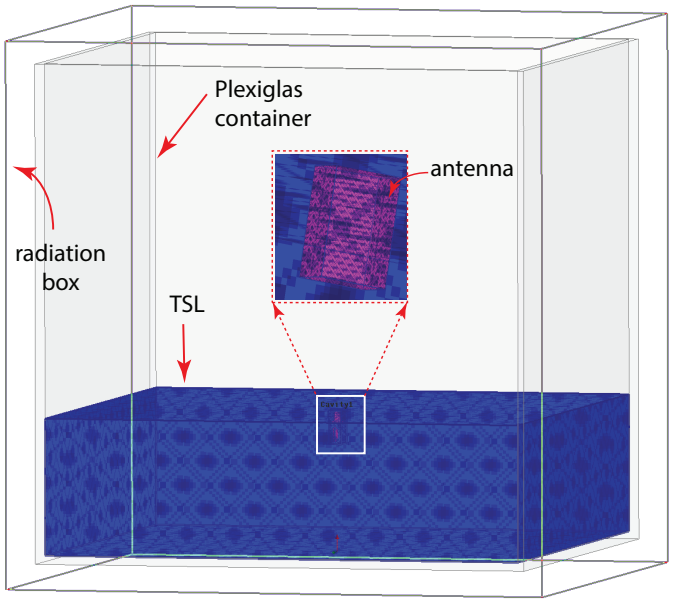

Figure 5.10. Simulation model of the antenna, TSL material and Plexiglas container in HFSS.

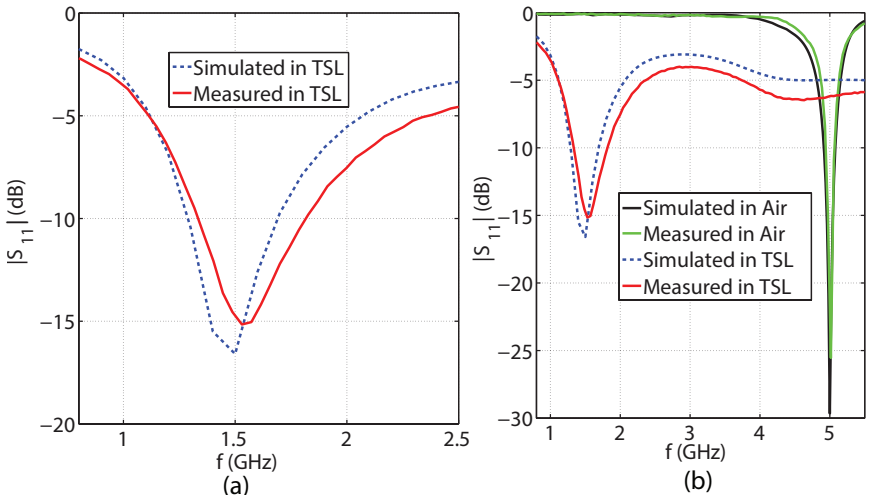

Figure 5.11. Comparison of the simulated and measured results. (a) Comparison of measured and simulated $|S_{11}|$ (in dB) in TSL, (b) Comparison of the results taken in air and in TSL, showing a resonance shift.

The actual radiating length (L) of the RPA is $13.38\,mm$, hence the electrical length of the RPA w.r.t. the wavelength can be computed as,

$$L = L_{air} = 0.473\,\lambda_{air} \approx 0.5\,\lambda_{air}. \tag{5.4}$$

Similarly, the above steps are repeated for the RPA when radiating in the TSL. It is observed the resonant frequency of the RPA in TSL is 1.56 GHz, and the measured relative permittivity ϵ_r of the TSL at 1.56 GHz is 55.2. The wavelength of the RPA in TSL is hence given by,

$$\lambda_{TSL} = \frac{c}{f\sqrt{\epsilon_{rTSL}}}. \tag{5.5}$$

Then by using the given values, the wavelength in the TSL is,

$$\lambda_{TSL} = 25.88\,mm. \tag{5.6}$$

The actual radiating length (L) of the RPA is $13.38\,mm$, hence the electrical length of the RPA w.r.t. the wavelength in TSL can be computed as;

$$L = L_{TSL} = 0.51\,\lambda_{TSL} \approx 0.50\,\lambda_{TSL}. \tag{5.7}$$

This implies that,

$$L = L_{air} = L_{TSL} = 0.50\,\lambda_{air} = 0.50\,\lambda_{TSL}. \tag{5.8}$$

It is hence shown that the resonant frequency of this RPA is the function of its length, which is consistent both in air, and also in the tissue simulating liquid. Moreover, for the given relative permittivity ϵ_r of 4.5 and resonant frequency of 5.0 GHz, the length L and width W of the RPA computed using the microstrip patch antenna equations [51] resulted in the dimensions of $13.64\,mm$ and $18.08\,mm$, respectively. Compared to the measured values (L & W) of $13.38\,mm$ and $18.24\,mm$, the percentage error was found to be 1.9 and 0.9 %, respectively. This further validates the accuracy of the simulation model created in HFSS for the design and optimization of the implantable antennas.

5.6. Applications of the Developed Simulation Model

The developed simulation model was employed to design a deeply implantable conformal metamaterial-based antenna for leadless pacing applications.

5.6.1. Design concept of a novel leadless pacemaker

As mentioned in Section 5.2, the main goal of developing a wide-band numerical model was to provide a platform for the design and development of deeply implantable antennas, especially for leadless pacing. To further the work reported in [4], and to devise a more practical leadless system, a novel metamaterial-based conformal implantable antenna for integration with a pacemaker design similar to Nanostim [12] is proposed. The design concept of this system is illustrated in Fig. 5.12(a)-(d).

Following the RF energy harvesting concept from [4], it is envisioned that the integration of a conformal implantable antenna with the casing of a device similar to Nanostim, as shown in Fig. 5.12 (b), will be a more practical and realizable solution for leadless pacing. The antenna will receive the power from the incoming RF wave (transmitted from outside to inside the body) and then provide this power to the circuitry enclosed inside the cylinder (device) for energy harvesting

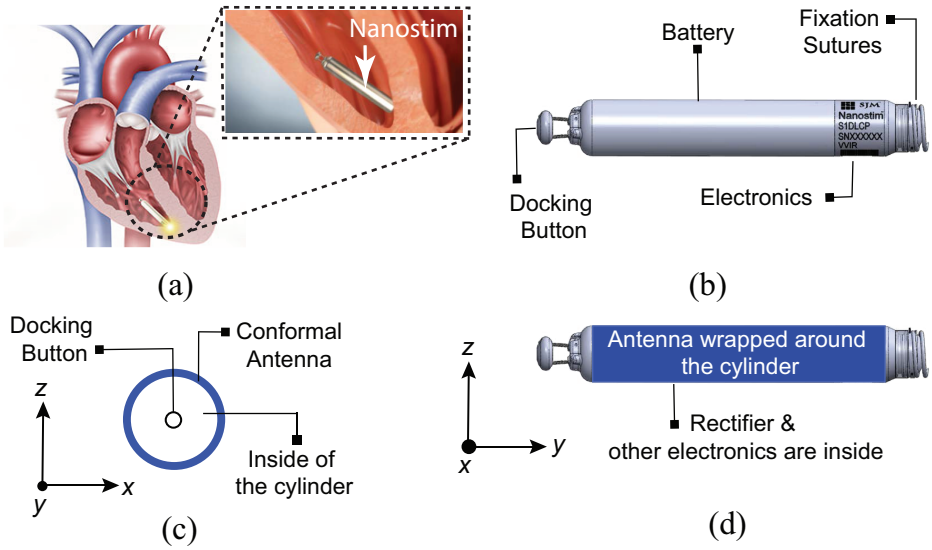

Figure 5.12. (a) St. Jude's Nanostim leadless pacemaker (NLP) positioned in the right ventricle (RV). (b) Details of the various components of the NLP. (c) & (d) Proposed modifications to the NLP showing two different orientations of the conformal antenna wrapped around the circumference of the NLP.

and eventually pacing the myocardium. With no battery requirements, this proposed leadless pacemaker model can be a good candidate for miniaturization.

5.6.2. A complimentary split-ring resonator (CSRR)−loaded deeply implantable conformal antenna

To achieve a novel miniaturized and conformal deeply implantable antenna for leadless pacing, a resonant type metamaterial technique, i.e., a complimentary split-ring resonator (CSRR) [52] has been used in this work. This technique provided the flexibility to achieve the required resonance frequency, and also helped in achieving a compact design with relatively good performance. The resonance frequency for this antenna was decided to be 2.45 GHz, which is an available open band in the industrial, scientific and medical (ISM) radio bands.

The proposed numerical model, developed in Section 5.6, was employed for the design and development of this conformal and deeply implantable antenna. A $10\,mil$ thick Rogers 6010LM substrate, having a dielectric constant ϵ_r of 10.2 was selected for this application. This substrate was selected due to its flexibility and high dielectric constant, which helped in achieving a conformal and compact design. A dummy cylindrical pacemaker measuring $20\,mm$ in length and $6\,mm$ in diameter was first created in HFSS and the implantable antenna was conformed around this cylinder. With $17.5\,\mu m$ of copper thickness on each side of the substrate, the overall thickness of the antenna was $0.289\,mm$. When the antenna was wrapped around the circumference of the cylinder, the total diameter of this model increased to $6.578\,mm$. A detailed geometry with dimensions of the implantable antenna and the pacemaker is shown in Fig. 5.13 (a-c).

The dummy cylindrical shaped pacemaker was designed in Solidworks, and manufactured using a desktop 3D printer (MakerBot Replicator). Also, the antenna was fabricated using the LPKF S63 Protomat milling machine and then tightly wrapped around the 3D printed pacemaker model. A $50\,\Omega$ SMA connector was connected to the conformal antenna prototype for testing purposes, as shown in Fig. 5.13(d). The manufactured prototype was conformal coated for insulation purposes before immersing it, 5 cm deep, inside the tissue simulating liquid for performance measurements. This measurement setup, showing a Keysight E5071 network analyzer and a Plexiglas container filled with TSL is shown in Fig. 5.14. A comparison of simulated and measured matching performance has shown a good agreement, as shown in Fig. 5.15. Although the measurements were performed in a fully calibrated anechoic chamber, a small frequency shift in the measure-

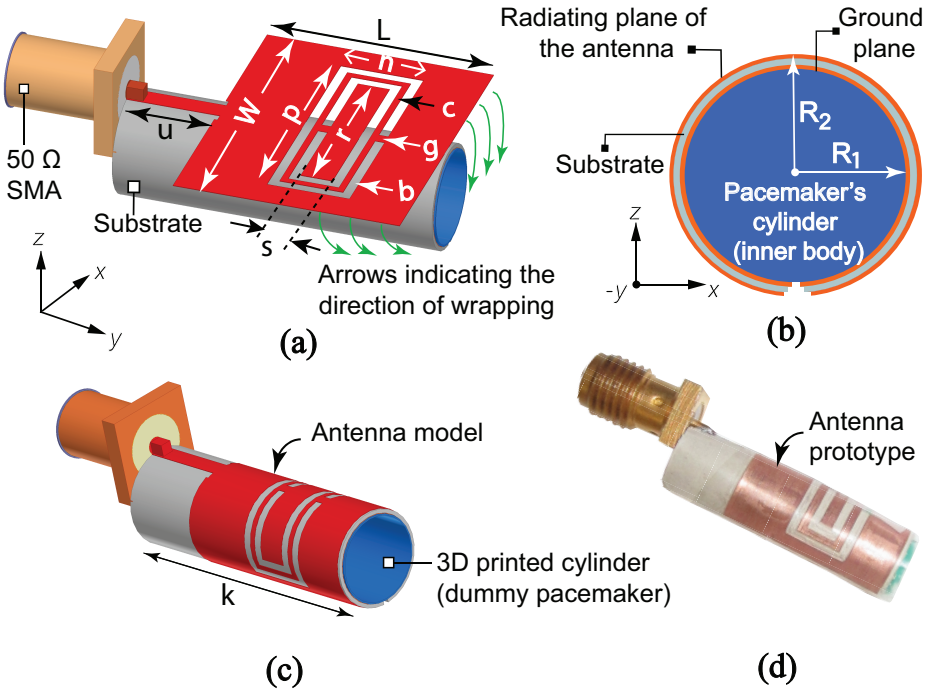

Figure 5.13. (a) The geometry details of the CSRR unit cell. (b) A different orientation of the model of the proposed antenna with leadless pacemaker (dummy). (c) A complete 3D model of the antenna with SMA connector. (d) A picture of the manufactured prototype. Dimensions are (in mm): $u = 5.7$, $L = 14.28$, $W = 17.28$, $p = 14$, $r = 10.8$, $g = 0.75$, $s = 2$, $n = 5.2$), $k = 20$, $d = 6.5$, $c = 0.4$, $b = 0.6$, $R_1 = 3$, $R_2 = 3.28$.

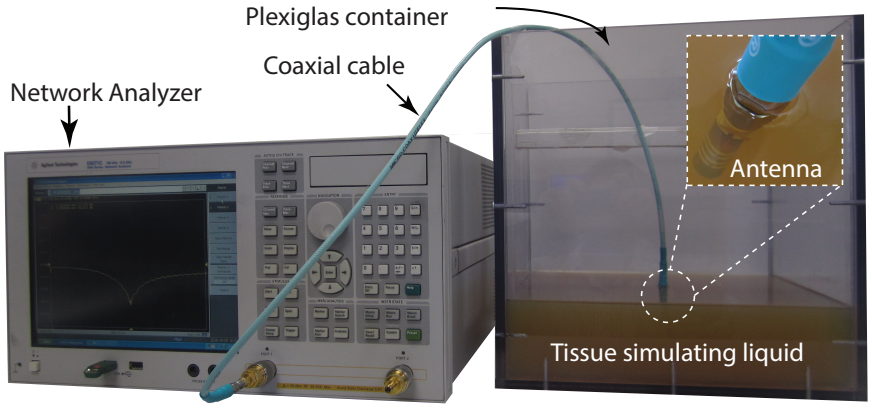

Figure 5.14. A picture of the experiment setup showing CSRR-loaded conformal antenna being measured in the TSL.

ments was observed, which was attributed to the fabrication and manufacturing imperfections of the prototype.

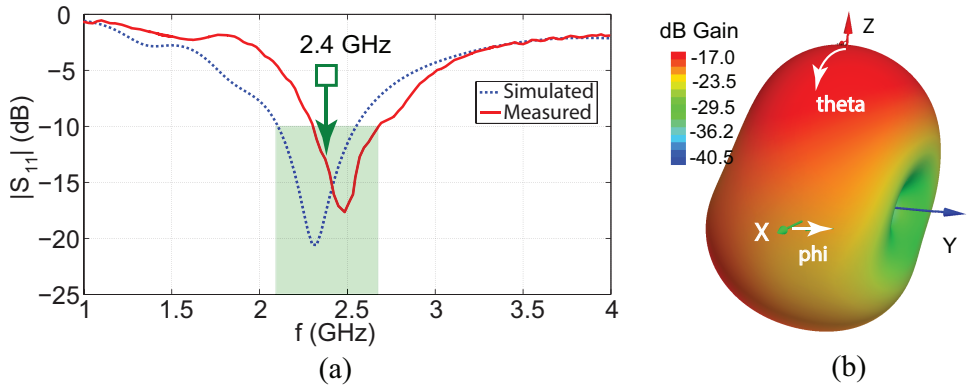

Figure 5.15. Performance of the CSRR loaded conformal antenna. (a) Comparison of the simulated and measured reflection coefficients ($|S_{11}|$ in dB). (b) A 3D radiation pattern showing the total gain in dB.

5.7. Discussion

The main emphasis of the work presented in this chapter is on the development and validation of a numerical model for deeply implantable antennas for leadless pacing. However, this platform can certainly be used for other biomedical applications involving the design of deeply implantable antennas. Following the validation of the numerical model, a conformal antenna integrated with a dummy pacemaker was proposed. The design concept of the proposed system was adapted from Nanostim and was favored due to its less invasive delivery method using femoral artery. It is important to note that the overall size of our proposed leadless pacemaker, with the conformal antenna included, is smaller than Nanostim, i.e, a total volume of $0.68\,cm^3$ compared to $1\,cm^3$. It is envisioned that once fully developed, this leadless pacemaker will be delivered using a sheath and in the same manner as Nanostim or Micra TPS. It should be mentioned that a complete RF-energy based leadless pacemaker will also need a wearable transmitting system, with flexible wearable antennas for transmitting the RF energy into the body. The development of such a wearable system will be critical to achieve the overall objective but is beyond the scope of this work.

The long term goal of this study is to develop a multi-site and leadless pacing system, which will be capable of addressing the unmet clinical needs of the CRT patients. One potential method of achieving leadless CRT, using six leadless pacemakers implanted at the (1) right atrium, (2) left atrium, (3) right ventricle, (4) left ventricle, (5) right ventricle apex, and (6) left ventricle apex, of a

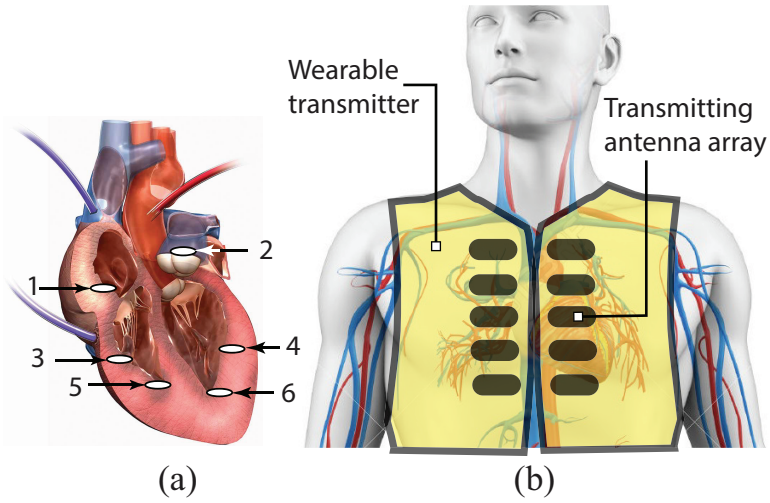

Figure 5.16. An conceptual illustration envisioning the implantation of (a) multiple leadless pacemakers at (1) right atrium, (2) left atrium, (3) right ventricle, (4) left ventricle, (5) right ventricle apex, and (6) left ventricle apex, and (b) a wearable transmitter with a conformal transmitting antenna array.

human heart model is shown in Fig. 5.16 (a). Furthermore, a wearable transmitter with a conformal transmitting antenna array is depicted in Fig. 5.16 (b). This concept is similar to that mentioned in [13].

5.8. Conclusion and Future Work

In this chapter, a novel wide-band numerical model has been designed and developed for deeply implantable antennas. More specifically, it is shown that a commercially available tissue simulating liquid (TSL) can be used to design a numerical model in HFSS. This model was further validated experimentally and analytically using a reference microstrip patch antenna. The application of this numerical model was demonstrated by the design and development of a metamaterial-based deeply implantable conformal antenna. Furthermore, integration of the proposed antenna with a model of a leadless pacemaker was presented as a solution to tackle the multi-site pacing needs for patients requiring CRT. Overall, the simulated and measured results of the characterization of TSL, reference microstrip patch antenna, and the proposed conformal antenna, were found to be in good agreement with each other.

In future, the proposed antenna will be integrated with an efficient rectifier and matching circuit, so that energy harvesting in deep tissue can be demonstrated, at 2.45 GHz, for leadless

pacing. Moreover, a detailed safety analysis including the compliance of specific absorption rate, maximum permissible exposure, biocompatibility and electromagnetic interference (etc.) has to be completed before considering any preclinical testing of this system. Overall, this work has a great potential for growth, as it can be extended to wireless powering of other deeply implantable biomedical sensors.

5.9. References

[1] W. D. Widmann *et al.*, "Radio-frequency cardiac pacemaker," *Ann. N. Y. Acad. Sci.*, pp. 992–1006, 1964.

[2] C. Cammilli *et al.*, "Radio-frequency pacemaker with receiver coil implanted on the heart," *Ann. N. Y. Acad. Sci.*, vol. 111, pp. 1749–6632, 1964.

[3] R. Bashirullah, "Wireless implants," *IEEE Microwave*, vol. 11, no. 7, pp. S14–S23, Dec 2010.

[4] S. M. Asif *et al.*, "Design and in vivo test of a batteryless and fully wireless implantable asynchronous pacing system," *IEEE Trans. Biomed. Eng.*, vol. 63, no. 5, pp. 1070–1081, May 2016.

[5] T. Campi *et al.*, "Wireless power transfer charging system for AIMDs and pacemakers," *IEEE Trans. Microw. Theory Tech.*, vol. 64, no. 2, pp. 633–642, Feb 2016.

[6] S. Cruciani *et al.*, "Induced effects in a pacemaker equipped with a wireless power transfer charging system," *IEEE Trans. Magn.*, vol. PP, no. 99, pp. 1–1, 2017.

[7] M. Miller *et al.*, "Leadless cardiac pacemakers- back to the future," *J. Amer. Coll. Cardiol.*, vol. 66, no. 10, pp. 1179–1189, Sep 2015.

[8] Carnegie School of Engineering. (2017, June 5). [Online]. Available: https://www.engineering.cmu.edu

[9] A. Haeberlin *et al.*, "The first batteryless, solar-powered cardiac pacemaker," *Heart Rhythm*, vol. 12, no. 6, pp. 1317 – 1323, 2015.

[10] J. Olivo *et al.*, "Energy harvesting and remote powering for implantable biosensors," *IEEE Sensors J.*, vol. 11, no. 7, pp. 1573–1586, July 2011.

[11] Medtronic Inc., MN, USA. (2017, June 5). [Online]. Available: http://medtronic.com/us-en/micra.html

[12] St. Jude Medical Inc., MN, USA. (2017, June 5). [Online]. Available: http://sjmglobal.com/en-int/sjm/leadlesspacing.

[13] D. L. Ewert *et al.*, "Intelligent self-organizing electrode stimulation delivery system," U.S. Patent 8,977,358, March 10, 2014.

[14] Schmid & Partner Engineering AG. (2016, October 5). [Online]. Available: http://www.speag.com/products/

[15] D. H. Werner and Z. H. Jiang, "Antennas, phantoms, and body-centric propagation at millimeter-waves," in *Electromagnetics of Body Area Networks*, First ed. New Jersey: Wiley 2016., pp. 159–203.

[16] F. Merli, "Implantable antenna for biomedical applications," Ph.D. dissertation, Swiss Federal Institute of Technology, 2011.

[17] A. Kiourti and K. S. Nikita, "A review of in-body biotelemetry devices: Implantables, ingestibles, and injectables," *IEEE Trans. Biomed. Eng.*, vol. PP, no. 99, pp. 1–1, 2017.

[18] P. S. Hall and Y. Hao, *Antenna and Propagation For Body-Centric Wireless Communications*, 2nd ed. Artech House, 2006.

[19] R. A. Bercich *et al.*, "Far-field RF powering of implantable devices: Safety considerations," *IEEE Trans. Biomed. Eng.*, vol. 60, no. 8, pp. 2107–2112, Aug 2013.

[20] J. W. Hansen *et al.*, "A far-field radio-frequency experimental exposure system with unrestrained mice," *Springerplus*, vol. 4, pp. 1–13, Nov. 2015.

[21] L. Marnat *et al.*, "On-chip implantable antennas for wireless power and data transfer in a glaucoma-monitoring," *IEEE Antennas Wireless Propag. Lett.*, vol. 11, pp. 1671–1674, 2012.

[22] F.-J. Huang *et al.*, "Rectenna application of miniaturized implantable antenna design for triple-band biotelemetry communication," *IEEE Trans. Antennas Propag.*, vol. 59, no. 7, pp. 2646–2653, Jul. 2011.

[23] S. Hu *et al.*, "A low-cost 2.45-GHz wireless power link for biomedical devices," in *IEEE Asia-Pacific Conf. Antennas Propag.*, Singapore, 27-29 Aug., 2012.

[24] A. Poon *et al.*, "Optimal frequency for wireless power transmission into dispersive tissue," *IEEE Trans. Antennas Propag.*, vol. 58, no. 5, pp. 1739–1750, May 2010.

[25] A. Moglia *et al.*, "Recent patents on wireless capsule endoscopy," *Recent Patents Biomed. Eng.*, vol. 1, no. 1, pp. 24–33, Oct. 2008.

[26] J. Hao *et al.*, "Wireless power transfer to deep-tissue microimplants," *PNAS*, vol. 111, no. 22, pp. 7974–7979, June. 2014.

[27] A. Kiourti *et al.*, "A wireless fully passive neural recording device for unobtrusive neuropotential monitoring," *IEEE Trans. Biomed. Eng.*, vol. 63, no. 1, pp. 131–137, Jan. 2016.

[28] X. Li, "Body matched antennas for microwave medical applications," Ph.D. dissertation, Karlsruhe Institute of Technology, 2014.

[29] K. R. Foster and H. P. Schwan, "Dielectric properties of tissues and biological materials: a critical review," *Critical Reviews in Biomedical Engineering*, vol. 17, no. 1, pp. 25–104, Nov. 1989.

[30] ANSYS HFSS. (2017, April 5). [Online]. Available: http://www.ansys.com/products/electronics-designstudio/ansys-hfss

[31] CST-Computer Simulation Technology, Microwave Studio. (2017, April 5). [Online]. http://www-cst.com/products/cstmws

[32] SPEAG Sim4Life. (2017, April 5). [Online]. Available: https://www.zurichmedtech.com/

[33] P. Soontornpipit *et al.*, "Design of implantable microstrip antenna for communication with medical implants," *IEEE Trans. Microw. Theory Techn.*, vol. 52, no. 8, pp. 1944–1951, Aug. 2004.

[34] J. Kim and Y. Rahmat-Samii, "Implanted antennas inside a human body: simulations, designs, and characterizations," *IEEE Trans. Microw. Theory Techn.*, vol. 52, no. 8, pp. 1934–1943, Aug. 2004.

[35] A. Kiourti and K. Nikita, "A review of implantable patch antennas for biomedical telemetry: Challenges and solutions," *IEEE Antennas Propagat. Mag.*, vol. 54, no. 3, pp. 210–228, Jun. 2012.

[36] T. Karacolak *et al.*, "Design of a dual-band implantable antenna and development of skin mimicking gels for continuous glucose monitoring," *IEEE Trans. Microw. Theory Techn.*, vol. 56, no. 4, pp. 1001–1008, Apr. 2008.

[37] Z. Noroozi and F. Hojjat-Kashani, "Three-dimentional FDTD analysis of the dual-band implantable antenna for continuous glucose monitoring," *Progress Electromag. Research Lett.,*, vol. 28, pp. 9–21, Apr. 2012.

[38] C. Gabriel, *Compilation of the Dielectric Properties of Body Tissues at RF and Microwave Frequencies.* Brooks Air Force, TX, USA.: Tech. Rep. Report N.AL/OE-TR-. 31-CB, 1996.

[39] F. A. Duck, *Physical Properties of Tissues: A comprehensive Reference Book.* Elsvier Ltd., 1990.

[40] M. Lazebnik *et al.*, "Tissue-mimicking phantom materials for narrowband and ultrawideband microwave applications," *Phys. Med. Biology*, vol. 50, no. 18, pp. 4245–4258, 2005.

[41] J. Garrett and E. Fear, "Stable and flexible materials to mimic the dielectric properties of human soft tissues," *IEEE Antennas Wireless Propag. Lett.*, vol. 13, pp. 599–602, 2014.

[42] A. W. Guy, "Analyses of electromagnetic fields induced in biological tissues by thermographic studies on equivalent phantom models," *IEEE Trans. Microw. Theory Techn.*, vol. 19, no. 2, pp. 205–214, February 1971.

[43] N. Chahat *et al.*, "New method for determining dielectric properties of skin and phantoms at millimeter waves based on heating kinetics," *IEEE Trans. Microw. Theory Techn.*, vol. 60, no. 3, pp. 827–832, March 2012.

[44] A. T. Mobashsher and A. M. Abbosh, "Three-dimensional human head phantom with realistic electrical properties and anatomy," *IEEE Antennas Wireless Propag. Lett.*, vol. 13, pp. 1401–1404, 2014.

[45] Y. Nikawa *et al.*, "Soft and dry phantom modeling material using silicone rubber with carbon fiber," *IEEE Trans. Microw. Theory Techn.*, vol. 44, no. 10, pp. 1949–1953, Oct 1996.

[46] J. T. Chang *et al.*, "A conductive plastic for simulating biological tissue at microwave frequencies," *IEEE Trans. Electromagn. Compat.*, vol. 42, no. 1, pp. 76–81, Feb 2000.

[47] SPEAG, Human Body Tissue Simulating Liquids. (2017, April 5). [Online]. Available: http://www.speag.com/products/dasy6/tissue-simulating-liquids

[48] SPEAG, Dielectric Probe Kit. (2017, April 5). [Online]. Available: http://www.speag.com/-products/dak/dielectric-measurements/

[49] Keysight Technologies, USA. (2016, March 1). [Online]. Available: http://www.keysight.com

[50] W. L. Stutzman and G. A. Thiele, *Antenna Theory and Design*, 3rd ed. New York: Wiley, 2012.

[51] C. A. Balanis, *Antenna Theory and Design*, 4th ed. New York: Wiley, 2016.

[52] J. D. Baena *et al.*, "Equivalent-circuit models for split-ring resonators and complementary split-ring resonators coupled to planar transmission lines," *IEEE Trans. Microw. Theory Techn.*, vol. 53, no. 4, pp. 1451–1461, April 2005.

6. CONCLUSIONS AND FUTURE WORK

This chapter concludes the work performed in this study. In addition, specific contributions are highlighted, as well as, limitations and final remarks are discussed. Finally, possible directions for future work are presented.

6.1. Summary of Findings and Conclusions

The overall goal of this study was to develop a novel leadless and batteryless cardiac pacemaker. To achieve this major goal and also to address the specific objectives mentioned in Chapter 1, this work was divided into three main parts: development of a path loss (PL) model; design, development, and manufacturing of a prototype leadless pacemaker and demonstration of leadless pacing using radio frequency (RF) energy wireless power transfer; and design, development, and validation of a numerical model for deeply implantable antennas.

First, an analysis of the results of a series of propagation experiments on ovine models shows that a PL model can be developed to predict the available RF power at an implant location, 6 cm deep, inside the body. Following the uncertainty analysis and analytical computations, it was concluded that the approximate PL for the given models at 1.2 GHz was 21 ± 2.0346 dB. This PL model was validated in an anechoic chamber using various methods. Furthermore, the results obtained from these various methods showed a good agreement.

Following the prediction of available RF power at an implant location inside an ovine model, it was shown that a metamaterial-based miniaturized, but efficient, implantable antenna can be designed and developed to attain the link budget requirements for wireless powering of an implantable device. Overall, a compact leadless pacemaker, comprised of an implantable antenna and matching, rectifier, pacing, and charging circuits, was fabricated and tested in vivo in an ovine model. It was demonstrated that a compact prototype leadless pacemaker, measuring $12\,mm \times 10\,mm \times 1.5\,mm$, achieved leadless pacing in ovine models at a recommended RF energy level. It was concluded that the proposed method of wireless energy transfer, at 1.2 GHz, for deeply implantable devices such as pacemakers, is safe and practically achievable.

Finally, it was shown that a commercially available tissue simulating liquid (TSL) can be fully characterized and used to devise a numerical model in HFSS. This proposed numerical model

was validated experimentally as well as analytically. It was concluded that this numerical model, when coupled with the TSL, could provide a good platform for the design, development, optimization, and measurement of deeply implantable antennas for leadless pacing or other biomedical implantable devices.

6.2. Summary of Contributions

Chapter 3 has focused on the development and validation of a PL model, which was important for the estimation of the available RF power at the implant location deep inside the body. In order to understand propagation loss in an environment similar to a human body, in vivo experiments were performed on ovine models. Results from the experiments were analyzed, which helped determine a frequency of 1.2 GHz for wireless power transmission. The PL at this frequency band was observed to be relatively low and was computed to be approximately 3.5 dB/cm. A comprehensive uncertainty analysis of the equipment was performed and the overall estimated power at the implant location, 6 cm deep inside the body, was computed to be 21 ± 2.0346 dB. The method and results presented in this chapter are novel and presented for the first time.

The in-depth details of the implantable rectenna design, fabrication of the prototype leadless pacemaker, and the in vivo experiments, as well as the testing of the pacemaker were discussed in Chapter 4. The rectenna module, which included a rectifier and matching circuit, was responsible for the receiving of the RF waves deep inside the body and then efficiently converting them to usable power for the pacing circuit. The pacing circuit comprised of a microprocessor provided pacing at various rates (110, 120, and 130 bpm). This leadless pacemaker was designed using a 3D EM solver, HFSS and then prototype was fabricated and tested in vivo in an ovine model, after implanting it on the epicardial surface of the left ventricle. The RF energy however, was transmitted to the implanted electrode using a horn antenna positioned 25 cm above the thorax of the ovine model. It was demonstrated that a small implanted electrode can capture and harvest enough recommended RF energy to achieve pacing. Electrocardiogram (ECG) signals were recorded during the experiments, which demonstrated asynchronous pacing achieved at three different rates. These results show that the proposed method has great potential for stimulating the heart and provides pacing without requiring any leads or batteries. This method for leadless pacing is novel and has the potential to be extended to other biomedical implantable devices.

In Chapter 5, the implantable antenna design technique was advanced further and a wide-band numerical model based on the commercially available tissue simulating liquid (TSL) was proposed. Design, development, and optimization of this model was performed in a 3D full wave electromagnetic tool, HFSS. Using a reference antenna (a microstrip patch), the proposed model was validated experimentally as well analytically. Finally, the application of this numerical model was demonstrated by the design, development, and manufacture of a novel conformal antenna, at 2.45 GHz, for leadless pacing applications. The simulated results of this proposed antenna was in good agreement with TSL measurements, which further increased the validity of the proposed numerical model.

6.3. Limitations and Final Remarks

The work proposed in this dissertation is novel, but has limitations, which are briefly discussed below.

Wireless power transfer to achieve leadless pacing using a horn antenna, held on the top of a subject, might not seem practical. However, the aim of this work was to prove the concept of wireless energy transfer in vivo and the feasibility of leadless cardiac pacing. Also, the RF energy transfer was demonstrated at 1.2 GHz, which is not an open band. This operating frequency was selected following a set of preliminary experiments indicating that this band produced good propagation through the tissue and also, this frequency matched efficient performance of the available Schottky diodes, which resulted in a more efficient rectifier circuit. Yet because the prototype leadless pacemaker was not biocompatible, a newer version of leadless pacemaker with biocompatibility has to be redeveloped.

Moreover, in order to make a practical leadless pacing system, the next version of this leadless pacemaker must satisfy all the stringent compliance and regulatory requirements set by FCC (Federal Communications Commission) and FDA (Food and Drug Administration). The clinical use of this system will require (a) a wearable battery operated transmitter system with a miniaturized conformal antenna, and (b) a miniaturized cylindrical shaped biocompatible electrode that can be fully inserted into the myocardium.

Although there are limitations of this work, the proposed method of wireless powering of a cardiac pacemaker demonstrated in this dissertation has the advantage of potentially lasting indefinitely and may never require replacement during the life of the patient. This method brings

forward transformational possibilities in wireless cardiac pacing, and also in powering many other implantable medical devices and sensors. In this study, an initial working system is proposed for leadless pacing but the main challenge is to integrate this wireless powering technique with the existing implantable medical devices. Any further advancement in this area would need major funding and a collaboration with an established medical device company. Possible research directions are presented in the next section.

6.4. Recommendations for Future Work

Using RF energy for wirelessly powering implantable devices opens a new frontier of research in the area of implantable medical devices. To improve existing prototype pacemakers, CMOS technology can be employed to design and manufacture efficient rectifiers and matching circuits. This alone will help to achieve miniaturization of the overall prototype and minimize power requirements. Furthermore, more efficient implantable antennas with good gain and improved form factors can be investigated. Moreover, while open band at 2.45 GHz can be used, other available bandwidths can also be considered in order to achieve a better tradeoff.

In addition to the aforementioned recommendations, work can be performed on the design and development of a more practical and wearable wireless transmitter system with the ability for on-demand wireless energy transmission for such implantable applications. Wearable or on-body antennas can be investigated for a system that is flexible to wear and comply with all the stringent regulations enforced by FCC, FDA, and other regulatory bodies. Safety considerations such as specific absorption rate (SAR) limits for such systems can also be investigated in great details.

In short, it is argued that once fully proven, this proposed method has the potential to revolutionize the way power is delivered to implantable medical devices not just pacemakers. Indeed, there are many open research questions that can lead to new knowledge that can directly affect quality of life of human.

APPENDIX A. SPECIFIC ABSORPTION RATE (SAR): POWER DENSITY AND ELECTRIC FIELD INTENSITY

A.1. Introduction

An electromagnetic (EM) wave in any medium is characterized by its frequency, electric and magnetic field intensity, direction, and polarization. The interaction of the EM wave with the biological tissue produces spatial variation in electrical and magnetic field intensities, which can be mathematically solved using Maxwell's equations for the given boundary conditions. The magnetic permeability of human tissues is practically equal to the permeability of the free space, meaning that human biological tissue is non-magnetic [1]. On the other hand, other relevant parameters, such as permittivity and conductivity of the biological tissue is not equal to the values in free space. These parameters are different for different tissues and are dependent on the frequency, magnitude and direction of the applied electric field, and the function of position [2]. Therefore, a homogeneous lossy medium having permeability (μ), permittivity ($\epsilon = \epsilon^{'} - j\epsilon^{''}$), and conductivity ($\sigma$) can be a better approximation of human tissue [1]. Maxwell's equations are usually used to solve boundary-value electromagnetic problems. The Maxwell's equations are written in either differential form or integral form [2]. This article starts with the theoretical and analytical solution of Maxwell's equations leading to the general form of law of conservation of energy. For a source free homogeneous lossy medium, differential form of Maxwell's equations can be written as [2]:

$$\vec{\nabla} \times \vec{\mathscr{E}} = -\frac{\partial \vec{\mathscr{B}}}{\partial t} \tag{A.1}$$

$$\vec{\nabla} \times \vec{\mathscr{H}} = \frac{\partial \vec{\mathscr{D}}}{\partial t} + \vec{\mathscr{J}} \tag{A.2}$$

$$\vec{\nabla}.\vec{\mathscr{D}} = 0 \tag{A.3}$$

and

$$\vec{\nabla}.\vec{\mathscr{B}} = 0. \tag{A.4}$$

All of these field quantities $\vec{\mathscr{E}}$, $\vec{\mathscr{B}}$, $\vec{\mathscr{H}}$, $\vec{\mathscr{D}}$, and $\vec{\mathscr{J}}$ are time varying, and each is a function of space coordinates, and time, i.e., $\vec{\mathscr{E}} = \vec{\mathscr{E}}(x, y, z, t)$. The definitions and units of these quantities are as follows:

$\vec{\mathscr{E}}$ = electric field intensity (volts/meter),

$\vec{\mathscr{H}}$ = magnetic field intensity (amperes/meter),

$\vec{\mathscr{D}}$ = electric flux field density (coulombs/square meter),

$\vec{\mathscr{B}}$ = magnetic flux field density (webers/square meter),

$\vec{\mathscr{J}}$ = conduction electric current density (amperes/square meter),

$\vec{\nabla}$ = the differential operator called 'del'.

A.2. Conservation of Energy

Maxwell's equations in differential form for general time varying EM fields were presented in the previous section. Electromagnetic (EM) fields are used to carry information over a distance. For this information transportation, energy is associated with these EM fields. The energy forms associated with these EM fields are interpreted from the derivation of the Maxwell's equations.

For a source free medium in which an EM wave is propagating, the behavior of the associated electric and magnetic fields are shown in (A.1) and (A.2). Scalar multiplying $\vec{\mathscr{H}}$ and $\vec{\mathscr{E}}$ on both sides of (A.1) and (A.2), respectively, gives the following relationship.

$$\vec{\mathscr{H}}.\left(\vec{\nabla} \times \vec{\mathscr{E}}\right) = -\vec{\mathscr{H}}.\left(\frac{\partial \vec{\mathscr{B}}}{\partial t}\right), \tag{A.5}$$

and

$$\vec{\mathscr{E}}.\left(\vec{\nabla} \times \vec{\mathscr{H}}\right) = \vec{\mathscr{E}}.\left(\frac{\partial \vec{\mathscr{D}}}{\partial t} + \vec{\mathscr{J}}\right). \tag{A.6}$$

Now by subtracting (A.5) from (A.6), we get,

$$\vec{\mathscr{H}}.(\vec{\nabla} \times \vec{\mathscr{E}}) - \vec{\mathscr{E}}.(\vec{\nabla} \times \vec{\mathscr{H}}) = -\vec{\mathscr{H}}.(\frac{\partial \vec{\mathscr{B}}}{\partial}) - \vec{\mathscr{E}}.(\frac{\partial \vec{\mathscr{D}}}{\partial} + \vec{\mathscr{J}}), \tag{A.7}$$

and using vector identity,

$$\vec{\nabla}.(\vec{\mathbf{A}} \times \vec{\mathbf{B}}) = \vec{\mathbf{B}}.(\vec{\nabla} \times \vec{\mathbf{A}}) - \vec{\mathbf{A}}.(\vec{\nabla} \times \vec{\mathbf{B}}). \tag{A.8}$$

Now, using (A.8), the left side of (A.7) can be rewritten as,

$$\vec{\nabla}.(\vec{\mathscr{E}} \times \vec{\mathscr{H}}) = \vec{\mathscr{H}}.(\vec{\nabla} \times \vec{\mathscr{E}}) - \vec{\mathscr{E}}.(\vec{\nabla} \times \vec{\mathscr{H}}) \tag{A.9}$$

and

$$\vec{\nabla}.(\vec{\mathscr{E}} \times \vec{\mathscr{H}}) = -\vec{\mathscr{H}}.(\frac{\partial \vec{\mathscr{B}}}{\partial}) - \vec{\mathscr{E}}.(\frac{\partial \vec{\mathscr{D}}}{\partial}) + \vec{\mathscr{E}}.\mathscr{J}. \tag{A.10}$$

Since, $\vec{\mathscr{D}} = \epsilon.\vec{\mathscr{E}}$,

$$\vec{\mathscr{E}}.(\frac{\partial \vec{\mathscr{D}}}{\partial t}) = \epsilon\vec{\mathscr{E}}.(\frac{\partial \vec{\mathscr{E}}}{\partial}) = \frac{1}{2}\epsilon(\frac{\partial \vec{\mathscr{E}}}{\partial t}.\vec{\mathscr{E}} + \vec{\mathscr{E}}.\frac{\partial \vec{\mathscr{E}}}{\partial}) = \frac{\partial}{\partial t}(\frac{1}{2}\epsilon\vec{\mathscr{E}}.\vec{\mathscr{E}}). \tag{A.11}$$

Similarly,

$$\vec{\mathscr{H}}.(\frac{\partial \vec{\mathscr{B}}}{\partial t}) = \frac{\partial}{\partial t}(\frac{1}{2}\mu\vec{\mathscr{H}}.\vec{\mathscr{H}}) \tag{A.12}$$

and also

$$\vec{\mathscr{J}} = \sigma\vec{.\mathscr{E}}. \tag{A.13}$$

Substituting the values of (A.11), (A.12), (A.13) in (A.9) and after rearranging, we get,

$$\vec{\nabla}.(\vec{\mathscr{E}} \times \vec{\mathscr{H}}) + \frac{\partial}{\partial t}(\frac{1}{2}\epsilon\vec{\mathscr{E}}\vec{\mathscr{E}}) + \frac{\partial}{\partial t}(\frac{1}{2}\mu\vec{\mathscr{H}.\mathscr{H}}) + \sigma\vec{\mathscr{E}}.\vec{\mathscr{E}} = 0. \tag{A.14}$$

Now, integrating (A.14) over the volume V and applying divergence theorem on the first term, we get,

$$\oint_S (\vec{\mathscr{E}} \times \vec{\mathscr{H}})dS + \frac{\partial}{\partial t}\int_V \left[\frac{1}{2}\epsilon\vec{\mathscr{E}}.\vec{\mathscr{E}} + \frac{1}{2}\mu\vec{\mathscr{H}}.\vec{\mathscr{H}}\right] dV + \int_V (\sigma\vec{\mathscr{E}}.\vec{\mathscr{E}})dV = 0. \tag{A.15}$$

Whereas,

$\oint_S(\vec{\mathscr{E}} \times \vec{\mathscr{H}})dS = S$, total power leaving the volume (through the surface S) (Watts),

$\frac{1}{2}\epsilon\vec{\mathscr{E}}.\vec{\mathscr{E}} = P_e$ stored electric energy density inside volume V (Joules/m^3),

$\frac{1}{2}\epsilon\vec{\mathscr{H}}.\vec{\mathscr{H}} = P_m$, stored magnetic energy density inside volume V (Joules/m^3),

$\frac{\partial}{\partial t}\int_V \left[\frac{1}{2}\epsilon\vec{\mathscr{E}}.\vec{\mathscr{E}} + \frac{1}{2}\mu\vec{\mathscr{H}}.\vec{\mathscr{H}}\right] dV$ = rate of increase of stored energy inside volume V, and

$\int_V(\sigma\vec{\mathscr{E}}.\vec{\mathscr{E}})dV$ = power lost to heat inside volume V.

However, in many practical systems, the time varying EM waves are sinusoidal and are referred to as *time-harmonic*. Thus, for time harmonic fields, instantaneous fields, and current densities can be related to their complex forms by,

$$\vec{\mathscr{E}}(x, y, z, t) = \Re[\vec{\mathbf{E}}(x, y, z)e^{j\omega t}] \tag{A.16}$$

and

$$\vec{\mathscr{H}}(x, y, z, t) = \Re[\vec{\mathbf{H}}(x, y, z)e^{j\omega t}]. \tag{A.17}$$

Where $\vec{\mathscr{E}}$ and $\vec{\mathscr{H}}$ represent the instantaneous field vectors, while $\vec{\mathbf{E}}$ and $\vec{\mathbf{H}}$ represent the corresponding complex spatial forms which are only a function of time.

For a plane wave EM wave propagating in the z-direction in a lossy medium having $\vec{\mathscr{E}}$ in x-direction and $\vec{\mathscr{H}}$ in y-direction, the time harmonic EM wave can be simplified. A layout of this case is illustrated in Fig. A.1.

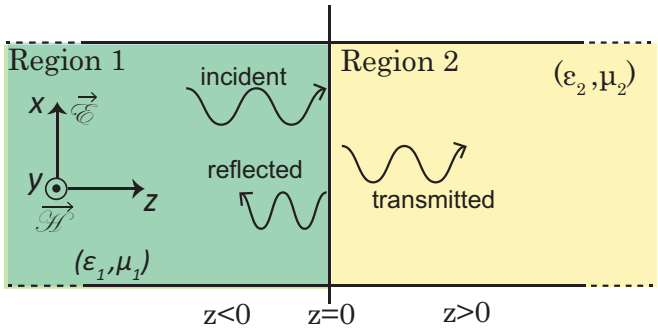

Figure A.1. An electromagnetic plane wave travelling in the +z direction in a lossy medium ($\vec{\mathscr{E}}$ in x- direction and $\vec{\mathscr{H}}$ in y-direction).

Mathematically, it can be written as,

$$\vec{\mathbf{E}} = E_o cos(\omega t + \beta z)\hat{a_x} \tag{A.18}$$

and

$$\vec{\mathbf{B}} = B_o cos(\omega t + \beta z)\hat{a_y}. \tag{A.19}$$

Thus, the energy stored by a time harmonic EM wave defined by (A.18) and (A.19) will be,

$$\begin{aligned} \frac{1}{2}\epsilon\vec{\mathscr{E}}.\vec{\mathscr{E}} &= \frac{1}{2}\epsilon E_o cos(\omega t + \beta z)\hat{a_x}.E_o cos(\omega t + \beta z)\hat{a_x} \\ &= \frac{1}{2}\epsilon E_o^2 cos^2(\omega t + \beta z) = \frac{1}{2}\epsilon E_o^2 \overline{cos^2(\omega t + \beta z)}. \end{aligned} \tag{A.20}$$

Where $\overline{cos^2(\omega t + \beta z)}$ is the average intensity of the time harmonic plane wave. The average of square of sinusoidal function over a whole number of periods is $\frac{1}{2}$. This simplifies (A.20),

$$P_e = \frac{1}{4}\epsilon E_o^2 \tag{A.21}$$

and similarly,

$$P_m = \frac{1}{4\mu}B_o^2. \tag{A.22}$$

It can be therefore concluded from (A.21) and (A.22) that (a) the stored electric and magnetic energy density of a time harmonic EM wave will be a constant value, and (b) the rate of increase of the stored energy inside a given volume V will be zero. Thus, (A.15) can be written in the follosing simplified form,

$$-\oint_S (\vec{\mathscr{E}} \times \vec{\mathscr{H}})dS = \int_V (\sigma\vec{\mathscr{E}}.\vec{\mathscr{E}})dV. \tag{A.23}$$

It is therefore implied from (A.23) that the change in total power leaving the volume (through the surface S) for a time harmonic wave is equal to the power lost to heat inside the volume V, as shown in Fig. A.2 .

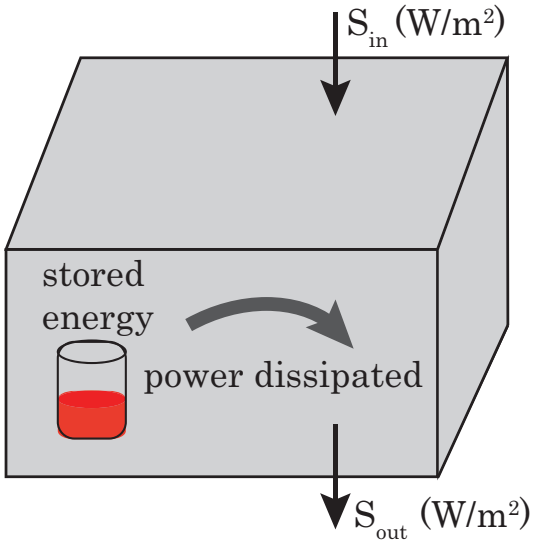

Figure A.2. An illustration of law of conservation of electromagnetic plane wave.

A.3. Specific Absorption Rate (SAR)

The definition of specific absorption rate (SAR) as per IEEE is as follows [3]: The time derivative (rate) of the incremental energy *(dW)* absorbed by (dissipated in) an incremental mass *(dm)* contained in a volume element *(dV)* of a given density (ρ), as

$$SAR = \frac{d}{dt}\left(\frac{dW}{dm}\right) = \frac{d}{dt}\left(\frac{dW}{\rho\, dV}\right).$$

SAR can expressed in watts per kilogram (W/kg) or milliwatts per gram (mW/g).

In simple terms, SAR is the time rate at which electromagnetic wave (EM) is imparted to an element of mass of a tissue [4]. Dividing (A.23) by mass $\triangle m$, we get,

$$-\frac{\oint_S(\vec{\mathscr{E}} \times \vec{\mathscr{H}})dS}{\triangle m} = \frac{\int_V(\sigma\vec{\mathscr{E}}.\vec{\mathscr{E}})dV}{\triangle m}. \tag{A.24}$$

The units of (A.24) are in W/kg, which shows that for a time harmonic EM wave, SAR can be expressed in terms of power density or in terms of volume integral of the electric field intensity. In

other words, with the incremental power $\triangle P$ absorbed by an incremental mass $\triangle m$ contained in a volume element $\triangle V$ of density ρ, the average value of SAR can be shown as,

$$\overline{SAR} = -\frac{\triangle P}{\rho \triangle V}. \tag{A.25}$$

Where $\triangle P = \oint_S (\vec{\mathscr{E}} \times \vec{\mathscr{H}}) dS$. Also, right hand side of (A.24) shows that average SAR can be defined as the power lost to heat inside volume V, averaged over a incremental mass. Furthermore, SAR can also be described as the ratio between the total absorbed in the mass of the body, as reported in [4]. Also using (A.24), SAR can be expressed as,

$$\overline{SAR} = \frac{1}{\triangle m} \int_V (\sigma \vec{\mathscr{E}}.\vec{\mathscr{E}}) dV. \tag{A.26}$$

Thus, it can be interpreted from (A.25) and (A.26) that average value of SAR can be represented in the form of power density and electric field intensity. Also power absorbed can be interpreted as $\triangle P = \triangle S \triangle A$ and $\triangle V = \triangle A \triangle z$. Solving (A.25) and putting values, result another expression of SAR, i.e.,

$$\overline{SAR} = -\frac{\triangle S}{\rho \triangle z} \tag{A.27}$$

In most practical cases, the source of EM radiations is an antenna, the radiated fields of which are divided into near- and far-field regions. The near field is further divided reactive and radiative regions [4]. The electric and magnetic fields in the near-field region of the antenna are complicated and hence their spatial variations in the near-field are difficult to predict. Therefore, it is often inconvenient to express SAR in terms of the power density (poynting vector) in the near-field region of the antenna. Equation (A.26) is an easy form of SAR expression in the near-field region and has been designated as the reference for EM radiation measurements [5]. However, in the far-field region, the EM wave generated by an antenna is approximated as a plane wave, the electric and magnetic field intensities of which are of same magnitudes and orthogonal to the direction of propagation. It is therefore convenient to predict the electric and magnetic field intensities in the far-field region, which can be used to compute the power density and eventually the value of SAR.

A.4. SAR Calculation: Comparison of Simulation and Analytical Solution

A.4.1. Plane wave at boundaries and formulas for the power densities

This section focuses on the phenomenon of reflection which occurs when a plane wave is incident on the boundary between the two regions composed of two different materials. First, the expression for the average power densities in the first region, reflected power density at the boundary of the two different materials, and transmitted power density in the second region will be established.

It was assumed that there is a single vector component of electric field intensity of plane wave resulting the average power density. Referring to Fig. A.1, we define region 1 (ϵ_1, μ_1) as the half space for which $z < 0$; region 2 (ϵ_2, μ_2) is the half space where $z > 0$. Further assuming a plane wave traveling in the $+z$ direction in region 1,

$$E^+_{x1}(z,t) = E^+_{x10} e^{-\alpha z} cos(\omega t - \beta_1 z) \tag{A.28}$$

or

$$E^+_{xs1}(z,t) = E^+_{x10} e^{-jk_1 z}, \tag{A.29}$$

where E^+_{x10} shows the real part. The subscript 1 identifies the region and the superscript + indicates a positively traveling wave. Thus, this plane wave in region 1 traveling in toward the boundary surface at $z = 0$ is called the *incident wave* and is normal incidence. Also the associated magnetic field with $E^1_{z,t}$ is

$$H^+_{ys1}(z,t) = \frac{1}{\eta_1} E^+_{x10} e^{-jk_1 z} \tag{A.30}$$

where k_1 and η_1 is complex wave number and wave impedance of region 1, respectively.

The energy must be transmitted across the boundary surface at $z = 0$ into region 2 by providing a wave moving in the $+z$ direction in that medium,

$$E^+_{xs2}(z,t) = E^+_{x20} e^{-jk_2 z} \tag{A.31}$$

$$H^+_{ys2}(z,t) = \frac{1}{\eta_2} E^+_{x20} e^{-jk_2 z}. \tag{A.32}$$

The wave that moved away from the boundary surface into region 2 is called the *transmitted wave*; for which different propagation constant and intrinsic impedance are used. The boundary conditions at $z = 0$ must be satisfied with these assumed fields. Since E_x is a tangential field; therefore the **E** field in regions 1 and 2 must be equal at $z = 0$. Setting $z = 0$ in A.29 and A.31 implies that $E^+_{10} = E^+_{20}$. As H_y is also tangential and must be continuous. Therefore, letting $z = 0$ will result $\frac{1}{\eta_1} E^+_{10} = \frac{1}{\eta_2} E^+_{20}$; since $E^+_{10} = E^+_{20}$, then $\eta_1 = \eta_2$ [6].

The case discussed above is a very special case that does not fit facts in general and therefore it is unable to satisfy the boundary conditions with only incident and transmitted wave. It is therefore required a traveling wave from the boundary in region 1, as shown in Fig. A.1: this is called *a reflected wave* [4],

$$E^-_{xs1}(z,t) = E^-_{x10} e^{-jk_1 z} \tag{A.33}$$

$$H^-_{ys1}(z,t) = \frac{1}{\eta_2} E^-_{x10} e^{-jk_1 z}. \tag{A.34}$$

where E^-_{x10} may be a complex quantity. Since this field is in the $-z$ direction, $E^-_{xs} = -\eta_1 H^-_{xs}$. This is because of Poynting vector that $\mathbf{E}^-_1 \times \mathbf{H}^-_1$ must be in the $-\mathbf{a}_z$ direction. The boundary conditions are now satisfied. The ratio of amplitudes of the reflected and incident electric fields is called *the reflection coefficient* and can be be found in basic book of EM [6]. This reflection coefficient is designated by Γ,

$$\Gamma = \frac{E^-_{x10}}{E^+_{x10}} = \frac{\eta_2 - \eta_1}{\eta_2 + \eta_1}. \tag{A.35}$$

This reflection coefficient may be complex, in that case there will be a phase shift in the reflected wave [6]. The relative amplitude of the transmitted electric field intensity will be [6],

$$\tau = 1 + \Gamma. \tag{A.36}$$

which is called as *the transmission coefficient*.

By considering the same vector field and regions shown in Fig. A.1, general rule on the transfer of power through reflection and transmission can be formulated by using average power density formula [6]:

$$S_{av} = \frac{1}{2} Re \left\{ \mathbf{E_s} \times \mathbf{H_s^*} \right\}. \tag{A.37}$$

The incident power density will be

$$\begin{aligned} S_{1,av}^{+} = \frac{1}{2} Re \left\{ E_{x10}^{+} H_{y10}^{+} \right\} = \frac{1}{2} Re \left\{ E_{x10}^{+} \frac{1}{\eta_1^*} E_{x10}^{+} \right\} \\ = \frac{1}{2} Re \left\{ \frac{1}{\eta_1^*} \right\} |E_{x10}^{+}|^2. \end{aligned} \tag{A.38}$$

The reflected power density will be

$$\begin{aligned} S_{1,av}^{-} = \frac{1}{2} Re \left\{ E_{x10}^{-} H_{y10}^{-} \right\} = \frac{1}{2} Re \left\{ \Gamma E_{x10}^{+} \frac{1}{\eta_1^*} \Gamma^* E_{x10}^{-*} \right\} \\ = \frac{1}{2} Re \left\{ \frac{1}{\eta_1^*} \right\} |E_{x10}^{-}|^2 |\Gamma|^2. \end{aligned} \tag{A.39}$$

Thus, the relationship between the incident and reflected power can be found:

$$S_{1,av}^{-} = |\Gamma|^2 S_{1,av}^{+}. \tag{A.40}$$

In the similar way, the transmitted power can be computed [6],

$$S_{2,av}^{+} = (1 - |\Gamma|^2) S_{1,av}^{+}. \tag{A.41}$$

A.4.2. Analytical solution of SAR for a lossy medium (skin tissue)

Above section shows the analytical formulation of incident, reflected, and transmitted power through the two different regions. This section focuses on the maximum value of SAR in a skin tissue. The material properties (ϵ, μ, σ, and ρ) of the skin tissues were used from Gabriel data base [7]. Fig. A.3 shows the setup used for the calculation of SAR values and the dielectric propeties

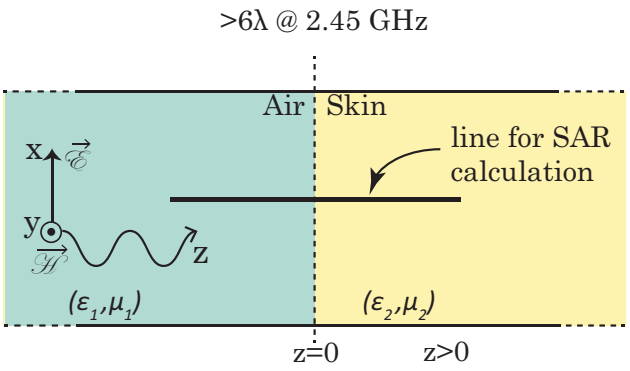

Figure A.3. Transverse electromagnetic wave with fields $\vec{\mathscr{E}}$ and $\vec{\mathscr{H}}$, as well as power density *S(z)* in a lossy medium with permeability μ, permittivity ϵ, and conductivity σ.

of the two mediums. It was assumed that the incident average power density in the region 1 is $400\,W/m^2$ with the assumption of plane wave propagating in the $+$z direction at 2.45 GHz. The values of intrinsic impedance in skin tissue (η_{skin}), attenuation constant (α_{skin}) can be calculated [6].

$$\eta_{skin} = \eta_{air}\sqrt{\frac{\mu_{skin}}{\epsilon_{skin}}} = 61.1070\ \Omega. \tag{A.42}$$

where η_{air} is impedance of the free space i.e. 377 Ω. $\mu_{skin}, \epsilon_{skin}$ are the relative permeability and permittivity of the skin tissue, respectively.

$$\alpha_{skin} = \omega\sqrt{\frac{\mu\epsilon}{2}\left(\sqrt{1+\left(\frac{\sigma_{skin}}{\mu\epsilon}\right)^2}-1\right)} = 43.58\ Np/m \tag{A.43}$$

where $\mu = \mu_{air}\mu_{skin}$, $\epsilon = \epsilon_{air}\epsilon_{skin}$.

Using the values of η for the air and skin, the reflection coefficient can be computed using (A.35) which is 7.21×10^{-1}. Similarly, (A.36) calculates the transmission coefficient of setup shown in Fig. A.1. Therefore, for a 2.45 GHz plane wave normally incident on to the skin tissue (Fig. A.3) of finite thickness having incident power density 400 W/m^2, the fraction of incident power that is reflected and transmitted into the skin tissue can be computed using (A.40) and (A.41), respectively. The calculated values are

$$S_{air}^{-} = 207.936\ W/m^2, \tag{A.44}$$

and

$$S^{+}_{skin} = 192.064\ W/m^2. \tag{A.45}$$

The electric field intensity of a plane wave in any lossy medium falls of as $e^{-\alpha z}$ and the power density attenuates as $e^{-2\alpha z}$ [6]. As shown in Fig. A.3, the region 2 (skin tissue) has finite thickness in the z-direction i.e. 1 cm and then again region 1 starts. So, magnitude of S^{+}_{skin} at z = 1 cm in the skin tissue will be,

$$S^{+}_{skin}(z = 1cm) = 192.064e^{-2\alpha z} = 80.33\ W/m^2, \tag{A.46}$$

and the reflected power density at the skin to air boundary will be

$$S^{-}_{skin}(z = 1\ cm) = |\Gamma|^2 S^{+}_{skin}(z = 1\ cm) = 30.11\ W/m^2. \tag{A.47}$$

A detailed discussion on the SAR formulation has been discussed in Section A.4. A graphical interpretation of SAR is also shown in Fig. A.4. Now, in order to compute 10 g SAR, change in the

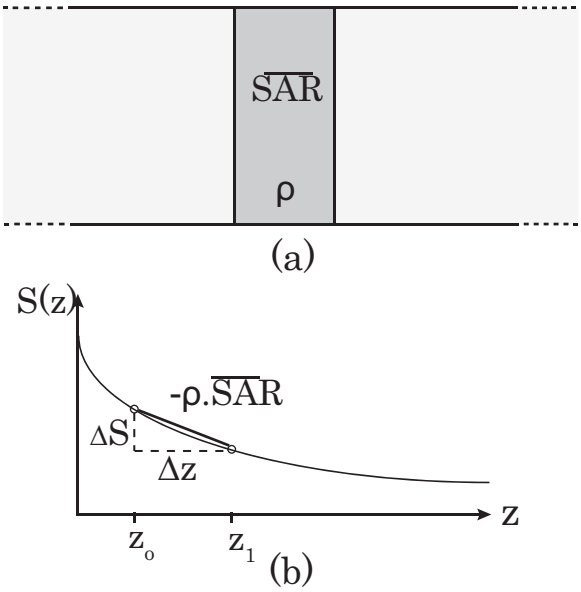

Figure A.4. A graphical interpretation of specific absorption rate.

average power absorbed per unit area was first computed and then (A.27) was used to compute the maximum value of average SAR in the skin tissue. Since mass can be expressed in terms of mass density and volume i.e. $\rho \triangle V = \triangle m$. So, for a specific mass density, mass depends on the volume. The setup in Fig. A.3 shows that there is no reflection other than the x-axis boundary and a more accurate picture of the Fig. A.3 can be obtained if the dimensions of the boundary is greater then 6 λ. For a 2.45 GHz these dimensions should be greater than 0.732 to minimize reflections from the boundaries other than z-axis. For this reason a cube of 1 $m \times 1\ m \times 00.01\ m$ was chosen. Over this area of $1m^2$, if the plane wave travels $9.017 \times 10^{-6}\ m$) then that will constitute total of 10 grams tissue mass. Therefore for $0<z<9.017 \times 10^{-6}\ m$, one power absorption will be because of plane wave traveling in +z direction and second will be because of the wave reflected from the skin to air boundary i.e reflected wave traveling in $-$z direction. Mathematically, it can be written as,

$$\begin{aligned} \triangle S^{+}_{skin} &= 192.064e^{-2(\alpha_{skin})(0)} - 192.064e^{-2(\alpha_{skin})(9.017\times10^{-6})} \\ &= 0.15088 W/m^2. \end{aligned} \tag{A.48}$$

The value of SAR because of the transmitted power can be calculated using (A.27), i.e.,

$$\overline{SAR^{+}_{skin}} = -\frac{\triangle S^{+}_{skin}}{\rho \triangle z} = 15.0890\ W/Kg. \tag{A.49}$$

Similarly, the reflected power density from the skin tissue boundary will be,

$$\begin{aligned} \triangle S^{-}_{skin} &= 30.11e^{-2(\alpha_{skin})(9.99909\times10^{-3})} - 30.11e^{-2(\alpha_{skin})(0.01)} \\ &= 0.01098212\ W/m^2. \end{aligned} \tag{A.50}$$

Similarly, SAR because of the reflected can be calculated using (A.27),

$$\overline{SAR^{-}_{skin}} = -\frac{\triangle S^{+-}_{skin}}{\rho \triangle z} = 1.09822\ W/Kg. \tag{A.51}$$

The total value of SAR over 10 g of tissue will be as follows:

$$\overline{SAR_{skin}^{TOTAL}} = \overline{SAR_{skin}^{+}} + \overline{SAR_{skin}^{+}} = 16.17\ W/Kg. \tag{A.52}$$

A.4.3. HFSS simulation for the SAR evaluation at a skin tissue

For the comparison of the analytical results with the simulation results, a similar setup shown in Fig. A.3 was modeled in HFSS. The SAR was plotted along a line in the modeled setup. A complete setup of the simulation model with the plane wave excitation is shown in Fig. A.5. The direction of propagation was defined by the durection of 'K', which was in -y direction in this case. The spatial peal SAR value (10 gm avg) obtained using the IEEE standard 62704 (in HFSS) was observed to be 15.42 W/kg., whereas the average value of SAR calculated analytically over 10 gm of skin tissue was 16.17 W/kg.

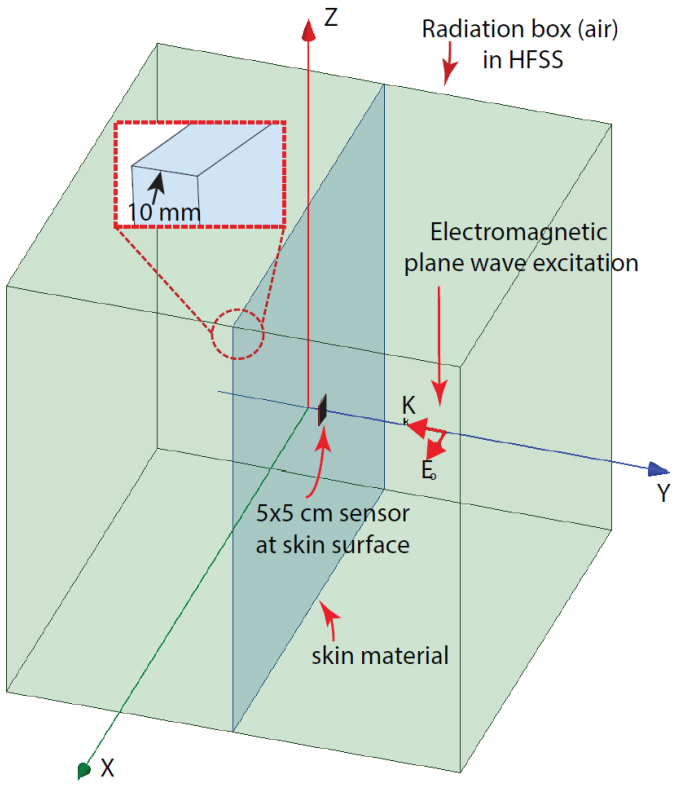

Figure A.5. A layout of the model setup in HFSS, showing plane wave excitation and a skin tissue model.

A.5. Conclusions

The analytical derivations of the SAR expression from the Maxwell's equations showed that SAR can be expressed in terms of power density or also in terms of power lost as heat in any given volume for a time harmonic EM wave. When a human tissue is exposed in the near-field region of an antenna, it is convenient to measure the electric field intensity of the EM field and express SAR in terms of power dissipated inside the volume over an incremental mass. It can also be concluded that when a human tissue is exposed in the far-field of the antenna, SAR can be expressed as a ratio between the power density and the mass of the exposed human tissue. Furthermore, the comparison of the SAR between the analytical and simulation results showed that for an average incident power density of the 400 W/m^2 , SAR exceed the limitation provided by the IEEE. It can be also concluded that simulation results agree well the analytical results.

A.6. References

[1] M. Hampe, "Specific absorption rate in human tissues: Accurate and approximated values," in *IEEE Int. Conf. Elect. Compat.*, Brugge, Belgium, 2-6 Sept.. 2013 2013.

[2] W. L. Stutzman and G. A. Thiele, *Antenna Theory and Design.* 3rd Edition, New York: Wiley, 2012, pp. 100–127.

[3] *IEEE Recommended Practice for Determining the Peak Spatial-Average Specific Absorption Rate (SAR) in the Human Head from Wireless Communications Devices: Measurement Techniques*, IEEE standard 1528-2013.

[4] Y. A. Sambo *et al.*, "A survey and tutorial of electromagnetic radiation and reduction in mobile communication systems," *IEEE Commun. Surveys Tutorials*, vol. 17, no. 2, pp. 790–802, Secondquarter 2015.

[5] ICNIRP, "Guidelines for limiting exposure to time-varying electric, magnetic, and electromagnetic fields (up to 300 GHz)," *Health Physics Society*, vol. 4, no. 74, pp. 494–522, Nov. 1997.

[6] W. H. Hayt and J. H. Buck, *Engineering Electromagnetic.* 6ˆth Edition, McGraw Hill, 2012, pp. 100–127.

[7] Italian International Research Council. (2016, June 5). [Online]. Available: http://niremf.ifac.crn.-it/tissprop/

APPENDIX B. PICTURES OF THE PROTOTYPE LEADLESS PACEMAKER

Various pictures of the prototype leadless pacemaker are shown in Fig. B.1.

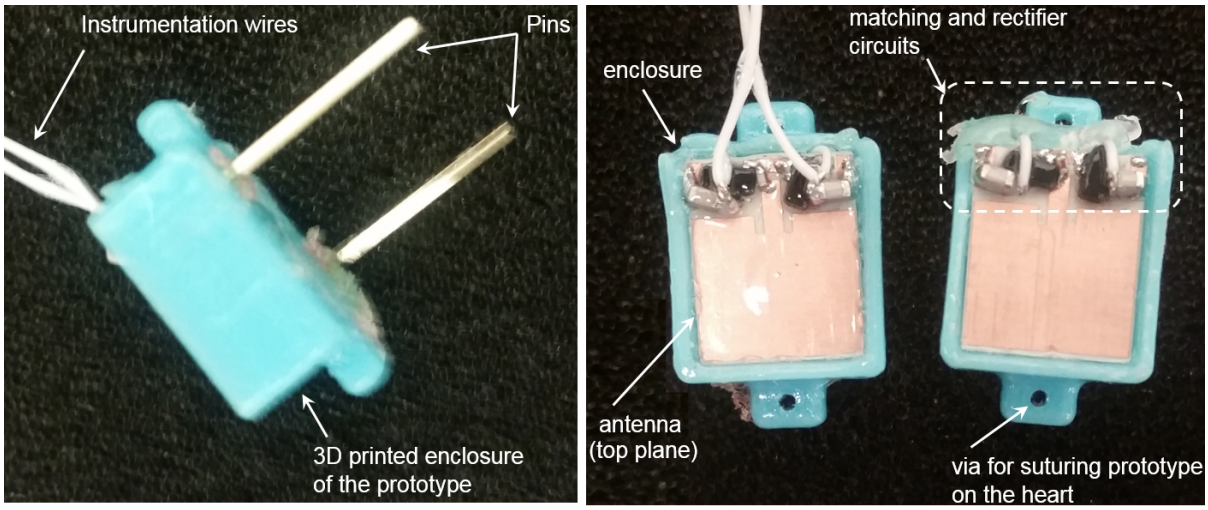

Figure B.1. Pictures of the fabricated leadless pacemaker. (a) A perspective view of the leadless pacemaker with pins and instrumentation wires shown. (b) Two prototype leadless pacemakers, one with instrumentation wires and the second without instrumentation wires.

APPENDIX C. VITA

Sajid Asif was born in May 1981, in Attock, Pakistan. He received the B.S. degree in Electrical Engineering (Communication) from the University of Engineering and Technology, Taxila, Pakistan in 2004, and the M.S. degree in Radio Frequency Communication Engineering from the University of Bradford, UK, in 2006. He achieved 3rd top position in B.S. class achieving a CGPA of 3.48/4.0, and a grade of Merit in M.S. degree.

He was a faculty member in Pakistan, before enrolling into PhD studies at North Dakota State University (NDSU), USA, in August, 2013. At NDSU, he has mainly worked as a Research Assistant, but also taught as an Instructor. Sajid has authored and co-authored 42 peer-reviewed journal and conference papers. His research interests include RF/microwave circuits, antenna miniaturization, frequency reconfigurable antennas, implantable antennas, wireless sensors, RF energy harvesting, and topics related to EMC/EMI.

Mr. Asif has received numerous awards and scholarships during his academic career. He was the recipient of the NSF EPSCOR Doctoral Dissertation Assistantship (2014-2016), IEEE Antenna and Propagation Society Research Award (2015), IEEE Outstanding Student Award (2016), and NDSU CoE Research Assistant of the Year Award (2017). He was inducted in the Tapestry of Diverse Talents at NDSU (2016), and have also won the Ozbun Entrepreneurial Fellowship (2017) as well as the NDSU Innovation Challenge (2017).

Mr. Asif was the elected Vice-Chair and Chair of the IEEE Red River Section for the 2014 and 2015, respectively. He is affiliated with the electrical engineering honor society, Eta Kappa Nu; engineering honor society, Tau Beta Pi; international honor society, Golden Key; and the professional organization, IEEE.